Delft University of Technology

Dispersive Gate Sensing of Hybrid Quantum Dot Systems

Author:
Christian Prosko

Supervisors:
Prof. Dr. Ir. Leo P. Kouwenhoven
Dr. Wolfgang Pfaff

A thesis submitted in partial fulfillment of the requirements for the degree of Master of Science in Applied Physics

May 20, 2019

DELFT UNIVERSITY OF TECHNOLOGY

Abstract

QuTech
Faculty of Applied Science

Master of Science in Applied Physics

Dispersive Gate Sensing of Hybrid Quantum Dot Systems

by Christian Prosko

Spin and topological-qubit based quantum computers require an easily scalable and highly sensitive method for readout and manipulation, for which Dispersive Gate Sensing (DGS) is a promising candidate [1, 2]. DGS enables sensing of single electron tunneling events in a mesoscopic system by measuring a reflected Radio Frequency (RF) signal from a resonator capacitively coupled to one of the system's gate electrodes. From the resonator's perspective, the system is modeled as an effective 'parametric capacitance' [3]. Motivated by its viability for qubit readout and control, we measure transport characteristics of a semiconducting-superconducting hybrid charge island system using this method. Doing so, we observe a spin degeneracy modulation of interdot tunnel couplings resulting from hybridization of a dot orbital with a subgap state of the superconductor, measured entirely within Coulomb blockade. Without DC measurement, we also track a subgap state's energy via voltage intervals between island charge states as a function of field. Subsequently, we attempt to correlate changes in the resonator's internal dissipation with coherence of tunneling into the superconducting island. In particular, we collapse a superconducting island's lowest energy state to the Fermi level by applying a magnetic field. Contrary to expectations, internal dissipation in the resonator did not change dramatically with field, in fact decreasing at charge degeneracy points at all field strengths. We corroborate measurements with existing theory, augmented by simple analytical and numerical models demonstrating that coherence factors of superconducting quasiparticle states and the degeneracy of dot orbitals modulate parametric capacitance. A master equation model of finite temperature interdot tunneling is solved, agreeing with experimental evidence that Sisyphus dissipation is negligible when a dot orbital is hybridized with multiple independent quasiparticle states. To be employed in quantum computers, a full understanding of all phenomena contributing to a DGS signal in these hybrid systems is critical. Hence, these results mark a step towards unambiguous readout of Majorana parity in topological qubits [4].

Contents

Abbreviations & Symbols

DGS	**D**ispersive **G**ate **S**ensing
RF	**R**adio **F**requency
MZM	**M**ajorana **Z**ero **M**ode
N	**N**ormal
SC	**S**uper**C**onducting
QD	**Q**uantum **D**ot
SC	**S**uperconducting **C**harge **I**sland
DQD	**D**ouble **Q**uantum **D**ot

L	Resonator inductance
C	Total resonator capacitance
C_p	Parametric capacitance
C_q	Quantum capacitance
C_t	Tunneling capacitance
R_{sis}	Sisyphus resistance
Z_0	Transmission line impedance ($50\,\Omega$)

Chapter 1

Introduction

QUANTUM COMPUTERS employ the entanglement present between many coupled two-level quantum systems, or *qubits*, to process information in parallel, promising to solve problems infeasible for bit-based classical computers. Their applicability is tremendous, ranging from breaking old encryption schemes [5] to offering better ones [6]. They can search large databases [7], simulate quantum systems for pharmaceutical and materials research [8, 9], as well as solve linear systems of equations and other algorithms [10, 11], all faster than a classical computer.

Unfortunately, of the many physical systems wrangled into the fundamental qubits comprising these computers, nearly all suffer from the rapid decoherence of their state seemingly inherent to all open quantum systems [12]. To achieve fault-tolerance, practical estimates suggest over one thousand physical qubits would be needed to encode a single logical qubit with error correction [13], compounding the requirement that any design for a quantum computer be scalable [14]. Hence, within this thesis we investigate two complementary approaches of granting scalability to quantum computers: subverting the need for error correction with topological qubits [15], and integrating sensitive measurement apparatus into gates defining the qubits themselves with Dispersive Gate Sensing (DGS) [1]. Specifically, we apply DGS to characterizing a normal-superconducting double quantum dot, itself a subsystem of many topological qubit designs.

First, topological qubits utilize a degenerate ground state subspace of certain topological systems, wherein zero-energy excitations at the system's edge are guaranteed to exist by the bulk material's topological phase. Described as quasiparticles, these excitations can be non-Abelian anyons, meaning exchanging or 'braiding' them nontrivially alters the system's state. This is in stark contrast with fermions and bosons occurring fundamentally in nature, which at most garner a π-phase factor upon exchange.

Using this ground state manifold as the computational space of a qubit ensures the qubit state is energetically protected from decoherence by the 'topological gap' separating the first excited state. Furthermore, since any computational state is a many-body state depending on the bulk material phase, it is immune to any local noise. Together, these properties make quantum error correction unnecessary for topological qubits[1].

Presently, scientists are primarily focused on creating topological qubits with semiconducting nanowires [18]. With strong enough spin-orbit coupling, a suitable magnetic field, and proximitized superconductivity, these wires can enter a topological

[1]'Protected' braiding operations only allow for a Clifford complete set of gates on topological qubits formed from Majorana zero modes [16]. To achieve universality, these gates must be supplemented with unprotected operations or coupled to other forms of qubits which *do* require error correction, such as spin qubits [17].

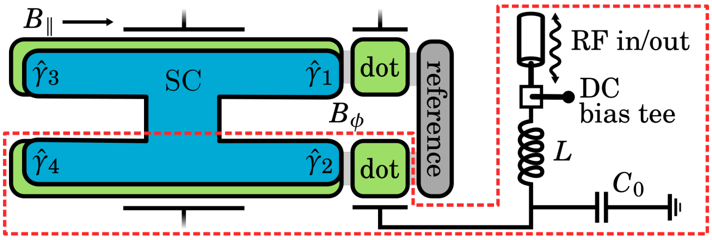

FIGURE 1.1: Minimal implementation of a Majorana box qubit [4]. The Majorana islands are constructed from two proximitized nanowires electrically connected via their superconducting (SC) shells and driven into the topological regime by a parallel field $B_\parallel$. Electrons may tunnel between two dots through the joint fermionic mode formed by MZMs $\hat{\gamma}_1$ and $\hat{\gamma}_2$ or via the reference arm. Interference between the two paths leads to a Majorana parity-dependent tunnel coupling, modulated by a magnetic flux B_ϕ through the loop. The strength of tunnel coupling can be measured via DGS coupled to a dot plunger gate with the simplified circuit shown. We consider the case of a proximitized nanowire coupled to a quantum dot (red box).

p-wave superconducting phase[2] [21, 22]. In this case, the Bogoliubov quasiparticles spanning the superconductors' excitation spectrum include two Majorana Zero energy Modes (MZMs), so called because like Majorana fermions, they are their own antiparticle[3]. These states' wave functions are highly localized at opposite ends of the wire. Analogous to a complex versus a real number, a superposition of two MZMs amounts to a single fermionic mode. If one such mode is formed by Majoranas on two connected nanowire charge islands, they may be braided by measuring occupation parity of the joint fermionic mode, forming the basis of a topological qubit, as in Figure 1.1.

Each of these qubits requires two Coulomb blockaded Majorana islands and multiple quantum dots. Fitting many Majorana parity qubits on the same chip clearly requires an ever increasing number of gates to define the charge islands. If combined with separate on-chip electronics for charge sensors, the task becomes near insurmountable.

Dispersive Gate Sensing alleviates this issue by integrating the sensor's interface with the sample into one of the existing gates defining the qubit, as in the right side of Figure 1.1. By capacitively coupling an LC resonator to the gate electrode, microwave reflectometry can be used to observe single electrons tunneling between any coupled charge islands. A microwave photon trapped in the resonator accrues a phase shift dependent on the quantum state of the coupled qubit which can be measured in the signal returning from the resonator. This method also allows one to leave the entire qubit in Coulomb blockade relative to the lead, reducing the quasiparticle 'poisoning events' which foil a topological qubit's state. Other obvious advantages of DGS are its state-of-the-art charge sensitivity and potential for fast qubit readout [23].

As a research tool, DGS is also profoundly interesting as a *local* probe of mesoscopic systems. While conductance measurements of a Coulomb blockaded system depend on the conductance through the whole system, a DGS probe only sees charge transitions from dots which are capacitively coupled to the lead, enabling non-local tunneling correlation measurements.

The goal of this thesis is therefore to implement DGS in studying a subsystem of a Majorana parity qubit (outlined in red in Figure 1.1). Namely, this thesis will elucidate

[2]Strictly speaking, it is a *quasi*-topological phase, since only some system degrees of freedom are topologically protected [19]. In particular, *quasiparticle poisoning* events can flip the wire's charge parity, altering the qubit state [20].

[3]*Unlike* Majorana fermions, MZMs are not fermions, since they obey non-Abelian exchange statistics.

which charge transfer processes are possible between a superconducting charge island and a quantum dot, and how this translates into a DGS measurement. Within, we demonstrate coherent hybridization of a subgap state with a dot orbital, crucial for the implementation of measurement based topological computers.

Outline of this Thesis

Chapter 2 briefly summarizes quantum dot theory and reflectometry readout of parametric capacitance and Sisyphus resistance, while Chapter 3 introduces models predicting various contributions to this capacitance in double dot systems. These include those from degeneracy in Section 3.1, driven excitations in Section 3.2, finite temperature effects in Section 3.3, and relevant effects for superconducting islands in Section 3.4.

In Chapter 4, results for a normal-superconducting double dot measured by DGS are given. The device is characterized in Section 4.2 while hybridization between a dot orbital and subgap state is noted in Section 4.3. Coherence of single electrons tunneling between the dot and superconductor subgap state is compared with the quasiparticle's energy in Section 4.4. We summarize results in Chapter 5, where possible experiments which further exploit DGS are also proposed.

Chapter 2

Background Theory

MESOSCOPIC systems of charge reside in a vaguely semiclassical regime of physics, where many degrees of freedom behave classically, though others may be well-described by a single quantum state. This chapter therefore aims to lay out the requisite theory of quantum dots and charge sensing techniques required for understanding results in subsequent chapters, along with its many underlying assumptions.

2.1 Mesoscopic Charge Systems in Coulomb Blockade

A Crash Course in Quantum Dots

A piece of conducting material so small that electrostatic repulsion between electrons at the Fermi level renders the energy cost of adding a single charge significant is called a *charge island*. Smaller still, charge islands where quantum confinement makes electronic orbital energy spacing significant is called a *quantum dot*[1]. This occurs when the Fermi wavelength is comparable to variations in the environment's electrostatic potential. These devices are fundamentally useful for reaching the quantum mechanical regime in a circuit-based experimental framework, since they enable one to controllably push single electrons on and off the island, quantizing charge.

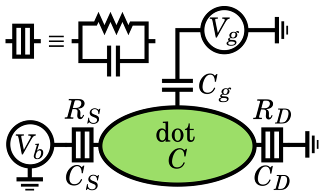

FIGURE 2.1: Effective circuit for a charge island with total capacitance $C = C_g + C_S + C_D$, biased by V_b and gated by V_g. Tunnel resistances $R_{S/D}$ are functions of V_g.

To be specific, consider the simple circuit of a dot connected to leads by tunnel barriers given in Figure 2.1. Such a dot could be defined with cutter gates overtop a nanowire (as in our experiments), or by depleting an enclosure around a small region within a 2-Dimensional Electron Gas (2DEG), among other realizations. At zero temperature, the energy stored on the island with n electrons (or capacitor charge Q) is[2] [24]:

$$U(n) = \frac{Q^2}{2C} = \frac{(C_g V_g - |e|n)^2}{2C} + \sum_{j=1}^{n} E_j = E_c(n - C_g V_g/e)^2 + \sum_{j=1}^{n} E_j \tag{2.1}$$

so that the electrochemical potential is:

$$\mu(n) \equiv U(n) - U(n-1) = E_c(2n-1) - e\alpha V_g + E_n \tag{2.2}$$

[1] Confusingly, charge islands with negligible quantum effects are still often called quantum dots, due to differing charge configurations being separated by significant discrete energies. For simplicity, we also adopt this unfortunate convention.

[2] This expression assumes the *linear transport regime* wherein bias voltage is ~ 0. In this case, excited states of the dot are not involved.

Above, $-e$ is the charge of an electron while $E_c \equiv e^2/2C$ is the *charging energy*, whose significance will be explained below. E_j is the energy of the j'th lowest electron orbital, taking into account all quantum effects outside of the classical circuit picture[3]. The ratio $\alpha \equiv C_g/C < 1$ is the *lever arm* of the gate to the dot, and can be thought of as a coupling strength converting voltage V_g to electrochemical potential induced on the dot. Large lever arms ($\alpha \sim 1$) are critical to the sensitivity of DGS measurements, as we will see in section 2.3.

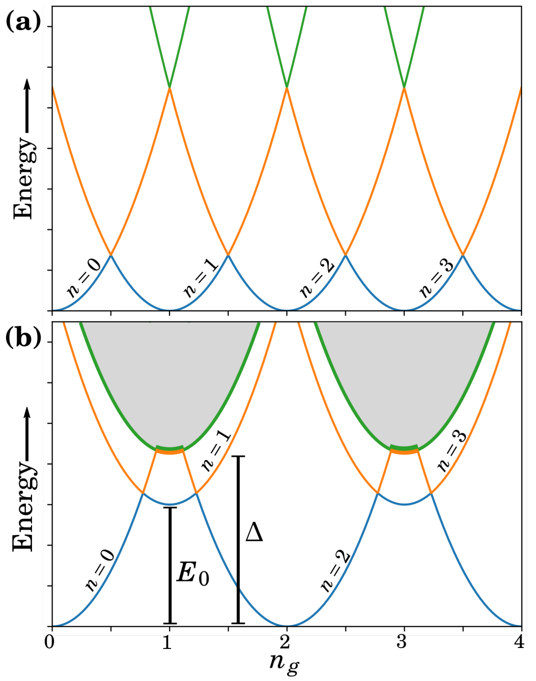

FIGURE 2.2: Energies of dot charge levels $U(n)$ plotted as a function of reduced gate voltage for a normal quantum dot **(a)** and superconducting charge island with $E_0 < \Delta < E_c$ **(b)**. At $k_bT = eV_b = 0$, the dot will reside in the lowest energy charge state. The first and second excited charge states are highlighted with color, with the superconductor's quasiparticle continuum in gray.

Neglecting orbital energies for now, it is clear that two charge configurations are degenerate when C_gV_g/e lies exactly halfway between $n-1$ and n. Letting the leads' Fermi energy at zero bias be $E_F = 0$, V_g is defined so that there are zero dot electrons at $V_g = 0$. Consequently, the *addition energy* needed to add another charge to the dot is $\mu(n) - \mu(n-1) = 2E_c$, twice the charging energy! When thermal energy $\sim k_BT$ is much less than E_c and V_g is off resonance, current flow is prevented by this charging effect, and we say the system is in *Coulomb blockade*. Sweeping the gate voltage leads to the dot accepting electrons from the leads at discretely separated resonances where two charge levels are degenerate, as in Figure 2.2a. This translates to sharp peaks in conductance through the dot near zero bias [25]. At higher biases, the chemical potential difference between the left and right leads makes all dot states within this *bias window* contribute to the current.

It is easy to confuse charge 'levels' with true quantum states, so this warrants some clarification. A fixed charge number n merely restricts the system to the n-electron Hilbert space within a larger Fock space. In fact, a relatively big charge island may have a huge density of states near the n-electron ground state, with a continuum of possible low-energy excitations for the electrons within. Only when the lowest available orbitals' energies $E_n \gg k_BT$ can one say the dot has a well defined quantum state. When this is not the case, the system counterintuitively may be purely classical for fixed charge. Electrons may decohere on short time scales in spite of the island's Fock space possessing a large energy scale E_c separating the ground states of the underlying fixed-charge Hilbert spaces. Quantizing one degree of freedom in a system does not amount to quantum behaviour if other degrees of freedom behave classically.

Note that when $E_n \neq 0$, the *addition energy* needed to insert another electron $E_a \equiv E_c + E_{n+1} - E_n$ includes the energy difference between subsequent orbitals. Usually,

[3] Even this is an approximation: Electrons can only be described as sequentially filling single-particle orbitals when they are non-interacting, but the existence of a non-zero charging energy implies some degree of electron-electron repulsion.

this orbital energy becomes important for small dots with only a few electrons, since in the many-electron regime $n \gg 1$, we expect very little qualitative difference between $n+1$ and n and thus $E_{n+1} - E_n \sim 0$. Of course, this approximates the electron orbitals as being independent of n, but in reality the lowest 'orbital' energy cost for n versus $n+1$ electrons could be similar, while *within* the n-electron Hilbert space the energy of the lowest excitation may be larger than $E_{n+1} - E_n$. Indeed, this is an approximation, since the charging energy implies the existence of repulsive interactions between the electrons, so that their states cannot be described completely independently.

The quantization of charge has other interesting effects in superconducting systems. For example, the Majorana islands in box qubits described in Chapter 1 must remain in Coulomb blockade to fix their parity, and hence the qubit state. For a superconducting island, odd parity charge states are forbidden whenever the lowest energy state E_0 in the SC is higher than the charging energy. This is because superconductors consist of a bosonic condensate of Cooper pairs of electrons, so that unpaired electrons must be quasiparticle excitations of energy at least E_0 (E_0 is the gap Δ when no subgap states are present). To reside in an odd parity state, the electron would have to pay $E_0 > E_c$, so instead the system relaxes by gaining another electron to form a Cooper pair. On the other hand, when $E_0 < E_c$, a single quasiparticle must be present in small regions of width $E_c - E_0$ in energy [26], see Figure 2.2b. In this way one can infer both the island charge parity and value of E_0 from distances between Coulomb resonances, even when many thousands of electrons are present!

Double Quantum Dots

The physical phenomena observable with a single quantum dot is limited by the fact that tunneling to and from leads results in unavoidably incoherent transport, due to the leads' continuous bath of relevant electron states near the Fermi level. To coherently manipulate individual electron spins or observe tunnel coupling between two quantum states (dot orbitals), at least two true quantum dots are thus needed [27], with a well separated excitation energy in each charge level.

A simple circuit schematic of a Double Quantum Dot (DQD) connected in series is shown in Figure 2.3a. As with the single dot, each dot's charge state $|n\rangle$ and $|m\rangle$ is such that energy is minimized, but in this case mutual capacitance C_m makes the dot charges interdependent. The energy as a function of charges n_1 and n_2 is [28]:

$$U(n_1,n_2) = \sum_{i=1,2} E_{ci}\left(n_i - C_{gi}V_{gi}/e\right)^2 + E_c^m\left(n - C_{g1}V_{g1}/e\right)\left(n - C_{g2}V_{g2}/e\right) + \sum_{i=1,2}\sum_{j=1}^{n_i} E_j^i \tag{2.3}$$

where the capacitances $C_{1(2)} = C_{S(D)} + C_{g1(2)} + C_m$ now have corrections due to the mutual capacitance C_m, as do relevant energy scales:

$$E_{ci} \equiv \frac{e^2}{2C_i}\left(\frac{1}{1 - C_m^2/C_1C_2}\right) \sim \frac{e^2}{2C_i} + \mathcal{O}(C_m^2/C_1C_2), \tag{2.4}$$

$$E_c^m \equiv \frac{e^2}{C_m}\left(\frac{1}{C_1C_2/C_m^2 - 1}\right) \sim e^2\frac{C_m}{C_1C_2} + \mathcal{O}(C_m^2/C_1C_2) \tag{2.5}$$

and we have orbital energies E_n^i for dot i. Notably, the magnitude of mutual capacitance C_m between the dots is a measure of how much they behave like separate quantum dots from the perspective of the source and drain, while any interdot tunnel coupling amplitude t_c (introducing off diagonal elements between charge states in the Hamiltonian) quantifies the degree to which they may be treated as separate dots quantum mechanically[4].

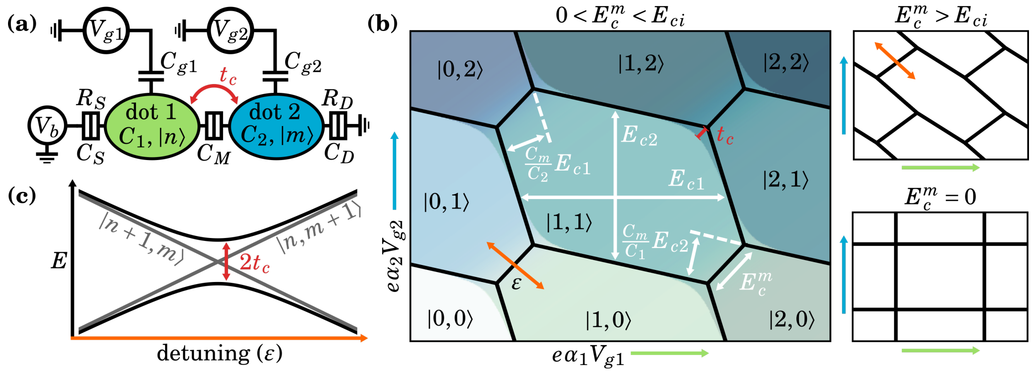

FIGURE 2.3: **(a)** Simplified circuit for a DQD connected in series. Each dot has charging energy $E_{Ci} \sim e^2/2C_i$ for small C_m and chemical potential controlled by gate voltages V_{gi} with lever arms $\alpha_i \equiv C_{gi}/C_i$. **(b)** Charge stability diagrams at $V_b = 0$, neglecting dot orbital energies. Black lines demarcate the boundary between stable charge configurations when $t_c = 0$, while the colored background qualitatively shows average charge values with $t_c = 0.1E_{c1}$. At the 'triple points' where three such lines meet, two dot levels are on resonance with each other *and* the leads. Moving across an interdot transition (orange arrow), quantum dot levels hybridize, mixing the two nearest charge levels' ground states into bonding and anti-bonding superpositions, shown in **(c)**. Triple points in **(b)** are rounded away from the interdot transition in a similarly hyperbolic fashion for $t_c > 0$. These interdot transitions are made energetically inaccessible at zero C_m and t_c (bottom right), while for large C_m or large t_c, they are so broad that the two dots behave as one, gated by both V_{g1} and V_{g2} (top right).

In the 'gate-space' of V_{g1} and V_{g2}, plotting the ground state of this distribution produces a so-called *charge stability diagram*, an example of which is given in Figure 2.3b. As seen in the figure, these diagrams possess all information about capacitances of the system, but they reveal more. A tunneling matrix element t_c between orbitals on dots 1 and 2 hybridizes their ground states when near degeneracy, broadening the region in gate-space where an electron may hop between them, depicted in fig. 2.3c. It also has the effect of broadening the signal we measure in experiment, a detail to be discussed in section 2.3.

A charge stability diagram like the one in fig. 2.3b can be measured in a multitude of ways. Conductance through the whole system can be measured with a lock-in amplifier for example, but this cannot distinguish between individual tunnel couplings without varying them, rather seeing their combined effect on the total conductance. Furthermore, it is insensitive to interdot transitions. Another approach is capacitively coupling a part of the sample to a Single Electron Transistor (SET) (essentially a quantum dot) or a Quantum Point Contact (QPC) and measuring the RF conductance through it [29, 30]. This makes the probe locally sensitive to the subsystem which it is capacitively coupled to, enabling fast selective measurement of tunneling events from a particular dot. These latter methods can approach quantum limits of sensitivity [31], but suffer from scalability issues. Each DQD in a multiple box qubit or spin qubit setup would require its own coupled RF-SET or RF-QPC, which goes hand in hand with additional readout circuitry. In the following sections, we describe a measurement scheme which avoids all of these problems: *Dispersive Gate Sensing*.

[4]As DQDs are well described in the language of quantum mechanics, we often use this parameter instead of tunneling resistance since it is simply the coupling Hamiltonian matrix element, though both are related.

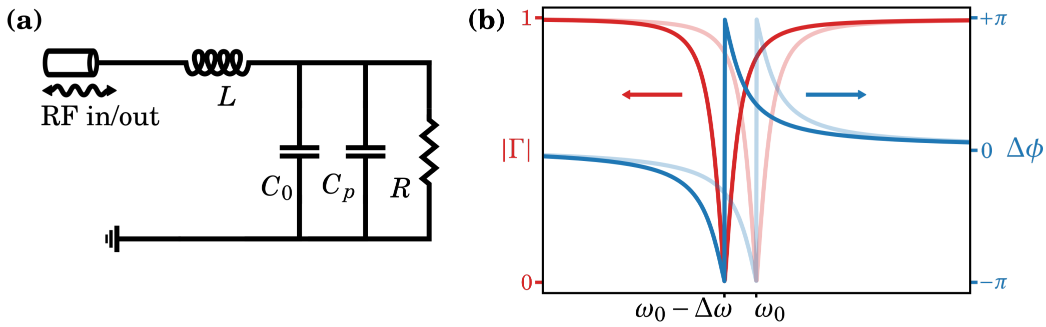

FIGURE 2.4: **(a)** Basic circuit for a series RLC resonator circuit, with R in parallel. **(b)** Reflection coefficient Γ phase $\Delta\phi$ and amplitude from an impedance matched ($R = Z_0$) resonator at different angular frequencies ω.

2.2 Reflectometry Readout of Charge Tunneling

In our experiments, we employ a non-invasive charge sensing technique called Dispersive Gate Sensing (DGS), capacitively coupling a resonator tank circuit directly to one of the gates defining our system. More generally, all other non-invasive charge detection methods involve measuring quantum transport in a mesoscopic system through a capacitive coupling to a sensor device such as an SET or QPC. Since source-to-drain conductance can be negligible when some part of the system is in Coulomb blockade, these approaches are far more sensitive to Coulomb oscillations and interdot transitions than traditional DC measurements [32]. The technique of *reflectometry* is used pervasively across these methods, including DGS. In brief, reflectometry amounts to discerning information about a system by measuring the reflection coefficient of an AC electric signal reflected from a circuit with this system contributing to its impedance.

For the purposes of DGS, reflectometry involves reflecting a Radio Frequency (RF) carrier of angular frequency ω from an RLC resonator with inductance L in series with bare capacitance C_0 perturbed by some shift C_p, see Figure 2.4a. An internal resistance R is also placed in parallel with $C_0 + C_p$, see Figure 2.4a. The impedance of our resonator is [33]:

$$Z = i\omega L + \frac{1}{i\omega(C_0 + C_p) + 1/R} \tag{2.6}$$

For resonators connected to the source or drain of a dot system, R represents tunnel resistance through the system. Alternatively, for a resonator connected to a gate within this dot system, dissipation may still be present in the form of *Sisyphus resistance*, described in section 2.4. The 'bare' capacitance C_0 is to some degree a point of reference, and may be considered for example to be the resonator capacitance when a coupled dot system is in a stable charge state.

This resonator oscillates with characteristic frequency $\omega_0 = 1/\sqrt{LC}$, so that its impedance reduces to R when $\omega = \omega_0$. Clearly, if C_p increases, so changes the resonator capacitance, leading to a downward-shifted resonance frequency $\omega = 1/\sqrt{L(C_0 + C_p)}$ [34], so that the shift is:

$$\Delta\omega = \frac{1}{\sqrt{L(C_0 + C_p)}} - \frac{1}{\sqrt{LC_0}} \sim -\frac{\omega_0}{2}\frac{C_p}{C_0} \qquad C_p \ll C_0 \tag{2.7}$$

A signal at $\omega_0 = 1/\sqrt{LC_0}$ will then be slightly off-resonance with the LC circuit, leading to an increase in amplitude of the reflected signal depending on the line width of the resonance and frequency shift, depicted in Figure 2.4b.

Furthermore, the now off-resonance carrier will experience a phase shift $\Delta\phi$ dependent on C_p and the external resonator quality factor $Q_e^s = \sqrt{L/C}/Z_0$ (see Appendix A for derivation):

$$\Delta\phi \sim -\tan^{-1}\left(\frac{2Q_e^p C_p}{C_0}\right) \qquad C_p \ll \frac{C_0}{Q_r} \tag{2.8}$$

assuming the resonator is probed with the bare frequency $\omega = 1/\sqrt{LC_0}$. Since high signal-to-noise ratio (which is optimal for $\Delta\phi = \pm\pi/2$) is desired in experiment, while $R \geq Z_0$ and $C_p \leq C_0$ typically, eq. (2.8) implies high quality factor resonators are desirable. Unfortunately, this is counteracted by the need to actually measure the reflected signal within a reasonable integration time: A resonator with infinite quality factor never lets any photons escape.

Now we see that DGS can measure small capacitive couplings through a phase shift in a reflected RF signal, but this is useless unless this capacitive coupling tells us something interesting about the charge state. Thankfully, it does. The relevant perturbing capacitance C_p in our case is called the *parametric capacitance* and has direct correspondence with tunnel coupling magnitudes and tunneling events in general. We will also see that dissipation within the resonator, *i.e.* a resonance broadening, carries other important information about multi-dot systems.

2.3 Parametric Capacitance

General Formulation

Parametric capacitance (C_p) is a correction to the capacitance of a system resulting from a low density of states in part of the capacitor [35, 36]. To find a general expression for this correction, consider the differential capacitance of any island of charges as seen by a coupled gate voltage V_g:

$$C_{diff} = \frac{d\langle Q\rangle}{dV_g} \tag{2.9}$$

with charge induced on the capacitor $\langle Q\rangle$, where the braket emphasizes that we consider the charge to be a statistical *average*. If the classical 'geometric' capacitance to the gate is C_g, then from electrostatics:

$$\langle Q\rangle = C_g(V_g - V) \tag{2.10}$$

where V is the total electrostatic potential on the island. As well as this, the total charge on the island may be written in terms of the expectation value of the number of electrons $\langle n\rangle$ or in terms of total self-capacitance C which includes C_g and all other capacitances:

$$-e\langle n\rangle = C_g V_g - CV \tag{2.11}$$

Solving for V gives $V = (e\langle n\rangle + C_g V_g)/C$, which in conjunction with eqs. (2.9) and (2.10) yields a capacitance with two contributions:

$$C_{diff} = \underbrace{\frac{(C - C_g)C_g}{C}}_{C_{geom}} \underbrace{-e\alpha\frac{d\langle n\rangle}{dV_g}}_{C_p} \tag{2.12}$$

where $\alpha = C_g/C$ is the lever arm of V_g to the island. C_{geom} constitutes the classical or *geometric* capacitance C_{geom} of two capacitors in series, subtracted by a correction C_p resulting from changes in the statistical average number of charges on the island. We call this latter correction the *parametric capacitance*, and it is important to note that it arises from changes in the *statistical* average charge on the island, be it a thermodynamic or quantum mechanical average. For a small shift in the gate voltage dV_g centered at a Coulomb resonance, a coupled quantum dot's energy changes by $d\varepsilon = -e\alpha dV_g$, so we see that at zero temperature parametric capacitance is proportional to the local density of states ρ, since $C_p = -(e\alpha)^2 d\langle n\rangle/d\varepsilon = -(e\alpha)^2\rho$. Intuitively, C_p accounts for the fact that a capacitor plate with a low density of states cannot hold an arbitrary amount of charge at a given voltage. This assumption entered our calculation in writing the charge in terms of $\langle n\rangle$: for a closed charge island, $\langle n\rangle$ does not change with voltage so $d\langle n\rangle/dV_g = 0$. When this island is tunnel coupled to an electron reservoir such as a lead, $\langle n\rangle$ is effectively the charge on the lead, arbitrarily large and therefore independent of V_g. In other words, charge must be quantized for $d\langle n\rangle/dV_g$ to be well defined and non-zero, implying a system with relatively low density of available states compared to a grounded metal.

The above treatment of parametric capacitance is quite general, but more specifically one might consider a *single* gate voltage coupled to multiple charge islands. In this case the geometric capacitance is $C_{geom} = \alpha_1 C_1 + \alpha_2 C_2$ as one might expect [28], with α_i being the lever arms of V_g with island $i = 1,2$ and C_i the contributions to their capacitances unrelated to V_g.

Parametric capacitance seen by the gate, however, is the difference of the individual parametric capacitances of each dot, since the loss of charge on one island seen be the gate is also seen as a gain in charge on the other. The expression for parametric capacitance to V_g is:

$$C_p = -e(\alpha_1 - \alpha_2)\frac{d\langle n_1\rangle}{dV_g} \qquad \textit{(near interdot transition)} \tag{2.13}$$

where $\alpha_1 > \alpha_2$ is the gate's lever arm to the first and second island, respectively. Notably, parametric capacitance is zero for a gate which is equally coupled to both islands.

Away from interdot transitions, the assumption that $d\langle n_1\rangle/dV_g = -d\langle n_2\rangle/dV_g$ is no longer valid, because one dot may gain or lose an electron to the leads without the other dot's charge state being effected. Considering the most broad scenario of a gate voltage coupled in parallel to N charge islands with capacitance C_{gi} (which themselves are coupled to each other with capacitance $C_{ij} \equiv C_{ji}$ for $i \neq j$), the differential capacitance is:

$$C_{diff} = \sum_{i=1}^{N} C_i = \sum_{i=1}^{N} \frac{d\langle Q_i\rangle}{dV_g} = \frac{d\sum_{i=1}^{N}\langle Q_i\rangle}{dV_g} \tag{2.14}$$

where $\langle Q_i\rangle = C_{gi}(V_{gi} - V_i)$ is the average charge induced on capacitor C_{gi} and V_i is the electrostatic potential on island i. Proceeding as with the single-island case by writing the total island charges $-e\langle n_i\rangle$ in terms of voltage induced charges, we find:

$$-e\langle n_i\rangle = \underbrace{C_{gi}(V_g - V_i)}_{\langle Q_i\rangle} + \sum_{j\neq i} C_{ij}(V_j - V_i) - C_{ei}V_i \tag{2.15}$$

Above, C_{ei} contains any contributions not from islands or the gate to island i's total capacitance C_i. Solving this equation for $C_i V_i$, then substituting the same expression for C_jV_j into the result, we get:

$$\begin{aligned} C_iV_i &= e\langle n_i\rangle + C_{gi}V_g + \sum_{j\neq i} C_{ij}V_j \\ &= e\langle n_i\rangle + C_{gi}V_g + \sum_{j\neq i} \frac{C_{ij}}{C_j}\left(e\langle n_j\rangle + C_{gj}V_g\right) + \mathcal{O}(C_{ij}^2/C_j^2) \end{aligned} \tag{2.16}$$

Hence, after some rearranging, the total gate charge is found to be[5]:

$$\sum_{i=1}^{N} \langle Q_i\rangle \sim \sum_{i=1}^{N} \alpha_i \left[\left(C_i - C_{gi} - \sum_{j\neq i} \alpha_j C_{ij}\right) V_g - e\left(1 - \sum_{j\neq i} \frac{C_{ij}}{C_j}\right)\langle n_i\rangle\right] \tag{2.17}$$

to first order in mutual capacitances. Differentiating finally produces an expression for C_{diff}:

$$C_{diff} \sim \underbrace{\sum_{i=1}^{N} \alpha_i \left(C_i - C_{gi} - \sum_{j\neq i} \alpha_j C_{ij}\right)}_{C_{geom}} - \underbrace{\sum_{i=1}^{N} e\tilde{\alpha}_i \frac{d\langle n_i\rangle}{dV_g}}_{C_p} \qquad C_{ij} \ll C_j \tag{2.18}$$

where we have defined an effective lever arm $\tilde{\alpha}_i \equiv (1 - \sum_{j\neq i} C_{ij}/C_j)C_{gi}/C_i$. Comparing this to the expression in eq. (2.12), it is clear that the total parametric capacitance is the sum of the individual parametric capacitances, negatively corrected by the additional polarizability that mutual capacitance grants the island electrons. As with the parametric capacitance near an interdot transition, this is another manifestation of the fact that a gate probing parametric capacitance will not be sensitive to electrons rearranging themselves on what is practically the same 'capacitor plate'.

A distinct expression for parametric (specifically, quantum) capacitance can also be qualitatively guessed from a Hamiltonian approach [37]. Consider a system of electrons probed by a gate voltage V_g with quantum Hamiltonian $\hat{H}$. This Hamiltonian may in principle be separated into a component $-\hat{H}_q$ containing all dependence on quantum degrees of freedom, as well as a term H_c which contains purely classical contributions to electrostatic energy. Since C_{geom} is by definition the classical component of capacitance, and because the energy stored on a capacitor is $CV^2/2$, it must be the case that $H_c = C_{geom}V_g^2/2$ in the absence of dissipation or current into the system. Under the assumption that the entire electronic system behaves as a capacitor as seen by the gate voltage, we must have $\langle\hat{H}\rangle = \langle\mathcal{L}\rangle = C_{eff}V_g^2/2$ for some effective capacitance C_{eff}, since the Hamiltonian consists only of potential terms. Differentiating this equation twice implies $C_{eff} = \partial^2 E/\partial V_g^2$. Applying this to our system's Hamiltonian leads to the result:

$$C_{eff} = \frac{\partial^2\langle\hat{H}\rangle}{\partial V_g^2} = \frac{\partial^2 H_c}{\partial V_g^2} - \frac{\partial^2\langle\hat{H}_q\rangle}{\partial V_g^2} = C_{geom} - \underbrace{\frac{\partial^2\langle E_q\rangle}{\partial V_g^2}}_{C_q} \tag{2.19}$$

where E_q is the energy of our quantum system, neglecting classical capacitance terms.

Qualitatively, this demonstrates that a capacitance measured under these assumptions is proportional to the second derivative of the system's energy with respect to the probe voltage. This is analogous to an effective mass model, wherein electrons in a metal are modeled as a free band $\varepsilon_{\vec{k}} = \hbar^2k^2/2m^*$ for some effective mass m^* varying from the bare electron mass, with capacitance taking the place of mass here. Just as in a free electron approximation, this effective capacitance description of C_p is valid

[5] A similar result for $N = 2$ was obtained in [3] by neglecting mutual capacitance altogether.

whenever the Hamiltonian is quadratic in probe voltage V_g. The above expression is often qualitatively cited but seldom motivated [38–40], despite ambiguity as to why the quantum Hamiltonian should be *subtracted* from H_c rather than added[6].

Quantum Capacitance

An important distinction may be drawn between two forms of parametric capacitance: *quantum* and *tunneling*. Quantum capacitance is described by eq. (2.19), and always contributes to the total parametric capacitance when two charge states are hybridized [3]. Physically, it results from adiabatic evolution of the electronic quantum state as the probe voltage oscillates in time (see Figure 2.5). Near an anti-crossing of two charge states in a DQD, the electron does not discretely (in time) jump from one dot to another, but rather transitions between varying superpositions of occupying the first or second dot, affecting the average dot occupation $\langle n \rangle$ and thus C_p.

More specifically, a DQD with no orbital degeneracy, tunnel coupling t_c and detuning from resonance[7] ε has ground state energy $E_g = -\sqrt{(\varepsilon/2)^2 + |t_c|^2}$, leading to a quantum capacitance at zero detuning of:

$$C_q|_{\varepsilon=0} \propto \left.\frac{\partial^2 E_g}{\partial \varepsilon^2}\right|_{\varepsilon=0} = \frac{1}{2|t_c|} \tag{2.20}$$

This is simply the non-degenerate ($N = 1$) case from the more general double-dot model solved in Section 3.1. Note from Section 3.1 that the same result would be obtained if eq. (2.13) was used. Thus, quantum capacitance is an inverse measure of the interdot tunnel coupling, and hence, the hybridization between their states!

Tunneling Capacitance

While quantum capacitance measures the system energy's dependence on the oscillating voltage, *tunneling capacitance* depends primarily on thermal or driven excitation and relaxation rates of the tunneling electron, and does not require quantum level hybridization. Large interdot tunnel couplings are equivalent to very fast electron tunneling rates, say Γ_r between the dots. If the probe voltage $V_g(t) = V_g^0 + \delta V \sin(\omega t)$ oscillates with frequency $\omega \ll \Gamma_r$ and if excitation rates $\Gamma_e \ll \omega$, then the electron can easily track the instantaneous voltage set by the probe: this is simply the adiabatic quantum capacitance regime described above[8].

Tunneling capacitance arises when excitation rates Γ_e and relaxation rates Γ_r of the electron are comparable to the probe oscillation: $\Gamma_e, \Gamma_r \lesssim \omega$. For a DQD slightly away from zero detuning, this is because excitations and relaxations correspond to either tunneling off of the dot or back on to it. The oscillating probe controls which charge state is of higher energy, so if the electron excites and relaxes on the time scale of one oscillation, it is on average lagging behind the preferred polarization induced by $V_g(t)$, depicted in fig. 2.5.

Clearly then, when tunneling capacitance is relevant depends on sources of excitation and relaxation in the system. Charge relaxation rates Γ_r depend on the geometry and material properties of the system, but can conceivably be comparable to

[6]A brief explanation in [37] claims that $\hat{H}$ is the system's *Routhian*, serving as a Hamiltonian for the quantum degrees of freedom but as *minus* the Lagrangian for circuit degrees of freedom.

[7]From the electrostatic theory of DQDs described earlier, the detuning of charge levels near resonance is always linear in either dot's gate voltage V_g.

[8]The high frequency regime $\omega \gg \Gamma_r$ is not considered here, since in this case the resonator would stimulate higher excitations as in photon assisted tunneling microwave experiments [28].

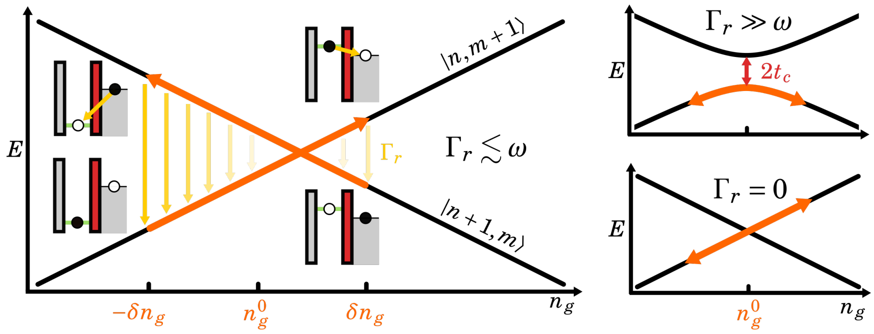

FIGURE 2.5: Tunneling with rate Γ_r near a charge degeneracy point for a coupled DQD or dot-lead system. for different charge relaxation rates Γ_r, subject to an oscillating reduced gate voltage $n_g(t) = n_g^0 + \delta n_g \sin(\omega t)$. For slow oscillations or strong tunneling (top right), the electron remains in its initial state, and no dissipation occurs. When charge tunneling rates are finite but small (so that $t_c \approx 0$), the electron can not respond to electrostatic pressure from the gate $n_g(t)$ immediately, gaining energy in the excited state until it finally relaxes. In this case, dissipation occurs. The insets show chemical potential diagrams of a dot-lead system before and after tunneling. Note the electron does not necessarily relax at the maximum or minimum oscillation amplitude of $n_g(t)$, but because at this point the energy difference between excited and ground state is maximum, the relaxation rate is largest at these points. When tunnel rates are negligible (bottom right), the involved dots or leads are effectively decoupled and no energy is dissipated. Figure based on one from [41].

the characteristic frequencies of resonators used in this thesis' experiments (~ hundreds of MHz) [42]. Supposing the energy difference between ground and lowest excited states is ΔE, thermal excitation rates can then be estimated as $\Gamma_e = \Gamma_r n_p$ where $n_p = (e^{\Delta E/k_B T} - 1)^{-1}$ is the occupation number of a thermal bath of phonons in the environment [3]. For truly discrete tunnel-coupled charge states, we expect in our experiment interdot couplings well above $1\hbar\cdot$GHz [43], which would significantly exceed temperatures of $k_B T \sim 0.4\hbar\cdot$GHz (at 20 mK, a typical base temperature of dilution refrigerators). Consequently, we only expect significant contributions to Γ_e from temperature when two charge states are very weakly hybridized, such as in the coupling between a dot state and the continuum of states in a lead. It has also been argued that Rabi driving to excited states by $V_g(t)$ can occur even when ω is far off resonance with t_c [43] provided driving power δV_g is strong enough, but this is easily avoided in our measurements by lowering this amplitude until power broadening is no longer observed[9].

One final mechanism by which the electron can be excited is through diabatic Landau-Zener Transitions (LZTs), which occur when the driving potential is either very strong or very fast. Supposing $V_g(t)$ oscillates with V_g^0 centered at zero detuning between two charge levels, its potential is approximately linear when $V_g(t) \sim \delta V_g \omega t$ passes near 0 detuning. The probability P_{LZT} of a LZT occurring as detuning is swept across zero for levels hybridized with tunnel coupling t_c is then [44]:

$$P_{LZT} = e^{-2\pi|t_c|^2/\hbar e \delta V_g \omega} \tag{2.21}$$

assuming a generously large lever arm $\alpha \sim 1$. For tunnel couplings on the order of GHz (μeV) and probe frequencies on the order of 100s of MHz as in our experiments, this

[9]The Rabi formula implies the occupation probability of excited states is asymptotically $\propto (e\delta V_g/(\omega - \Delta E)^2$ for driving frequency ω and transition energy ΔE when ω is far detuned and δV_g is weak enough that $e\delta V_G \ll |\omega - \Delta E|$.

probability is vanishingly small for driving potentials less than 2.25 μeV (for a 50 Ω system being driven with -100 dBm of power), see Figure 2.6. This is the regime we use in experiment. On the other hand, when tunnel couplings are negligibly small or zero, the probability of an LZT occurring approaches 1. This is the limit of two non-interacting dots or a dot coupled to a lead: if two charge levels are completely decoupled, then there is no mechanism by which the electron can *avoid* a LZT by tunneling to the other dot. For leads, inelastic processes dominate charge tunneling since there are an abundance of states in the lead at any point above its Fermi level [23]. Significant tunnel rates can coexist with negligible tunnel couplings (*i.e.* a strong tunnel barrier), since the sum of very small tunnel rates to each of the many unoccupied states can add to a significant total rate nonetheless [45]. The same is true for metallic charge islands, or any system with a continuum of states spaced practically infinitesimally in energy.

Evidently, we can identify tunneling capacitance as the result of incoherent charge tunneling between nearly degenerate quantum states. Intuitively, this makes it difficult to derive a clear relation between the tunneling capacitance and characteristics of orbitals or subgap states in charge islands[10], but a closely related phenomena called *Sisyphus resistance* may enable one to conclude whether or not electrons are tunneling between discrete quantum states without dephasing or incoherently with a bath of states from a DGS measurement.

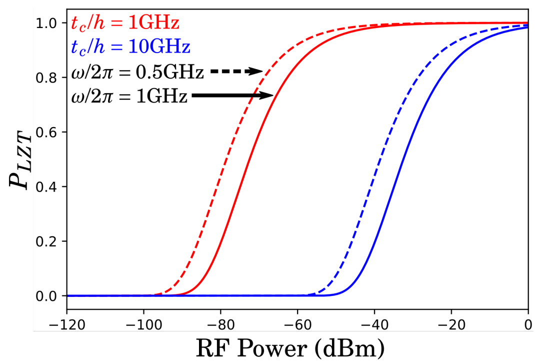

FIGURE 2.6: Probability of LZT occurring for an $\alpha = 1$ gate oscillating with frequency $\omega/2\pi$ about a charge degeneracy point of tunnel coupling t_c. Power is relative to a 50Ω line.

2.4 Sisyphus Resistance

As mentioned above, the probability of a LZT is near unity when two decoupled charge levels (*i.e.* in a DQD or lead and dot) are swept across a degeneracy point. Phrased another way, it is impossible for an electron to adiabatically remain in the system's ground state if the initial and final ground state are separated by too high of a potential barrier, such as a tunnel barrier. Recall the Adiabatic theorem, which states that a system initially in some eigenstate of a Hamiltonian varying slowly in time will remain in the analogous eigenstate of the instantaneous Hamiltonian, *unless this eigenstate becomes degenerate with another.*

By definition of a level crossing, the energy of a system's ground state relative to the first excited state can only *increase* upon approaching this crossing. If relaxation rates are finite and the energy released during relaxation is lost to the environment, dissipation must be occurring, shown in fig. 2.5. For an oscillating voltage sweeping two charge states across degeneracy, the resulting dissipation seen by the oscillator circuit is called Sisyphus resistance [45]. Mathematically, it is written in terms of the time averaged power dissipation P_{sis}:

$$R_{sis} = \frac{(\delta V_g)^2}{2P_{sis}} \tag{2.22}$$

[10]Tunneling problems of a statistical nature such as this one are usually solved using a master equation approach to find the probability of occupying different quantum states [41, 46, 47].

P_{sis} is heuristically defined as the average energy dissipated minus the average energy gained per resonator cycle:

$$P_{sis} = \frac{\omega}{2\pi}\int_0^{2\pi/\omega} dt\Delta E(t)(\Gamma_{1\to2}P_1 - \Gamma_{2\to1}P_2) \tag{2.23}$$

Above, $\Delta E(t) = E_1(t) - E_2(t)$, $\Gamma_{1\to2}$ and $\Gamma_{2\to1}$ are tunnel rates between 'charge system' 1 and 2, and P_1 and P_2 are probabilities of an excess electron occupying either one of these coupled systems.

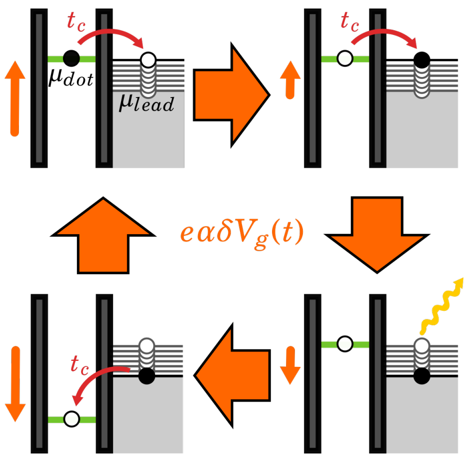

FIGURE 2.7: Chemical potential diagram of a dot orbital coupled to a lead. Additional dissipation can occur through elastic tunneling into excited states of the lead followed by relaxation through scattering with a phonon. This cartoon assumes charge relaxation rates $\Gamma_r \lesssim \omega$ but orbital relaxation rates $\gg \omega$.

Importantly, the dissipated power is zero whenever the relaxation and excitation rates are zero or whenever the probability of occupying the excited state is zero. For a discrete set of states, the former occurs for a very strong tunnel barrier, while the latter arises from LZTs being suppressed by a significant tunnel coupling. For a dot state coupled to a continuum of states such as a lead, these individual tunnel couplings may combine to a significant tunnel rate according to Fermi's golden rule [47], even when tunnel barriers are very strong.

From the above considerations, we see that the existence of Sisyphus resistance is indicative that the system's relevant charge states are approximately decoupled, but that a process nonetheless exists allowing an electron to relax by tunneling across a barrier. For a sufficiently strong tunnel barrier, this means that many degenerate or near degenerate states are present in the ground charge state or excited charge state manifold. We do not claim the converse statement, however: For strong tunnel barriers, a marked *lack* of dissipation increase while sweeping voltages across a charge degeneracy point does not imply that only two or very few quantum states are involved, as far as current experiments have suggested. We note that additional dissipation may also occur via elastic tunneling into excited states of another charge level followed by orbital relaxation, see Figure 2.7.

One scenario not yet mentioned is the case of strong tunnel coupling between a single dot orbital and a collection of nearly degenerate states. In this case, we expect the electron to adiabatically remain in the ground *charge* state manifold, but naively predict the resonator may drive orbital excitations within the nearly degenerate state set, since the excitation energies are very small. While this would not lead to tunneling capacitance or Sisyphus resistance as we defined it since no charge relaxation occurs, the electron still may relax its orbital state, dissipating energy from the resonator (Figure 2.7). This intuition, and whether or not it is accurate, will be discussed in somewhat more detail in Section 3.3.

Chapter 3

Theoretical Results

This chapter is presented as an explanation for phenomena we observe in experiment, especially charge parity dependent tunneling. Measuring or braiding the state of a Majorana box qubit amounts to measuring the fermion parity dependent tunnel coupling of a Superconducting Charge Island (SCI) with a Quantum Dot (QD) [4]. It is imperative, then, that any other transport phenomena modulating the interdot tunnel rate depending on its parity be accounted for and calibrated out. In order, we therefore explain the effect of introducing degeneracy to a Double Quantum Dot (DQD) system, followed by accounting for thermal and driving effects, as well as coherence effects for the case of an SCI. Beyond building qubits, this also illustrates the wealth of information contained in the impedance of a gate coupled to a quantum charge system.

3.1 Effect of Degeneracy on Quantum Capacitance

Since we will be dealing with semiconducting QDs coupled to SCIs with subgap states, it is not always as simple as each charge level having a single discrete ground state for an excess electron to occupy. Orbitals could be spin-degenerate, for example, or many subgap states could be clustered near degeneracy. To gain some intuition regarding how degeneracy affects quantum capacitance, we thus present a toy model minimally describing this. A schematic of the model is given in Figure 3.1. For a single dot state $|D\rangle$ tunnel-coupled to an N-fold degenerate charge state $\{|n\rangle\}_{n=1}^{N}$ by tunnel coupling t_c with energy detuning ε, the Hamiltonian is:

$$\hat{H} = \frac{\varepsilon}{2}|D\rangle\langle D| - \frac{\varepsilon}{2}\sum_{n=1}^{N}|n\rangle\langle n| + \sum_{n=1}^{N}\left[t_c|n\rangle\langle D| + \text{h.c.}\right] \tag{3.1}$$

The eigenvectors and eigenenergies of this Hamiltonian can easily be solved for directly. The eigenvalue equation $\hat{H}|\psi\rangle = E|\psi\rangle$ where $|\psi\rangle$ has components $|\psi\rangle = c_0|D\rangle + \sum_n c_n|n\rangle$ leads to the $N+1$ coupled equations:

$$(\varepsilon/2)c_0 + t\sum_n c_n = Ec_0 \tag{3.2}$$

$$t^*c_0 - (\varepsilon/2)c_n = Ec_n \qquad \forall n \tag{3.3}$$

From inspection, we deduce two cases. First, if $E \neq -\varepsilon/2$, then $c_n = t^*c_0/(E+\varepsilon/2)$, and accordingly E is $E_\pm = \pm\sqrt{(\varepsilon/2)^2 + N|t|^2}$. Allowing $c_0 = 0$ would force $E = -\varepsilon/2$, against our assumption, so c_0 must instead be determined by normalization relative to c_n.

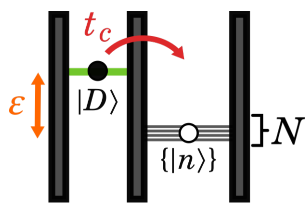

FIGURE 3.1: Energy diagram of a single dot orbital tunnel coupled by t_c to some N-fold degenerate state on another charge island, detuned by ε.

In the second case, where $E = \varepsilon/2$, we find $c_0 = 0$, and $\sum_n c_n = 0$. By inspection, we can identify $N-1$ orthonormal solutions where, say, $c_1 = 1$ and $c_i = -1$ for some $1 < i < N_{qp}$. In summary, the eigenstates of our system are:

$$|\pm\rangle = \frac{1}{\sqrt{A}}|D\rangle + \frac{1}{\sqrt{A}}\sum_n \frac{t_c^*}{E_\pm + \varepsilon/2}|n\rangle, \qquad E_\pm = \pm\sqrt{(\varepsilon/2)^2 + N|t_c|^2} \tag{3.4}$$

$$|n'\rangle = \frac{1}{\sqrt{2}}[|1\rangle - |n\rangle], \qquad E_{n'} = -\varepsilon/2 \tag{3.5}$$

for $N \geq n > 1$. We define $A \equiv 1 + N|t_c|^2/(E_\pm + \varepsilon/2)^2$.

For significant tunnel couplings $t_c > k_B T$, the ground state E_- is energetically well separated from the degenerate $|n'\rangle$ states near $\varepsilon = 0$, where quantum capacitance C_q is expected to be significant. Using its eigenvector, we can then calculate C_q at $k_B T = 0$. If we probe from the dot's gate, the probability of an excess electron residing on this dot is:

$$\langle n\rangle_D = |\langle D|-\rangle|^2 = \frac{1}{A} = \frac{1}{2}\left(1 - \frac{\varepsilon}{\sqrt{\varepsilon^2 + 4N|t_c|^2}}\right) \tag{3.6}$$

Near zero detuning, $e\alpha' dV_g = d\varepsilon$ where $\alpha' = \alpha_1 - \alpha_2$ is the gate's difference in lever arms between the dot and degenerate island. The quantum capacitance is thus:

$$C_q = -(e\alpha')^2 \frac{d\langle n\rangle_D}{d\varepsilon} = (e\alpha)^2 \frac{N|t_c|^2}{4(N|t_c|^2 + (\varepsilon/2)^2)^{3/2}} \tag{3.7}$$

plotted in Figure 3.2. Clearly, the quantum capacitance has a peak of $C_q = (e\alpha)^2/4\sqrt{N}|t_c|$ at $\varepsilon = 0$, and a quick calculation reveals that this peak has a Full Width at Half Maximum (FWHM) of $\Delta\varepsilon = 4\sqrt{4^{1/3} - 1}\sqrt{N}|t_c| \approx 3.07\sqrt{N}|t_c|$.

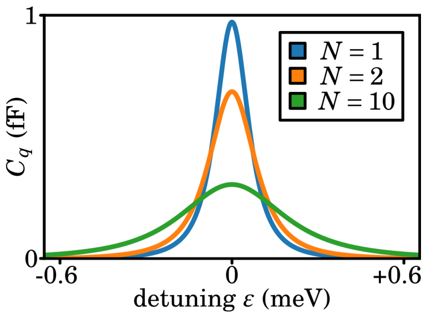

FIGURE 3.2: Quantum Capacitance for a discrete charge state coupled to N-fold degenerate charge states in its ground state, using a realistic tunneling frequency $t_c/h = 10GHz$ [43] and lever arm $\alpha = 1$.

From this model, we deduce that measured quantum capacitance broadens and flattens about an interdot transition linearly in the tunnel coupling, and $\propto 1/\sqrt{N}$ in the degeneracy of one of the island's states. This conclusion should hold whenever t_c is significant and excitation rates are negligible. Thus, the phase response signal observed in experiment for dot-to-lead or dot-to-metallic-island transitions with DGS likely has negligible contributions from quantum capacitance when t_c is significant since $N \gg 1$, with tunneling capacitance dominating. Since tunneling and quantum capacitance for dots coupled to continua both rely on small tunnel couplings (*i.e.* small inter-state anti-crossings), we expect there to be a very low capacitive signal measured with DGS in experiment for relatively open tunnel barriers *aside* from the classical geometric capacitance.

To test how valid these claims are in a slightly more realistic scenario, we simulate a dot orbital coupled to a second degenerate dot using zero temperature numerical simulations (described in Appendix B). These simulations account for charging energies, mutual capacitance, degenerate fermionic modes, and parity dependent tunneling. Due to their modularity, they will be compared with experiment and other theory throughout this thesis. The results for various degeneracies are given in Figure 3.3.

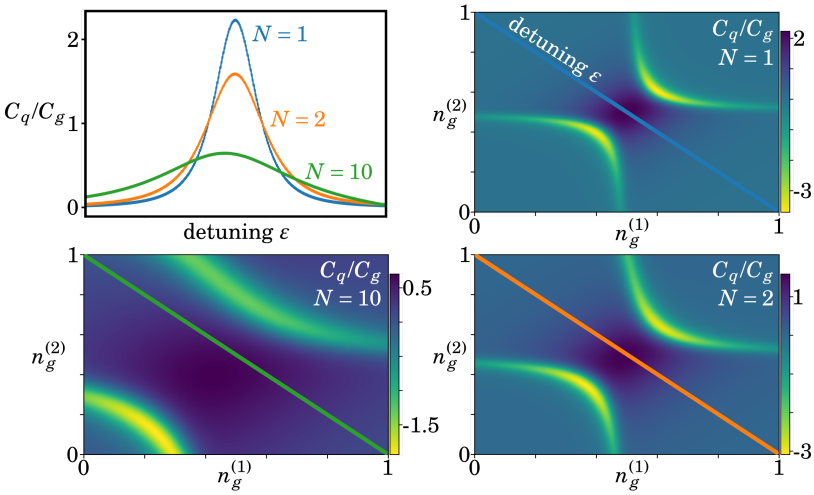

FIGURE 3.3: Simulated charge stability diagrams of a DQD where one dot's level is non-degenerate and the other is N-fold degenerate. Linecuts are plotted to show qualitative agreement with Figure 3.2, with resonances broadening and widening with increasing degeneracy. The $N = 10$ linecut deviates slightly from the center because of interference from the lead transition.

Spin Effects

The toy model also suggests a zero-field spin effect on quantum capacitance for DQD's with spin-degenerate levels, originally predicted by Cottet *et al* using linear-response theory [48]. For such a DQD, there are two cases. When the DQD's total charge parity is even, there is a degeneracy: either a spin-up or spin-down electron may tunnel into an empty orbital so that there is a 2-fold degeneracy of final states. For odd total charge parity, however, there is no degeneracy. An excess electron of some spin shared between

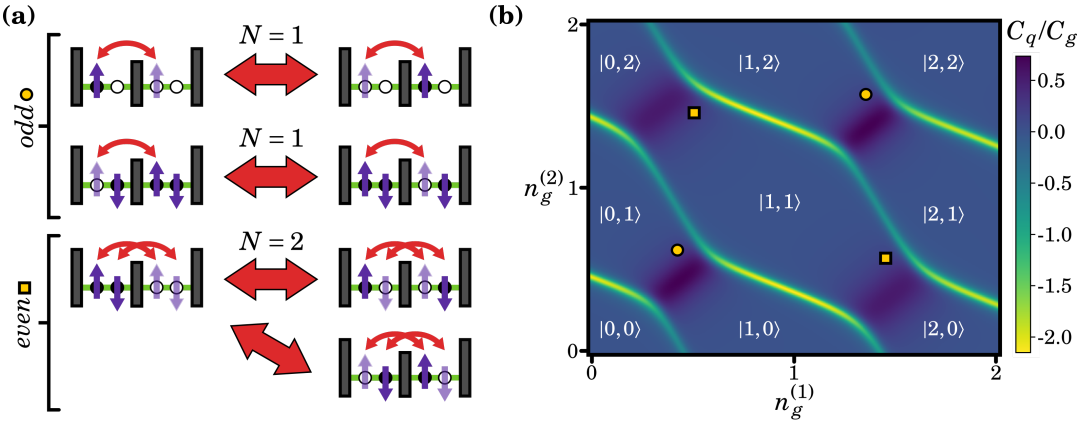

FIGURE 3.4: **(a)** Tunneling channels for a spin-degenerate DQD at even and odd parity. **(b)** Simulated charge stability diagram of quantum capacitance at $T = 0$ for a DQD with $E_c = E_c^{(1)} = E_c^{(2)}$, $t_c = 0.1E_c$, and $E_m = 0.7E_c$, in order to most closely qualitatively reproduce the results of Cottet *et al* [48]. Note that C_q peaks at interdot transitions for even DQD charge parity are lower and broader than those for odd parity. Leads are modeled as dots with zero charging energy and tunnel coupling to dots $t_l = 0.02E_c$ in order to reproduce correct transition placement and tunnel broadening, but should only be considered qualitatively. Conversely, lead transitions do produce a negative capacitance as predicted by Gonzalez-Zalba *et al* [23].

two orbitals will maintain its spin as it tunnels provided there is no mechanism for spin-flips (*eg.* due to a nuclear spin bath [49]). For a full orbital and one half full orbital, only the electron with spin not present in both dot states may tunnel, by the Pauli exclusion principle. These processes are schematized in Figure 3.4a. From the perspective of the toy model, an even parity DQD has $N = 2$ while an odd parity DQD has $N = 1$. For tunneling between discrete states in quantum dots or subgap states in SCIs at zero field, we therefore expect a frequency shift due to quantum capacitance that is $\sqrt{2}$ smaller for even parity transitions.

Since the $N = 2$ degeneracy is lifted when a magnetic field is applied due to the Zeeman effect, the smaller capacitance peak is predicted by Cottet *et al*'s model to become sharper and narrower, while the $N = 1$ peak remains invariant [48]. Obviously, a Majorana qubit experiment in semiconducting nanowire geometries would involve a strong magnetic field. This would break the zero field spin degeneracy, but this spin blockade effect could still lead to parity dependent tunneling[1]. As a further demonstration of our numerical model, we reproduce qualitatively their results at zero field in Figure 3.4b.

As a final note, the conclusions of this model may hold more closely for tunneling into a SCI's quasiparticle continuum than for a metallic island, since superconductors have a well known 'coherence peak' of diverging density of states at the superconducting gap edge. This means that the vast majority of states involved in tunneling are very closely spaced at the gap edge.

3.2 The Adiabatic Regime of Dispersive Gate Sensing

Thus far, in addition to assuming low temperatures, we have also assumed that charge level excitations are only driven by an RF-oscillating gate voltage when the avoided crossings of two charge states are small compared to the drive power and frequency. From the perspective of diabatic Landau-Zener transitions (LZTs), this proved justified for frequencies below a gigahertz (see Equation (2.21)), as we use in experiment. For systems driven by periodic potentials, however, Rabi oscillations may also lead to fluctuating population of excited states. Earlier experiments in DQD systems found that DGS measurements' dependence on the RF power was well described by a Rabi-like model [43].

Here, we justify neglecting these Rabi processes by showing that for $e\alpha\delta V_g \ll \sqrt{N}|t_c|$, the probability of excited states whose energy has non-zero second derivative being occupied is itself on the order of $(e\alpha\delta V_g/\sqrt{N}|t_c|)^2$.

We consider the toy model of Section 3.1 depicted in Figure 3.1, where the detuning oscillates as $\varepsilon(t) = \delta\varepsilon\sin(\omega t)$ for some angular frequency ω. As a reminder, this model describes a DQD where one dot has a N-fold degenerate orbital $\{|n\rangle\}_{n=1}^{N}$ while the other $|D\rangle$ is non-degenerate. The Hamiltonian at $t = 0$ is:

$$\hat{H}_0 = +\sum_{n=1}^{N}\left[t_c\,|n\rangle\langle D| + \text{h.c.}\right] \tag{3.8}$$

[1] This would depend on spin-orbit coupling. Majoranas, for example, are expected to have a different spin 'canting' angle for Majorana quasiparticles on opposite ends of a topological nanowire, arising due to strong spin-orbit coupling [50, 51].

with eigenstates:

$$|\pm\rangle_0 \equiv |\pm\rangle\,|_{\varepsilon=0} = \frac{1}{\sqrt{N+1}}\left[|D\rangle \pm \sum_{n=1}^{N}|n\rangle\right], \quad |n'\rangle_0 \equiv |n'\rangle\,|_{\varepsilon=0} = \frac{1}{\sqrt{2}}\left[|1\rangle - |n\rangle\right] \tag{3.9}$$

of energy $\pm\sqrt{N}|t_c|$ and 0 respectively. The perturbing potential is then:

$$\hat{H}' = \frac{1}{2}\delta\varepsilon\sin(\omega t)\left[|D\rangle\langle D| - \sum_{n=1}^{N}|n\rangle\langle n|\right] \tag{3.10}$$

which clearly has the effect of mapping $\hat{H}'|\pm\rangle = \frac{1}{2}\varepsilon(t)|\mp\rangle$ and $\hat{H}'|n'\rangle = -\frac{1}{2}\varepsilon(t)|n'\rangle$. Evidently, the oscillating detuning only couples the ground state $|-\rangle$ to its excited counterpart, merely evolving the phase of any $|n'\rangle$ component of the state. Assuming the system resides in its ground state $|-\rangle_0$ at $t=0$, we can therefore neglect all $|n'\rangle$ states and the problem reduces to that of Rabi oscillations. In experiment, our resonators probe at sub-GHz frequencies, while typical tunnel couplings are $\mathcal{O}$(GHz). Consequently, the rotating wave approximation that $2\sqrt{N}|t_c|+\omega \gg 2\sqrt{N}|t_c|-\omega$ does not hold and the standard Rabi formula is likely inapplicable[2]. Instead, we use second order perturbation theory. The resulting probability of occupying the excited state $|+\rangle_0$ is (see Appendix F for derivation):

$$P_+(t) \sim \left(\frac{\delta\varepsilon}{4\sqrt{N}|t_c|}\right)^2 \sin^2(\omega t) \qquad \omega \ll 2\sqrt{N}t_c,\, \delta\varepsilon \ll 2\sqrt{N}|t_c| \tag{3.11}$$

under a rotating-wave-like approximation which assumes the probe frequency to be much lower than the transition frequency. As expected, the probability of occupying an excited state due to Rabi driving is negligible whenever $\delta\varepsilon \ll \sqrt{N}|t_c|$. Interestingly, in this limit the Rabi oscillations occur with the same frequency as the drive potential.

3.3 Finite Temperature Effects

From Section 3.2, we found that the probability of an oscillating RF gate voltage driving excitations to the $|+\rangle$ state (in the toy model of Section 3.1) is negligibly small in the case that driving power is small compared to the transition energy. Still, we have neglected the possibility of the electron occupying a localized $|n'\rangle$ state. At first this seems valid – the oscillating detuning does not couple the ground state to any $|n'\rangle$ states – but thermal excitation may cause tunneling between $|-\rangle$ and $|n'\rangle$. Since this state has $\langle n\rangle_D = 0$, however, the electron has zero quantum capacitance while occupying this state. This still holds some significance, though, since the quantum capacitance of the system is the C_q it experiences in each state weighted by the probabilities of occupying each state. Hence, we investigate how additional decoupled states in one of two charge islands gives rise to thermal quantum and tunneling capacitance effects, even when the interdot tunnel coupling is large. Resulting from this, we find that thermal effects enable tunneling capacitance and Sisyphus resistance-like dissipation even when the oscillating potential is too weak to drive transitions to excited charge states, but these contributions too are diminished by increasing degeneracy. The limitations of our calculation are discussed, including the possibility of inelastic tunneling mediated by phonons adding Sisyphus resistance beyond that predicted by our model.

[2] The Rabi formula states that the occupation probability of the excited state $P_+(t)$ oscillates as $P_+(t) = (\delta\varepsilon/\hbar\Omega)^2\sin^2(\Omega t/2)$ for Rabi frequency $\Omega = \sqrt{(2\sqrt{N}|t_c|/\hbar-\omega)^2+(\delta\varepsilon/\hbar)^2}$.

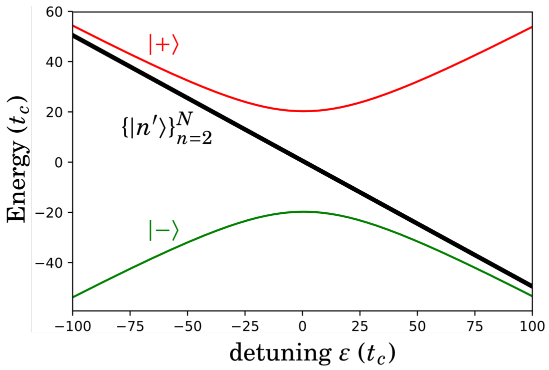

FIGURE 3.5: Energy structure of a dot orbital detuned by ε from an island with $N = 400$ levels spaced apart by $\delta = 1/N$. Labels denote the corresponding eigenstates in the $\delta = 0$ case. Note $E_+ - E_- \approx 40t_c = 2\sqrt{400}t_c$, while the gap to the $|n'\rangle$-like states is smaller, especially at positive ε.

To find an expression for parametric capacitance and Sisyphus resistance, we begin with the degeneracy model of Section 3.1 with $N \gg 1$. This, we argue, is sufficient to describe a dot orbital coupled to a charge island with a continuum of states when the continuum states are decoupled from each other. Pictured in Figure 3.5, we plot an altered version of the degeneracy model with many states $N \gg 1$ where we have shifted the energy of each $|n\rangle$ state to $-\varepsilon/2+(n-1)\delta$ for some $\delta \ll t_c$, simulating a continuum. As can be seen from the plot, there still exists $N-1$ states decoupled from the quantum dot where the electron is localized to the degenerate island. Assuming all relevant states to be near the lowest decoupled state's energy, we can approximate thermal excitation rates from $|-\rangle$ to each of these states to be identical. This approximation is especially valid for a dot level tunneling into a superconductor's BCS quasiparticle continuum, since in that case the density of states is drastically higher near the gap edge. In the end, this means we can assume the tunneling rates $\Gamma_{-\to n'}$ into each of these nearly degenerate states are roughly the same, and define P_n as the *total* probability of occupying any of the decoupled states. These states are approximately localized to the second island for small splitting δ, so that the expectation value of the dot orbital's charge when residing in one of these states is zero. We also assume that the splitting is small enough that we can approximate the system ground state as $|-\rangle$. The solution for a true continuum of states, rather than an N-fold degenerate one, would likely differ in that thermal excitations would occur between them.

To find a result for parametric capacitance and dissipation, we follow a similar approach to Gonzalez-Zalba *et al* [23], using master equations. To begin, suppose that our system is subject to an oscillating voltage $V_g(t) = V_g^0 + \delta V_g \sin(\omega t)$ with corresponding energy detuning $\varepsilon(t) = \varepsilon_0 + \delta\varepsilon \sin(\omega t)$. The expectation value of charge on the non-degenerate dot $\langle n_D \rangle$ may be written as:

$$\langle n_D \rangle = \langle n_D \rangle_- P_- + \langle n_D \rangle_+ \underbrace{P_+}_{\approx 0} + \sum_{n=2}^{N} \underbrace{\langle n_D \rangle_{n'}}_{=0} P_{n'} \approx \langle n_D \rangle_- P_- \tag{3.12}$$

where the eigenstates are fixed at $\varepsilon = \varepsilon_0$. Above, we approximated $P_+ \approx 0$ as it follows from the assumption that $\hbar\omega, \delta\varepsilon \ll \sqrt{N}|t_c|$. The parametric capacitance is then:

$$\begin{aligned} C_p = -e\alpha \frac{d\langle n_D \rangle}{dV_g} &= -e\alpha P_-(t) \frac{d\langle n_D \rangle_-}{dV_g} - e\alpha \langle n_D \rangle_- \frac{dP_-(V_g(t))}{dV_g} \\ &= -e\alpha P_-(t) \frac{d\langle n_D \rangle_-}{dV_g} - \frac{e\alpha \langle n_D \rangle_-}{\delta V_g \omega \cos(\omega t)} \dot{P}(t) \end{aligned} \tag{3.13}$$

where the gate has lever arm to $|D\rangle$ of α, no cross-capacitance to the other island, and where we neglect mutual capacitance for convenience. The notation $\dot{f}(t) \equiv df/dt$ is used hereafter. In the second equality, we applied the inverse function theorem and chain rule. To find the $|-\rangle$ occupation probability, we use the master equations:

$$\dot{P}_- = \Gamma_- P_n - \Gamma_+ P_-, \quad \dot{P}_n = \Gamma_+ P_- - \Gamma_- P_n \tag{3.14}$$

where, as in [3, 23, 45], the excitation rates $\Gamma_+ = \Gamma_0(e^{\Delta E/k_B T} - 1)^{-1}$ and relaxation rates $\Gamma_- = \Gamma_+ + \Gamma_0$ are written based on the assumption that thermal processes give rise to them [47]. Namely, Γ_+ is the product of some bare relaxation rate Γ_0 (assumed to be constant for voltages between $V_g^0 - \delta V_g$ and $V_g^0 + \delta V_g$) with the occupation number of a coupled phonon bath. Γ_- is shifted by Γ_0 because relaxation occurs even in the absence of phonons. $\Delta E = E_{n'} - E_- = -\varepsilon/2 + \sqrt{\varepsilon^2/4 + N|t_c|^2}$ is the energy difference between ground $|-\rangle$ and excited states $|n'\rangle$. Recall that P_n describes the total probability of occupying any of the $|n'\rangle$ states. These master equations can be solved to first order in δV_g, as is done in Appendix D. The result is, neglecting transient terms:

$$P_- \sim \frac{1}{2} + \frac{\Gamma_0}{2\Gamma_\Sigma}(1 - \Lambda\cos(\omega t)) + \frac{\Gamma_0 \Lambda}{2(\Gamma_\Sigma^2 + \omega^2)}(\Gamma_\Sigma \cos(\omega t) + \omega \sin(\omega t)) \quad t \to \infty \tag{3.15}$$

where we defined:

$$\Gamma_\Sigma = (\Gamma_- + \Gamma_+)|_{t=0} = \frac{\Gamma_0}{\tanh(\Delta E_0/2k_B T)}, \quad \Lambda = \frac{1}{4}\left(\frac{\varepsilon_0}{\sqrt{\varepsilon_0^2 + 4N|t_c|^2}} - 1\right)\frac{(\Gamma_0/\omega)\delta\varepsilon/k_B T}{\sinh^2(\Delta E_0/2k_B T)} \tag{3.16}$$

with $\Delta E_0 \equiv \Delta E|_{t=0}$. From section 3.1, we recall that:

$$\langle n_D \rangle_- = \frac{1}{2}\left(1 - \frac{\varepsilon_0}{\sqrt{\varepsilon_0^2 + 4N|t_c|^2}}\right), \qquad \frac{d\langle n_D \rangle_-}{dV_G} = -e\alpha \frac{N|t_c|^2}{4(N|t_c|^2 + (\varepsilon/2)^2)^{3/2}} \tag{3.17}$$

Now, if we were to apply eq. (3.14) to find the instantaneous differential capacitance, it would contain sinusoidally oscillating $\tan(\omega t)$ terms, which diverge at certain points. This is a result of the AC signal: when electrons briefly move towards the capacitor 'plate' in phase with the oscillating signal, it is as though no capacitor is present since charge is moving freely, leading to an infinite instantaneous capacitance. We thus average out all sinusoidal terms to find:

$$\langle C_p \rangle = C_q + C_t \tag{3.18}$$

where the quantum capacitance contribution is:

$$C_q = (e\alpha)^2 N|t_c|^2 \frac{1 + \tanh(\Delta E_0/2k_B T)}{8(N|t_c|^2 + (\varepsilon_0/2)^2)^{3/2}} \tag{3.19}$$

corresponding to the derivative of the thermodynamic expectation value of charge, while the tunneling capacitance term is:

$$C_t = \frac{(e\alpha)^2}{16k_B T}\left(1 - \frac{\varepsilon_0}{\sqrt{\varepsilon_0^2 + 4N|t_c|^2}}\right)^2 \frac{1}{\cosh^2(\Delta E_0/2k_B T) + (\omega/\Gamma_0)^2 \sinh^2(\Delta E_0/2k_B T)} \tag{3.20}$$

Naturally, the quantum capacitance term is dominant whenever the energy difference is large compared to temperature, though it is itself suppressed by large effective tunnel couplings $\sqrt{N}|t_c|$. The tunneling capacitance, on the other hand, is small when ω is large compared to Γ_0, but reaches a saturated value beyond about $\Gamma_0 = 2\pi\omega$. This

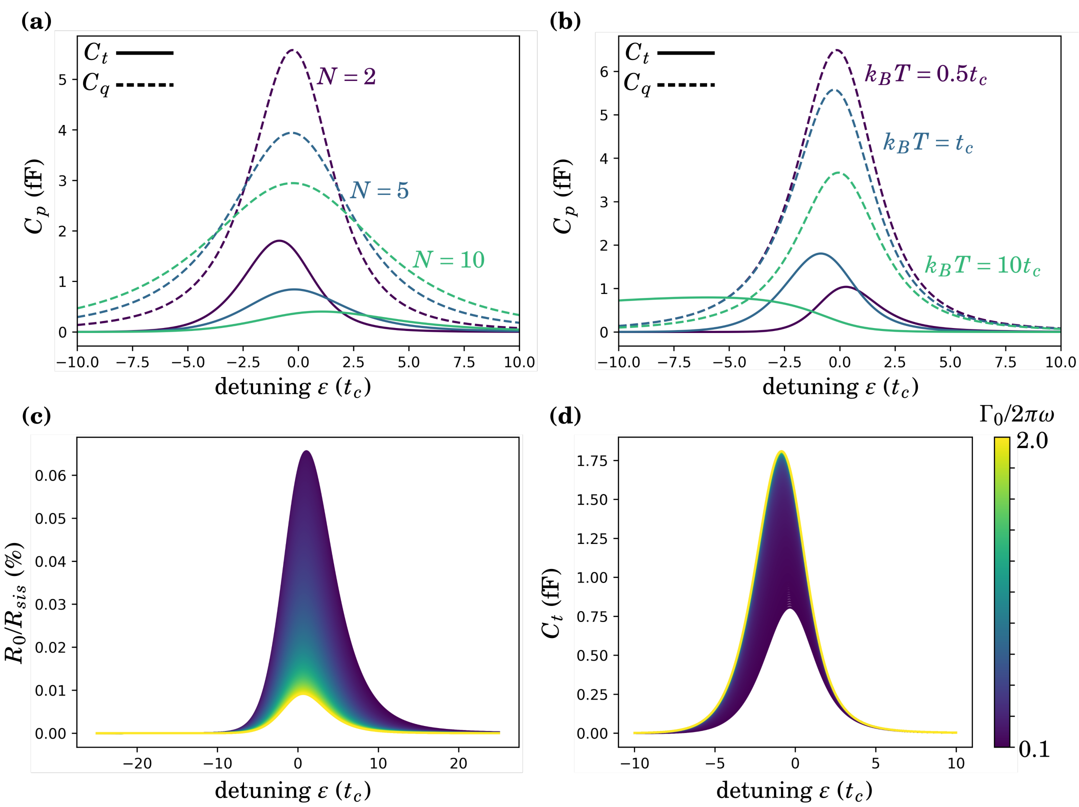

FIGURE 3.6: Thermal effects on the parametric capacitance and dissipation in the degeneracy model of Section 3.1. All plots use the parameters $N = 2$, $\Gamma_0 = 10\omega$, $\omega = 500\,\text{MHz}$, $t_c/h = 1\,\text{GHz}$, and $k_BT = t_c$, unless they are explicitly varied. **(a)** Tunneling C_t and quantum C_q capacitance for different degeneracies. Within this limited model, both capacitances are broadened by increasing degeneracy. **(b)** Capacitances plotted for different temperatures. Quantum capacitance C_q is reduced by increasing temperature, while temperature increases C_t up to a maximum due to additional tunneling events occurring, until thermal broadening takes over and reduces it. Somewhat surprisingly, quantum capacitance is the dominant capacitive contribution in every scenario. **(c)** Ratio of the resistance quantum $R_0 = h/2e^2$ over the Sisyphus resistance. R_{sis} is large enough to be negligible for a wide range of tunnel rates Γ_0. R_{sis} achieves a maximum at $\Gamma_0 \approx (\pi/2)\omega$, though Γ_0 is not shown for less than $0.2\pi\omega$. **(d)** Tunneling capacitance for different orbital excitation rates in the degenerate island. C_t increases with increasing Γ_0, quickly converging to a maximum at about $\Gamma_0 = 2\pi\omega$, beyond which multiple excitations occur on the timescale of the probe signal.

is not surprising, since the resonator can not possibly dissipate more energy per cycle than it puts in to the system. We plot C_t and C_q for various parameters in Figure 3.6.

To some extent, this explains how it is possible for a parametric capacitance signal to be measured in dots tunneling to highly degenerate islands, where the results of section 3.1 suggested that quantum capacitance should be negligible at zero temperature. Finite temperature populates the $|n'\rangle$ states, leading to a tunneling capacitance contribution resulting from tunneling between the ground ‘bonding’ state of the DQD and states localized on the degenerate island. This is in contrast to the result for a non-degenerate DQD system found by Mizuta *et al* [3], where tunneling was between bonding and anti-bonding charge state superpositions.

With experiment in mind, we would also like to see if the degeneracy of a DQD system leads to a dissipative impedance contribution, depending on the level of degeneracy N. The average power dissipated $\langle P \rangle$ into the DQD can heuristically be defined as the net energy gained through excitation and relaxation events averaged over a resonator cycle:

$$\langle P\rangle = \langle \Delta E(t)(\Gamma_- P_n - \Gamma_+ P_-)\rangle = \langle \Delta E(t)\dot{P}_-(t)\rangle \tag{3.21}$$

We expand to the lowest order in $\delta\varepsilon/k_B T$ which survives after time averaging to find:

$$\langle P\rangle \sim \frac{\Gamma_0(e\alpha\delta V_g)^2}{16k_B T\sinh\left(\frac{\Delta E_0}{k_B T}\right)}\left(\frac{\varepsilon_0}{\sqrt{\varepsilon_0^2+4N|t_c|^2}}-1\right)^2\left(1-\frac{1}{1+(\omega/\Gamma_0)^2\tanh^2\left(\frac{\Delta E_0}{2k_B T}\right)}\right) \tag{3.22}$$

contributing a parallel Sisyphus-like resistance to the effective impedance of the DQD of:

$$R_{sis} = \frac{(\delta V_g)^2}{\langle P\rangle} \tag{3.23}$$

plotted in Figure 3.6c. Importantly, it becomes infinite at large positive or negative detunings ε_0, but seems to be a negligible amount of dissipation, particularly when compared with the results of Esterli *et al*. They found the resistance quantum to be on the order of one percent of R_{sis} in simulation of a *non*-degenerate DQD tunneling between charge states.

The implications of this lack of dissipation depend crucially on how valid the model is. It may hold for a system of a small number of degenerate states, but for islands with larger degeneracies and continua, it seems to predict zero contribution from parametric capacitance and negligible dissipation. In these latter cases, this conclusion is likely unphysical, since in experiment we do observe a capacitive frequency shift in DGS measurements as well as dissipation in certain scenarios where a metallic (quasi-) continuum of states is present.

Hence, this model is not complete. One possibility is that interactions with the environment induce an effective coupling between nearly degenerate states in a continua [52]. We plot the nearly-degenerate model of Figure 3.5 introducing this assumption in Figure 3.7. In this case, the nearly degenerate continuum states can no longer decouple from the quantum dot state by entering a superposition with each other, and so are repelled in an anti-crossing by the dot state. The width of these anti-crossings decreases as the level spacing between states decreases, so that even for large tunnel couplings anti-crossings may be small enough that the resonator can induce LZTs. This would lead to tunneling capacitance and Sisyphus resistance effects from the resonator driving excitations within the continuum.

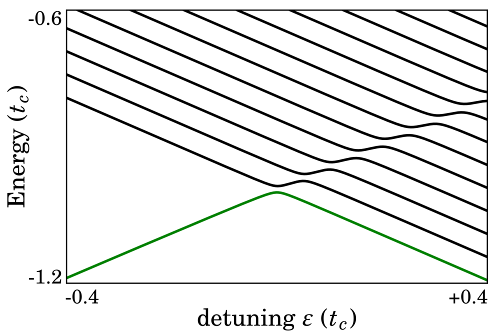

FIGURE 3.7: Zoomed-in band structure of a dot orbital tunnel coupled via t_c to $N = 400$ levels, linearly spaced by $t_c/20$, themselves coupled via $t_d = t_c$. The dot orbital traces a path of anti-crossings through the continuum states.

3.4 Normal-Superconducting Double Quantum Dots

In this section, we describe a low energy model of a Superconducting Charge Island (SCI) coupled to a Normal Quantum Dot (QD), assuming the thermal energy $k_B T$

is much smaller than dot charge level spacings, superconducting gaps, and subgap state energies. This last assumption is strong since it precludes Majoranas, which are pinned at zero energy. Since the conclusions drawn here are related to electron and hole-like coherence factors u and v modulating charge tunneling depending on a SCI's parity however, this is unimportant: Majorana zero modes have $u = v$, being self-conjugate Bogoliubov quasiparticles. We calculate parametric capacitance of the considered system in the regime of quantum capacitance, borrowing some results for an ordinary DQD (Mizuta *et al*, Ciccarelli & Ferguson [3, 41]). Implicitly, this means we assume significant tunnel couplings between the SCI and QD.

The Model

Consider a QD of charging energy E_C^N with a tunnel coupling t to a SCI of charging energy E_C^S and gap Δ. Furthermore, suppose that there is a single spinful subgap state $E_0 < \Delta$. The Hamiltonian is:

$$\hat{H} = \overbrace{E_C^N(\hat{n}_N - n_g^N)^2}^{\hat{H}_D} + \overbrace{E_C^S(\hat{n}_S - n_g^S)^2 + \sum_{\substack{\sigma=\pm1 \\ p=e,h}} \left(E_0 \hat{\gamma}^\dagger_{0\sigma p}\hat{\gamma}_{0\sigma p} + \sum_\nu E_\nu \hat{\gamma}^\dagger_{\nu\sigma p}\hat{\gamma}_{\nu\sigma p}\right)}^{\hat{H}_{SC}} + \hat{H}_T \tag{3.24}$$

neglecting any mutual capacitance between the dots, where $\hat{H}_T$ is a general tunneling Hamiltonian:

$$\hat{H}_T = \sum_{\sigma=\pm1} \left(t_{0\sigma}\hat{n}_+\hat{c}_{0\sigma} + \sum_\nu t_{\nu\sigma}\hat{n}_+\hat{c}_{\nu\sigma} + \text{h.c.}\right) \tag{3.25}$$

with $\hat{n}_D \equiv \sum_n n\,|n\rangle\langle n|$ and $\hat{n}_S = \sum_{\nu,\sigma} \hat{c}^\dagger_{\nu\sigma}\hat{c}_{\nu\sigma}$ being the QD and SCI's charge number respectively, and $n_g^{N/S}$ being their reduced gate charges. Hence, $\hat{H}_D$ and the first term of $\hat{H}_{SC}$ are simply the quantized version of charge island energies given in Equation (2.1). The operators $\hat{n}_\pm = \sum_n |n \pm 1\rangle\langle n|$ create/annihilate a charge on the normal dot. Finally, the fermionic $\hat{\gamma}^\dagger_{\nu\sigma p}$ operators create Bogoliubov quasiparticles (Bogoliubons) on the SCI with energy $E_\nu = \sqrt{\varepsilon_\nu^2 + |\Delta|^2}$ ($\nu \neq 0$) for non-superconducting energy band ε_ν characterized by quantum number ν. These are defined in terms of the SCI's electron operators and coherence factors $u_{\nu\sigma}$ and $v_{\nu\sigma}$ as:

$$\hat{\gamma}_{\nu\sigma e} = u_{\nu\sigma}\hat{c}_{\nu\sigma} - \sigma v_{\nu\sigma}\hat{c}^\dagger_{-\nu-\sigma}e^{-i\hat{\phi}},\ \hat{\gamma}_{n\sigma h} = \hat{\gamma}_{\nu\sigma e}e^{i\hat{\phi}} \tag{3.26}$$

with inverse relation:

$$\hat{c}_{\nu\sigma} = u^*_{\nu\sigma}\hat{\gamma}_{\nu\sigma e} + \sigma v_{\nu\sigma}\hat{\gamma}^\dagger_{\nu-\sigma h} \tag{3.27}$$

The exponential of the superconducting phase operator $e^{i\hat{\phi}}$ creates a Cooper pair in the condensate, so that $\hat{\gamma}_{n\sigma e/h}$ represent electron or hole-like excitations respectively of energy E_ν.

The same relation holds for $\nu = 0$ [46, 53], as a consequence of using the BCS condensate $|g\rangle$ as the vacuum state of quasiparticles. It is of no profound physical meaning, then, if this is assumption is made even when the subgap state is well described as a second dot level tunnel-coupled to the superconductor. In this sense, u_0 and v_0 are parameters 'mapping' a fermionic operator to another, the Bogoliubon, which acts in a simpler way on $|g\rangle$.

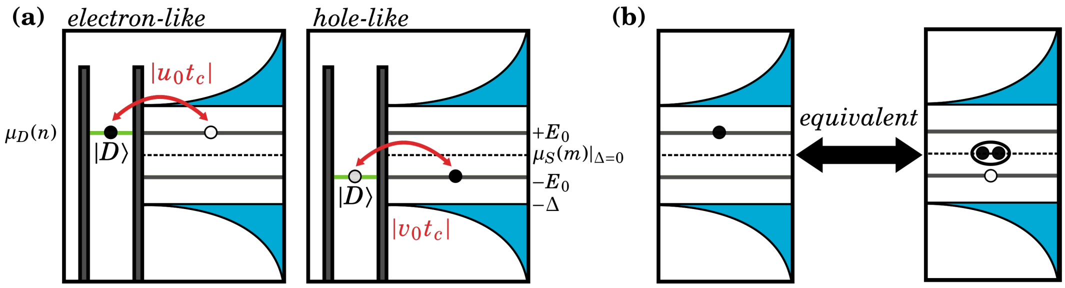

FIGURE 3.8: **(a)** Two tunneling processes possible when a dot orbital $|D\rangle$ is coupled to a SCI with lowest energy state $E_0 < \Delta, E_C^S$. $\mu_{D(S)}(n)$ is the chemical potential of the n'th charge state on the dot (SCI). Black and empty circles denote electrons and holes, respectively. Because charge is quantized, particle-hole symmetry is broken, and gaining an electron on the SCI by *gaining* or *losing* a quasiparticle involves either an electron or hole-like tunneling process, respectively. **(b)** Illustration of particle-hole symmetric excitations. When Cooper pair number is unfixed, hole-like quasiparticles are indistinguishable from electron-like quasiparticles.

Superconducting Charge Islands with Subgap States

Additional assumptions of our model are as follows in the case where $|E_0 - \Delta| \gg k_B T$. If the normal dot level is near resonance with a charge state of the superconductor modulated by the subgap state $E_C^S \pm E_0$, and the subgap state is well separated from continuum quasiparticle states, we can project out all continuum-state terms from the Hamiltonian. Furthermore, since we will be studying the transfer of a single electron between each subsystem, spin is implicitly conserved in $\hat{H}$, and subsystem energies are independent of spin, we can drop the spin index σ and assume the electron in question maintains its spin at say $\sigma = 1$. The Hamiltonian reduces to:

$$\hat{H} = \hat{H}_D + E_C^S(N - \hat{n} - n_g^S)^2 + E_0 \hat{\gamma}_{0p}^\dagger \hat{\gamma}_{0p} + t\left[u_0^* \hat{n}_+ \hat{\gamma}_{0e} - v_0 \hat{n}_+ \hat{\gamma}_{0h}^\dagger + \text{h.c.}\right] \tag{3.28}$$

The value of $p \in \{e, h\}$ depends on whether the normal dot level is near resonance with an electron-like or hole-like transition into the superconductor (*i.e.* above or below the gap). Finally, we assume that the likelihood of having two quasiparticles simultaneously on the SCI is negligibly small. In a voltage sweep where the SCI already has a quasiparticle, the QD would be on resonance with the SCI's Fermi level so that a Cooper pair can be formed from a QD electron and the quasiparticle far before it is resonant with the top of the gap. A Cooper pair could also break and doubly occupy a spinful subgap state, but this costs twice E_0 and so is suppressed whenever $k_B T \ll E_0$. Consequently, we can reduce the Fock space of the SCI to containing only the superconducting condensate $|g\rangle$ as well as the states $\hat{\gamma}_{0p}^\dagger |g\rangle$ for $p \in \{e, h\}$. Hence, we are left with two distinct physical processes:

First, if the SCI has even parity and the QD has n charges, the SCI can accept a charge by creating a quasiparticle. Since the charge on the SCI must have increased by one in this process, the quasiparticle must be electron-like:

$$|i\rangle = |g\rangle \otimes |n\rangle \to |f\rangle = \hat{\gamma}_{0e}^\dagger |g\rangle \otimes |n-1\rangle$$

with matrix element $\langle f|\hat{H}_T|i\rangle = t u_0$ (sample calculations are in Appendix E).

Second, if the SCI has odd parity (so it contains a single quasiparticle under our assumptions), and excepts an electron from the QD initially containing n charges, it must form a Cooper pair from this electron and quasiparticle since the electron does not have sufficient energy to tunnel into a quasiparticle state. Then the only possible processes are the following hole-like transfer and its reverse, because the SCI must *gain* a charge by *eliminating* a quasiparticle:

$$|i\rangle = \hat{\gamma}^{\dagger}_{0h}\,|g\rangle \otimes |n\rangle \rightarrow |f\rangle = |g\rangle \otimes |n-1\rangle \tag{3.29}$$

with corresponding matrix element $\langle f|\hat{H}_T|i\rangle = -tv_0^*$. A cartoon of these processes is given in Figure 3.8.

Clearly then, near resonance with an electron-like ($p = e$) or hole-like ($p = h$) charge transfer between the dots, the problem reduces to an effective two-level system with Hamiltonian:

$$\hat{H} = \frac{\varepsilon}{2}(|i\rangle\langle i| - |f\rangle\langle f|) + t_p\,|f\rangle\langle i| + t_p^*\,|i\rangle\langle f| \tag{3.30}$$

where ε is the detuning between the occupied QD state and the unoccupied SCI state under consideration[3], and $t_p = tu_0$ for $p = e$ and $-tv_0^*$ for $p = h$. This Hamiltonian has eigenstates:

$$|\pm\rangle = \frac{1}{\sqrt{2}}e^{i\theta}\sqrt{1 \pm \frac{\varepsilon}{\Delta E}}\,|i\rangle \pm \frac{1}{\sqrt{2}}\sqrt{1 \mp \frac{\varepsilon}{\Delta E}}\,|f\rangle \tag{3.31}$$

with energies $E_{\pm} = \pm\sqrt{\varepsilon^2/4 + |t_p|^2}$. We define the transition energy $\Delta E \equiv E_+ - E_-$ and $\theta \equiv \mathrm{Arg}(t_p)$. At zero temperature, we may apply the model from Section 3.1 for $N = 1$ to obtain the quantum capacitance:

$$C_q = -(e\alpha')^2 \frac{|t_p|^2}{4(|t_p|^2 + (\varepsilon/2)^2)^{(3/2)}} \tag{3.32}$$

reaching a maximum of $-(e\alpha')^2/4|t_p|$. This coherence-factor dependent tunneling has also been predicted to modify the conductance through a SCI [53], an effect which has been measured [54]. Unfortunately, to be a direct measure of coherence factors, such a measurement requires that tunneling rates between the SCI and the source or drain be near identical. With regards to quantum capacitance, however, we now see that the frequency shift of a resonator probing the charge transfer with DGS is inversely proportional to the appropriate coherence factor at zero detuning, provided temperature is low relative to the bare tunnel coupling. If variations in the bare tunnel coupling across a few successive SCI to QD charge transitions can be neglected, coherence factors may be directly measured by taking the ratio of frequency shifts for an odd to even or an even to odd charge transition onto a SCI.

For completeness, we note how the complete parametric capacitance at finite temperature may be calculated for this model, following Mizuta *et al*'s method for a DQD. Suppose we probe the QD coupled to an SCI and consider a single excess electron hopping between the subsystems. In that case, $|f\rangle$ corresponds to an extra electron on the SCI, and from the eigenvectors of Section 3.1 for $N = 1$ we can infer the ground and excited state occupation expectation values as $\langle n\rangle_{\pm} = 1 \pm \varepsilon/\Delta E$. Then the expectation value of the single charge on the QD $\langle n\rangle$ is, in that model:

$$\langle n\rangle = P_+\,\langle n\rangle_+ + P_-\,\langle n\rangle_- = \frac{1}{2} + \frac{\varepsilon}{2\Delta E}\chi \tag{3.33}$$

[3]Choosing the QD as occupied is arbitrary, since substituting $n \to n-1$ leads to the scenario of the SCI being 'occupied' and donating a charge to the QD.

where $\chi \equiv P_- - P_+$, and we applied normalization of probability: $P_+ + P_- = 1$. Using 2.13, the parametric capacitance is then:

$$C_p = \underbrace{4(e\alpha')^2 \frac{|t_p|^2}{\Delta E^3}\chi}_{C_q} + \underbrace{(e\alpha')^2 \frac{\varepsilon}{\Delta E}\frac{\partial \chi}{\partial \varepsilon}}_{C_t} \tag{3.34}$$

where we used the energy-voltage relation $d\varepsilon = e\alpha' dV_g$. The first term describes a system in a constant mixed state, so it is the quantum capacitance contribution, whereas the second term is non-zero whenever the state is affected by perturbations in V_g, and so is the tunneling capacitance. If we apply the result of Mizuta for a DQD at non-zero temperature by substituting in the effective tunnel coupling t_p, we obtain:

$$C_p = \frac{(e(\alpha_1 - \alpha_2))^2}{|t_p|} \left[\frac{|t_p|^3}{\sqrt{\varepsilon_0^2/4 + |t_p|^2}} \tanh\left(\frac{\sqrt{\varepsilon_0^2/4 + |t_p|^2}}{k_B T} \right) \right] \tag{3.35}$$

Charge Islands with a Continuum of States

Broadly, quantum capacitance is the sole contribution to parametric capacitance when the probed system's (potentially mixed) quantum state is fixed on the time scale of the probing RF carrier's oscillations. Given that the quasiparticle states above the gap in a SCI constitute a continuum or 'quasi-continuum' of excitations, this condition is not met. It is reasonable hypothesize that while the driving RF probe is not strong or fast enough to induce Landau-Zener transitions to excited charge states in the regime of concern, it very well may drive excitations *within* the SCI to higher quasiparticle states, as discussed in Section 3.3. These transitions do not effect an electron's charge state, and therefore may occur at a different rate than charge relaxation and excitation. Finding a quantitative expression using a more realistic model than in Section 3.3 is difficult, but it is expected to cause dissipation into the DQD due to its incoherence, as well as lead to a tunneling-like capacitance associated with these excitations in addition to quantum capacitance arising from the mixed state of the system.

3.5 Other Capacitive Effects

In experiment, it was found that in many regimes, a resonator coupled to one quantum dot's plunger gate was sensitive to *lead* transitions on the other dot in a DQD setup, despite the charge transfer not even involving the probed dot. Furthermore, despite this being explicable according to Equation (2.18) for significant cross-capacitances of one dot's gate to the other dot, cross-capacitance was found to be negligible in experiment. Interestingly, numerical simulations suggested this was a result of tunnel coupling between the dots. As the tunnel coupling between dot levels increases, the range of level detuning over which the levels are still hybridized with each other becomes larger. When an electron tunnels onto one dot within this range from a lead, then, the other dot's state is altered as well, since the new electron's wave function is delocalized into the other dot to some degree. We depict this with numerical simulations using the model of Appendix B in Figure 3.9 for different tunnel couplings.

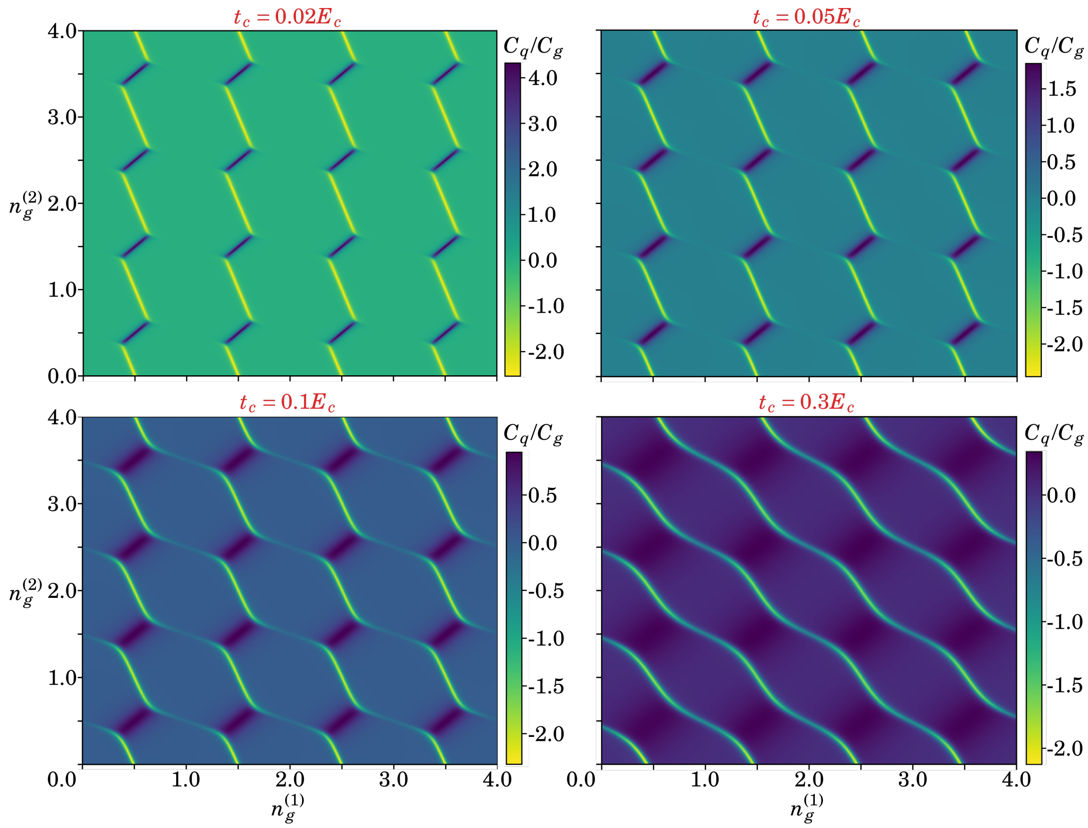

FIGURE 3.9: Simulated zero temperature quantum capacitance charge stability diagrams for two non-degenerate dots with charging energies $E_{c1} = E_{c2} = E_c$, mutual capacitance energy $E_m = 0.7E_c$, and tunnel coupling to quasi-leads $0.02E_c$, as a function of reduced gate voltages $n_g^{(1),(2)}$. The tunnel coupling between the dots, t_c is increased from top left to bottom right. The capacitance is probed from dot 1, and the gates have no cross-capacitance with each other. For weaker tunnelings, this is why lead transitions to dot 1 are visible but those to dot 2 are not. At stronger tunnel couplings, electrons become delocalized between the two dots and dot 1's gate is sensitive to lead transitions onto dot 2 as well.

Chapter 4

Experimental Results

HEREIN, we present transport and Dispersive Gate Sensing (DGS) measurements of electron tunneling in a Normal-Superconducting-Normal triple quantum dot device, focusing on the regime where it is tuned as a Double Quantum Dot (DQD). As mentioned previously, readout and braiding of a Majorana parity-based qubit requires measuring an effective tunnel coupling from a quantum dot through Majorana zero modes to another quantum dot. Understanding all factors which modulate the effective tunnel coupling between a dot and superconducting island is therefore critical. Another necessary condition for the implementation of such a qubit is that levels in a quantum dot can be controllably hybridized with subgap states in a superconductor. To work towards meeting these conditions, we begin by characterizing our device and identifying various parity-dependent tunneling processes described in Chapter 3. Next, we demonstrate hybridization between a subgap state of a superconducting island and a quantum dot level, and observe evolution of the state with increasing magnetic fields. Along the way, we analyze changes in the resonator lineshape as it responds to changes in the subgap state's energy and degeneracy.

4.1 Experimental Setup & Methods

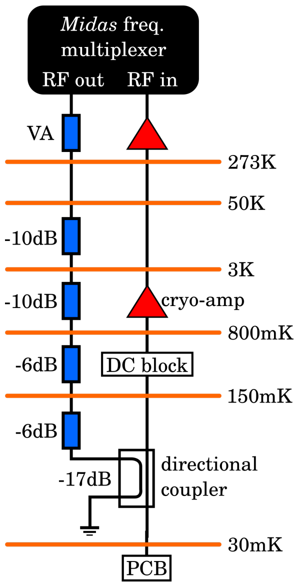

FIGURE 4.1: Attenuation and amplification at each temperature stage of the RF circuit, down to the PCB.

Measurements are performed in a dry dilution refrigerator from Leiden Cryogenics at its base temperature of about 20mK. Initial cooling to roughly 4 K is performed via pulse tube vacuum pump refrigeration, while the final cooling stage is accomplished with the help of a mixture of helium-3 and helium-4 in the so-called 'mixing chamber'. At this stage, a helium-3 rich condensed phase is separated from a dilute phase by a phase boundary. Pumping helium-3 from the dilute phase causes helium-3 from the condensed phase to cross the phase boundary, pulling latent heat out of the mixture.

DC voltages are controlled with the help of a set of Digital to Analog Converters (DACs) followed by filtering and attenuation at various steps of cooling in the refrigerator in order to reduce thermal noise seen by the sample. Similarly, RF signals are filtered at each temperature stage of the refrigerator to reduce noise, and amplified both at 4K by a cryogenic amplifier and again at room temperature, see Figure 4.1. The DC block prevents low frequency carriers from being transmitted in either direction. A Printed Circuit Board (PCB) provides the electronic interface connecting input cables to bonds on the sample, and includes bias tees which combine the oscillating RF and DC signals without DC components from the RF line (or vice versa) contributing to the output.

A *Midas* frequency multiplexer both serves as the RF source and measurement apparatus. It is capable of mixing 8 controllable frequencies and sending them down a single RF line, while it also separates the signals into each probe frequency's component in the return signal. This enables us to simultaneously probe multiple resonators provided they are not too close in frequency. Including the Midas' output signal of -23 dBm, depending on the Variable Attenuator (VA) settings used in the signal chain, RF power at the sample level was estimated to be between -123 and -128 dBm, relative to a 50 Ω transmission line. In terms of voltages, this translates to a swing of δV_g between 90-160 nV. Midas obtains the in-phase and quadrature (I and Q) components of the return signal, from which the phase and amplitude of the reflected signal are calculated.

4.2 The Normal-Superconducting Double Dot Device

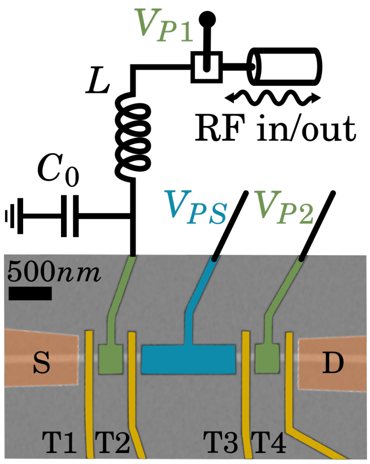

FIGURE 4.2: SEM image of triple dot device with gate design superimposed in color and DGS resonator circuit shown above. Between Source (S) and Drain (D) leads, three dots may be defined and controlled by tunnel cutter gates ($T1-T4$) and plunger gates V_{P1}, V_{P2}, V_{PS}. V_{PS} possesses its own resonator circuit with a different resonant frequency.

We conducted DGS and direct current measurements of a hybrid normal-superconducting dot device, pictured in Figure 4.2. Since the fabrication recipe was not a focus of its research, and in fact is identical to that used in [43, 55] aside from different dot lengths, we only briefly summarize it here.

A roughly 140 nm thick indium-arsenide nanowire was positioned on a silicon wafer coated with 20 nm of silicon-nitride dielectric. This wire has an epitaxially grown 10 nm aluminum shell on two facets with all but a 1.1 μm long segment etched away, defining the superconducting charge island. Leads are composed of a 10 nm titanium sticking layer covered with 150 nm gold, deposited after an argon milling step to improve contact with the wire. Coating all this is a 10 nm aluminum oxide dielectric layer formed with atomic layer deposition, made as thin as possible to maximize the gates' lever arms. As with the leads, the plunger and cutter gates are composed of 10 nm titanium covered with 150 nm gold. The semiconducting dots' sizes are defined by their 290nm wide wrap gates, up to variations due to the differing voltages applied to them and the tunnel gates.

Off-chip superconducting resonators patterned with niobium spiral inductors on a sapphire substrate were used in the DGS circuits, where the resonators' capacitance is composed of its parasitic capacitance to ground in parallel with any parametric capacitance of coupled dots [56]. Two such resonators with characteristic frequencies of roughly $\omega_{P1} = 2\pi \cdot 449$ MHz and $\omega_{PS} = 2\pi \cdot 525$ MHz were bonded to plunger gates V_{P1} and V_{PS}, respectively. The amplitude response of the resonator circuit is shown in Figure F.1.

To begin, we characterized individual charge islands with a combination of current measurements and reflectometry measurements of each resonator. To define dots, it is

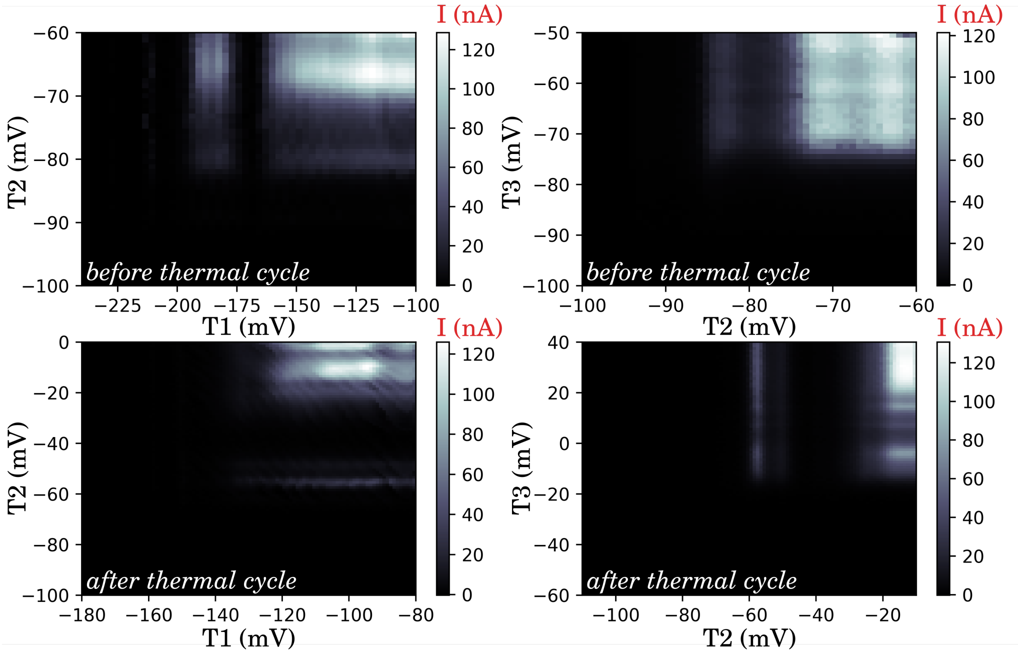

FIGURE 4.3: Current 'pinchoff' maps as a function of tunnel gates bordering the QD (T1 and T2, left) and those bordering the SCI (T2 and T3, right). As a result of necessary dilution refrigerator maintenance, the sample was thermally cycled once during this experiment. Upon cooling back down to base temperature, pinchoff traces were shifted to more positive voltages, indicating that the wire became less conductive after the cycle. Consequently, there are instances in this thesis where similar tunneling regimes were found for tunnel gate settings offset by upwards of 50mV. In both cases, pinchoff traces showed very little hysteresis in sweeping tunnel gates forward and backward in a single scan.

necessary to determine which ranges of the tunnel gate voltages (T1, T2, T3, and T4) enforce weak tunneling across them. To this end, we measure voltage pinchoff curves, given in Figure 4.3. Since the experiments conducted here are focused on a DQD consisting of a Quantum Dot (QD, defined by V_{P1}) and Superconducting Charge Island (SCI, defined by V_{PS}), we only present pinchoff curves for $T1$ to $T3$, simply setting $T4$ and V_{P2} to positive voltages to 'open up' that wire segment into behaving as a lead. This was accomplished with varying success, since we found every tunnel barrier to contain intrinsic quantum dots, see Figure F.3 for relevant tunneling spectroscopy data. To avoid such 'dotty' barriers, we simply tuned the tunnel gates away from any resonant spots where charges appeared to be tunneling to a third, unwanted dot. Hereon, we identify the V_{P1} dot as *the QD* and the Superconducting Charge Island as *the SCI*.

Based on the pinchoff traces, dots are defined by setting their respective tunnel gates to voltages near those where current is almost completely closed off, denoted the *pinchoff* voltage. From here, a natural method of characterization of charge islands is with Coulomb diamonds: the islands are swept through several charge states via their plunger gates, while bias voltage V_{bias} is also swept. This results in characteristic 'diamond' shaped features in the measured current or RF signal. The height of these diamonds in bias is simply twice the addition energy E_a, while their width is simply E_a divided by the gate lever arm α [24]. Coulomb diamonds therefore allow us to estimate these parameters, while features at higher bias indicate the presence of additional tunneling channels, such as excited states in the dot or quasiparticles in the SCI. Furthermore, the difference in addition energy between successive Coulomb

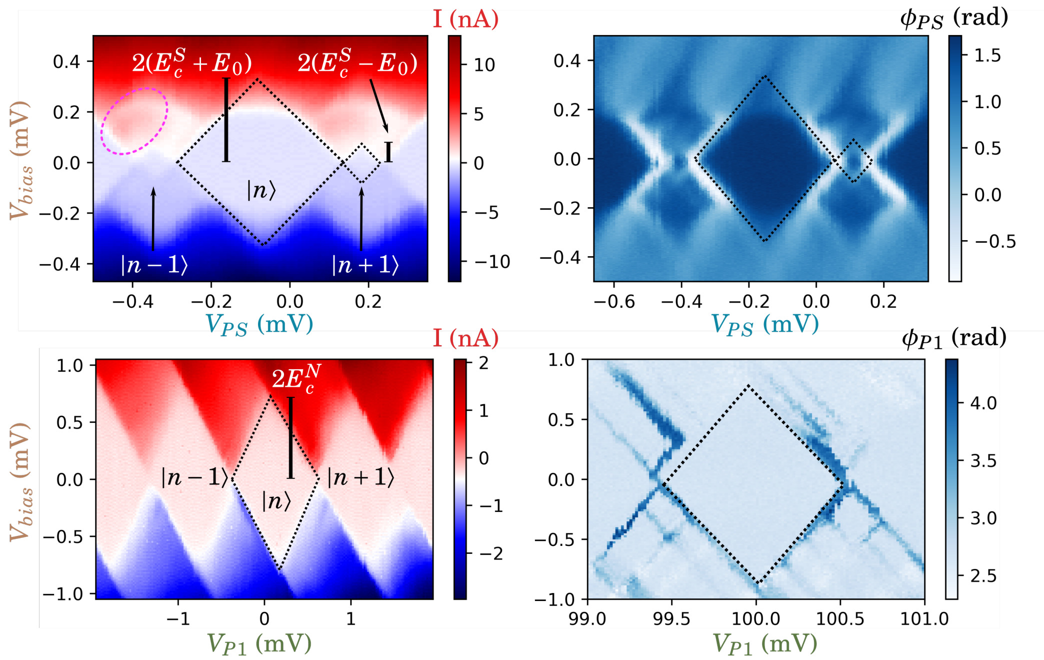

FIGURE 4.4: SCI Coulomb diamonds (top) with $\vec{T} \equiv (T1, T2, T3, T4) = (450, -84, -75, 450)$mV measured with current (left) and $\vec{T} = (450, -83, -74, 450)$mV measured with V_{PS} phase response. Likewise, below are QD diamonds with $\vec{T} = (-184, -84, 0, 0)$mV and $\vec{T} = (-120, -25, 100, 100)$mV for the DC and RF phase measurements, respectively. From these diamonds we estimate $E_0 \sim 70\mu$eV, $E_c^S \sim 90\mu$eV, and $E_c^N \sim 360\mu$eV. Ordinarily, one can estimate the induced gap of the SCI from the bias point where $1e$ periodicity in Coulomb oscillations begins, however in our device the gap is ‘soft’ at these voltages, making this irrelevant. In the normal dot, particularly from the RF V_{P1} phase diamonds, lines running parallel to the diamond edges either indicate transport through orbital excitations in the dot, or from the dot’s drain lead being partially superconducting with subgap states. When diamonds are skewed in one direction and one diagonal edge of the diamond supports more current than another this is indicative of a mismatch in tunnel coupling and capacitance to the source and drain. The swelling of current in part of the SC diamonds may be a sign of negative differential conductance, known to arise from quasiparticle excitations occupying and thus blocking transport channels [57].

diamonds is proportional to their orbital energy difference, since the charging energies cancel. For superconductors with lowest quasiparticle state energy $E_0 < E_C^S$ (the SCI charging energy), this difference is proportional to E_0. Specifically, it is $\Delta E = E_C + E_0 - (E_C - E_0) = 2E_0$.

Two typical diamond scans for the QD and SCI are displayed in Figure 4.4, both for DC and RF measurement. From these and other diamonds, we estimate that the lever arms of the P1 and PS gates are both > 70%, increasing as the dots are depleted at more negative voltages, where charging energies also tend to increase. These large lever arms facilitate the sensitivity of DGS measurements, as evidenced by the large phase shifts observed in their resonators in Figure 4.4. Note that in some cases we take the phase data modulo 2π to make color scales more clear.

As is noted from the SCI diamonds, for V_{PS} near zero volts there is a subgap state of some energy. Considering the differential conductance of the above scans dI/dV_{bias}, the SCI appeared to have a ‘soft’ gap based on the lack of coherence peaks indicative of a diverging BCS density of states. In other words, enough clustered subgap states are present that the superconducting energy gap is not clearly defined. It has been shown that the superconducting shell's coupling to the underlying nanowire is markedly increased when the electrons' wave functions are 'pushed' towards the shell by applying a negative gate voltage opposite to the shell [58]. For near-zero voltages then, it is no surprise that there is a soft gap. Contrary to this, we note that current is relatively flat outside of Coulomb blockade in the odd regime of the SCI, other than the negative dI/dV feature. This hints that a single subgap state at low energy is well energetically separated from higher energy states, since otherwise the current would continue to rise in this region.

To shed some light on the nature of the E_0 subgap state, it is helpful to consider two limits. First, in the limit of a nanowire completely decoupled from the Al shell, there is no superconductivity, and all orbital states are simply 'dot-like' states in the semiconductor. An even-odd spacing effect can still be observed without proximitized superconductivity due to the presence of an effective triple quantum dot [59], where the Al shell behaves as a third charge island. On the other hand, when complete proximitized superconductivity is achieved through strong coupling between the shell and wire, there is a hard gap and therefore no subgap states. From this, and data to be shown later, we note that the subgap state (or states) is likely better described as a dot orbital tunnel-coupled with the superconducting shell than as an Andreev bound state. To demonstrate hybridization between an SCI subgap state and a QD orbital, however, it is not necessary for it to be an Andreev state.

Before proceeding to double dot measurements, it is important to note that for $E_0, E_c - E_0 \gg k_B T$, we can control with negligible uncertainty the quasiparticle occupation of the SCI, neglecting any quasiparticle poisoning from non-thermal effects while our superconductor is in Coulomb blockade with respect to the leads[1] [60]. In the center of a Coulomb valley (tallest part of a Coulomb diamond) at zero bias, the energetic cost of an electron tunneling into the SCI is either $E_c^S + E_0$ or $E_c^S - E_0$, depending on if the island parity is even or odd, respectively. As well as that, the only route by which a Cooper pair could split and occupy a quasiparticle state is through an energy cost of at least E_0, depending on if the other electron tunnels to the lead or another quasiparticle state. When all of these energy scales are larger than temperature, there is thus exponentially vanishing probability of the quasiparticle occupation being zero (one) for an odd (even) parity Coulomb diamond. The conclusion is precisely what was noted in Section 3.4: any Coulomb resonance of the SCI must involve tunneling between the BCS condensate of the superconductor and a state with a single quasiparticle. In the following section, we exploit this fact to correlate the charge parity of the SCI with its tunnel coupling to dot orbitals and leads.

4.3 Parity-Dependent Tunneling

One important tool by which we probe tunneling between the SCI and its coupled QD is with Charge Stability Diagrams (CSDs) given by DGS measurements. Sweeping the gate voltages of both islands, we measure tunneling between them. The regions of suppressed tunneling identify stable charge states, while boundaries between stable charge regions reveal information about tunneling processes occurring. Imperfections in the resonator such as stray resonances distort the resonator response, making its phase and amplitude response non-monotonic. This prevents us from extracting quantitative results from DGS CSDs relating to tunnel couplings, but variations in this

[1] Note however, that finite but relatively large (on the timescale of RF measurement) quasiparticle poisoning times have been observed for an SCI mostly decoupled from leads of $> 10\mu s$ [46].

response nonetheless grant a qualitative picture of quantum transport in the system. To inspect more closely features of interest, we conduct frequency sweeps around these features, since the shift in the resonator's amplitude dip near resonance should still be a good measure of the shift C_p in capacitance of the resonator $\Delta\omega \sim -(\omega_0/2)C_p/C_0$, see Figure 2.4b.

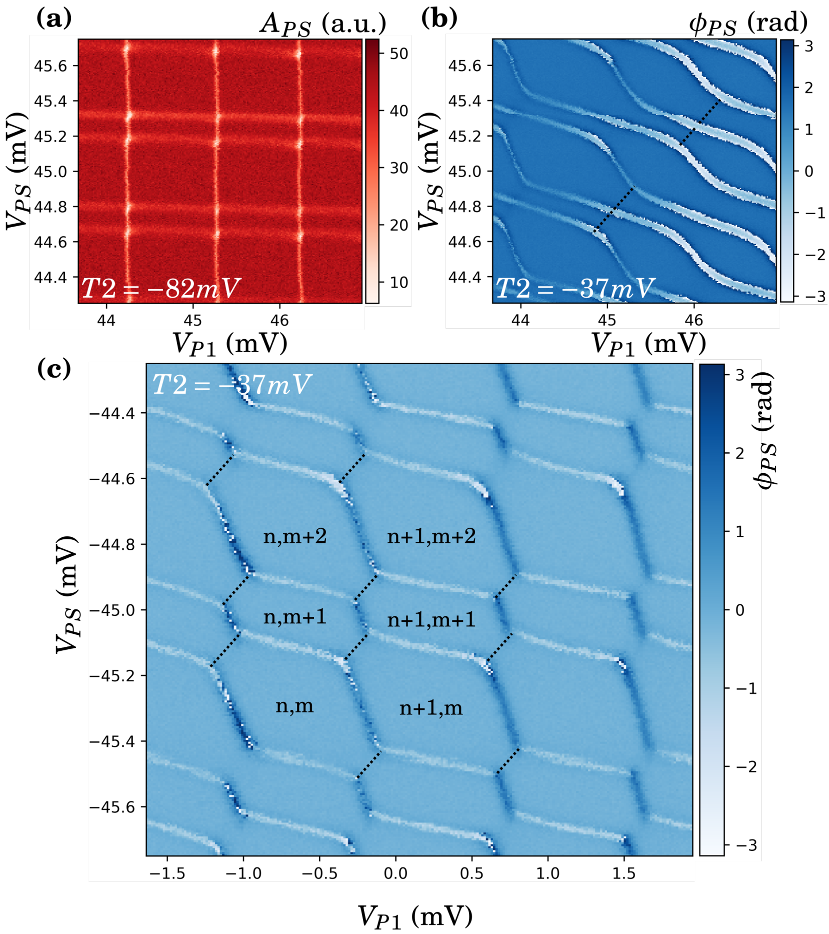

FIGURE 4.5: Three CSDs taken with a previous RF signal generator and waveform digitizer instead of *Midas*: A *Rode & Schwarz SGS100A* and *AlazarTech ATS9870*, respectively. Charge states of the dot (SCI) are shown as numbers n (m) with respect to some arbitrary charge state, and interdot transitions are drawn as dotted lines. In all diagrams, barriers of $T1 = -182$mV and $T3 = -73$mV enforce weak tunneling to the leads. Diagrams are shown for very weak interdot coupling in amplitude response A_{PS} **(a)**, strong coupling and mutual capacitance in phase response ϕ_{PS} **(b)**, and strong coupling in a more depleted SCI and QD regime **(c)**.

To get a broad picture of the system, however, three typical CSDs are given in Figure 4.5, where the resonator response of the V_{PS} resonator is measured through its reflected amplitude A_{PS} and phase ϕ_{PS}. From the CSD shown in Figure 4.5a in the weak interdot coupling regime, we see that the plunger gates $V_{P1(S)}$ have negligible cross capacitance to the opposite charge island, since otherwise V_{PS} would gate the QD and V_{P1} the SCI and the lead transitions would show a slope. Figure 4.5b is a CSD for very strong interdot coupling and mutual capacitance, where the two dots nearly behave as a single charge island gated by both V_{PS} and V_{P1}. Importantly, these two factors tend to suppress the QD-to-lead transitions when the *SCI* has odd parity. Also, in this regime the system is essentially a single charge island, part of which is superconducting and part of which isn't, making transport very complicated. Hence, we generally avoid such regimes.

Lastly, Figure 4.5c shows a CSD for a more depleted QD and SCI. QD-to-lead transitions are not suppressed for the odd parity SCI, since the odd parity state is more stable at these gate settings, having an energy closer to the SCI nanowire's Fermi level. In all cases, however, note that the SCI resonator is sensitive to lead transitions on the QD despite having little cross-capacitance to it. As proposed in Section 3.5, this is a result of electronic wave functions being spread between the two islands at stronger tunnel couplings.

4.3.1 Peak-Fitting Models

Subsequent analysis in this thesis is heavily based on the positioning and width of our V_{P1} resonator's response, and on our ability to pinpoint charge transition positions in gate-space. We thus explain the methods used for peak fitting before proceeding.

Uncertainty in evaluation of peak positions, be they in gate-space or frequency-space, depends on the fit function used. As we saw in Section 3.1, the parametric capacitance near an interdot transition should be a Lorentzian function of detuning ε, while Gonzalez-Zalba predicts a $1/\cosh^2(\varepsilon/k_B T)$ variation [23] for tunneling from a dot to a lead, itself a Lorentzian for small ε. Assuming small parametric capacitance, the phase shift seen by the resonator is proportional to C_p, making it Lorentzian as well. To approximately determine the peak position, we therefore heuristically fit with a Lorentzian function the complex resonator data $V = |V|e^{i\phi}$ formatted as $|V|\cos(\phi - \phi_{max})$ where ϕ_{max} is the maximum phase shift over the data set. By doing so, we make use of both the real and imaginary part of the complex reflected signal, since $|V|\cos(\phi - \phi_{max})$ is maximized for large phase *and* amplitude shifts. This model fits the peak centers very well using the least-squares method, so we estimate that the dominant uncertainty comes from uncertainty in the peak positioning due to broadening of the transitions. As a result, we overestimate the uncertainty in peak positioning to be simply $\pm\gamma_{max}/2 \approx 6\,\mu$V, half the largest FWHM γ_{max} across all peak fits in a data set.

Fitting the resonator frequency response, on the other hand, requires different approximations. We find in Appendix A that an ideal series resonator with some dissipation R in parallel with the capacitance C has a reflection coefficient with a square root Lorentzian-like dependence on the difference in probe frequency $\Delta\omega$ from the true resonance ω_0 characterizing the distribution's width:

$$|\Gamma| \sim \frac{\sqrt{(R - Z_0)^2 + 4L^2(\Delta\omega)^2}}{\sqrt{(R + Z_0)^2 + 4L^2(\Delta\omega)^2}}, \qquad \Delta\omega \ll \omega_0 \quad (4.1)$$

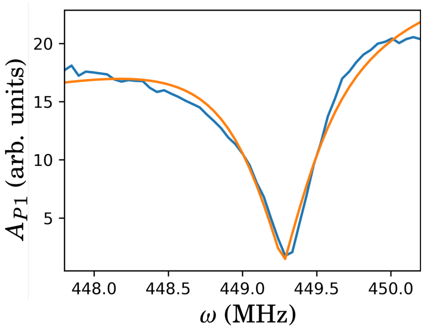

FIGURE 4.6: A typical fit (orange) of the V_{P1} resonance in amplitude using eq. (4.2). Original data is in blue.

In practice, other resonances contribute to a varying background in the resonator response, so the V_{P1} resonance is clearly not completely described by Equation (4.1) (see Figure F.1). We nonetheless fit the V_{P1} resonator response with a function of the form:

$$f(\omega) = f_0 + b(\omega - \omega_0) + A|\omega - \omega_0|/\sqrt{(3/4)\gamma^2 + (\omega - \omega_0)^2} \quad (4.2)$$

with two fit parameters A and γ determining the scale and FWHM of the distribution while ω_0 is its center and f_0 is an offset. We implicitly approximate the resonator dissipation as being matched with the transition line impedance to reduce the number of fit parameters. The term fitted with b accounts for the varying background of the RF response, approximated as linear on the scale of the V_{P1} resonance width. To provide an upper bound on the fit parameters' uncertainties, we therefore include a rough estimate of the scale of the RF background's variation as the difference between minimum and maximum values that $b(\omega-\omega_0)$ achieves over the width of the ω sweep, and include this as uncertainty in the amplitude data at each frequency point. This is then translated to uncertainty in the fit parameters through the standard deviation calculated by the least-squares fitting algorithm used. An example of one of these fits is in Figure 4.6.

4.3.2 Tunneling into the Superconducting Condensate

In addition to the obvious even-odd spacings characteristic to an SCI with a low energy subgap state, the amplitude and phase response of the resonator often alternated between successive charge transitions, begging the question of whether this too was related to superconductivity. Towards an affirmative conclusion, we discussed in Section 3.4 the possibility for electron-like and hole-like coherence factors (u and v, respectively) of the subgap state modulating tunneling into and out of it when the superconductor has quantized charge. Some of our measurements also supported this, shown in Figures 4.7a and 4.7b.

SCI-to-lead transitions were found to frequently display an even-odd phase response difference, but these transitions are subject to the inherent incoherence of tunneling into a lead. Information about the electron tunnel rate into the lead is then obscured by thermal effects [23], rendering this method of measuring coherence factors no more revealing than conductance based methods [54]. Optimistically, the fact that there is a difference at all is nonetheless suggestive of a coherence factor dependent tunneling. Probing even-odd frequency responses is possible when tunneling to a coupled QD, however, and the spin effect described in the following section only alters the effective interdot tunnel coupling when the *total* DQD parity is changed. Motivated by this, we pinched off both leads by setting tunnel gates to strongly negative voltages, fixing the DQD's total parity.

In the floating DQD regime, CSDs consist solely of interdot transitions (Figure 4.7b), so that a sweep of either V_{PS} or V_{P1} crosses interdot transitions. Even-odd peak heights in frequency response were sometimes observed in such sweeps, see Figures 4.7c and 4.7d, but these patterns only persisted over a few charge transitions at a time. Furthermore, alternating tunnel couplings can be explained by, for example, tunnel coupling to the QD being dependent on if an empty or half-full spin-degenerate orbital is being filled. Thus, to truly isolate effects from the coherence factors, a single QD charge state should be tunneled into for each successive SCI charge transition. This could be accomplished with a 'side-loading' experiment, discussed in Section 5.1.

Another unexpected feature of the resonator frequency response across interdot transitions is that in many cases, the resonance becomes *less* broad at these transitions, shown in Figure 4.7e. It is possible that low-lying excitations are occupied due to driving by the RF signal when the dots are decoupled, and that bringing the dots near resonance allows the ground state to lower its energy at an anticrossing, preventing population of excited states and thus dissipation. An example of a Hamiltonian leading to this phenomena is that of a single dot orbital coupled to a nearly-degenerate continuum of states, whose spectrum is shown back in Figure 3.5. When the nearly

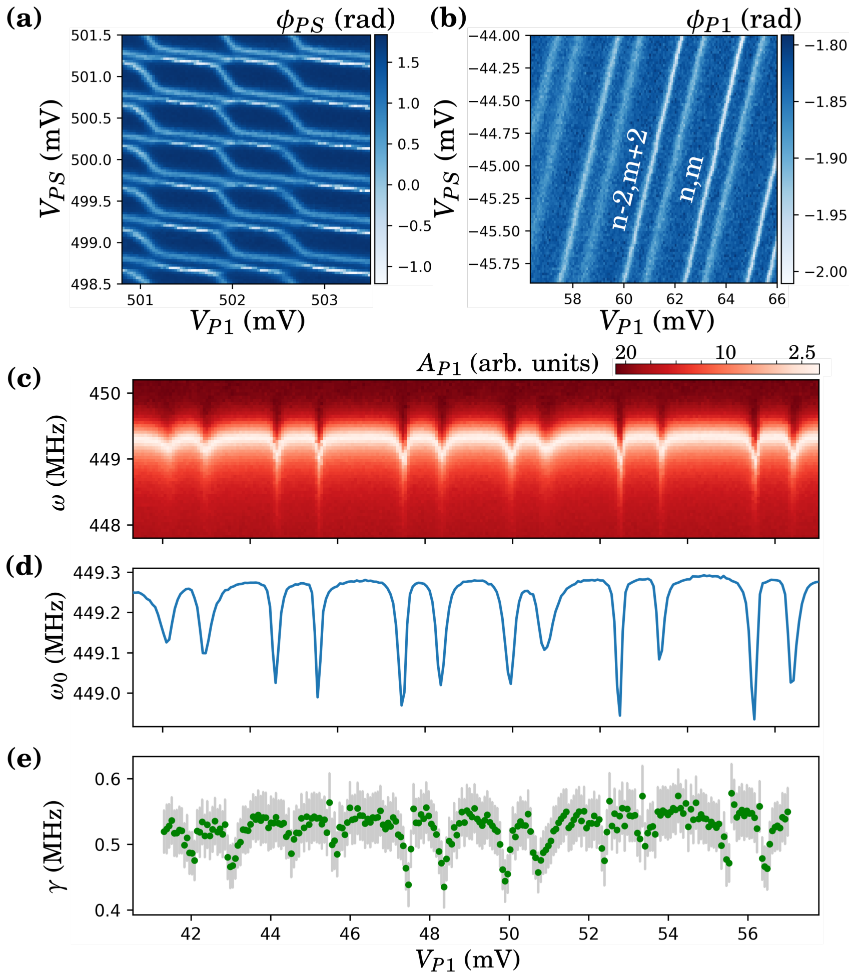

FIGURE 4.7: **(a)** and **(b)** are CSDs for weakly coupled ($T1, T3 = -100, +3\,\mathrm{mV}$) and pinched off ($T1, T3 = -280, -173\,\mathrm{mV}$) leads, respectively. Numbers in **(b)** indicate relative DQD charge states. **(c-e)** Frequency sweep along with V_{P1} in the floating regime, with fitted resonance frequencies ω_0 **(d)**, and full widths at half maxima γ **(e)**.

degenerate states themselves are independent, the electron's ground state energy is lowered away from the continuum states by spreading its wave function across each state, creating an energy gap.

4.3.3 Zero-Field Spin-Dependent Tunneling

In order to focus on the interdot transitions between the SCI and QD, the SCI's lead was pinched off by setting $T4 = -400$mV, so that lead transitions from the SCI could only occur by direct tunneling to the source or via cotunneling through the QD. Fairly strong coupling was created between the QD and SCI by setting $T2 = 10mV$, while $T1 = -100$mV was set to enforce weak dot-to-lead tunnneling. Unfortunately, it was found that the V_{PS} resonator was still fairly insensitive to interdot transitions in this regime, see Figure F.2. Furthermore, because all CSDs were taken in the vicinity of 500mV on each plunger gate, the SCI's subgap state is likely dominated by the physics of the InAs semiconductor.

Once again, we therefore focused on the V_{P1} resonator, which revealed a surprising zero-field spin effect on the interdot tunneling. In the phase response of V_{P1} it was noted that interdot transitions showed a stronger or weaker shift depending on the total charge parity of the DQD, see Figure 4.9a. In this regime, spacings between QD charge states also showed an even-odd effect, hinting that the dot is well described by independent spin-degenerate levels separated by a significant orbital energy. This, combined with the already established even-odd spacings of the SCI, allows the determination of the total DQD charge parity based on the size of a given charge state's hexagon in a CSD. We observed that for odd total parity, the phase shift at transitions was weaker than for even parity.

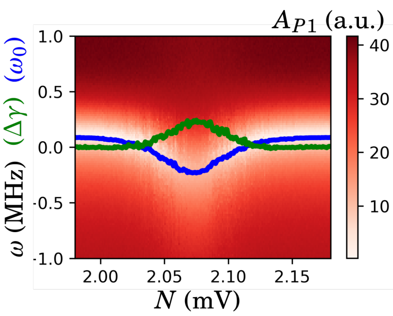

FIGURE 4.8: Sweep across a lead transition at $\varepsilon = 1.37$mV, along with fitted resonance frequencies ω_0 and FWHM shifts $\Delta\gamma$ at each N points. From this we extract a maximum frequency shift of $\Delta\omega_{max} = -321 \pm 5$ kHz and broadening of $\Delta\gamma_{max} = 240 \pm 40$ kHz.

To further investigate, we selected nine pairs of interdot transitions (boxes in Figure 4.9a), and conducted 3-dimensional CSD sweeps, with a frequency sweep about the V_{P1} resonance on the third axis. At each point in the stability diagram, the resonator was fit with the function $f(\omega)$ described in Section 4.3.1 to extract the resonance's FWHM and and characteristic frequency. As is evident from Equation (4.1), larger FWHM values correspond to increased internal dissipation in the resonator, while from early theoretical discussions we predict the frequency shift is proportional to tunneling or quantum capacitance. In order to facilitate study of the interdot transitions while neglecting lead transitions, we rotate our gate voltage coordinates, using the slopes of SCI and QD lead transitions in earlier CSDs as the transformation parameters. Incidentally, the rotation matrix used:

$$\begin{pmatrix} \varepsilon \\ N \end{pmatrix} = R(-126.9^\circ)\begin{pmatrix} V_{P1} - 500\,\text{mV} \\ V_{PS} - 500\,\text{mV} \end{pmatrix}, \quad R(\theta) = \begin{pmatrix} \cos(\theta) & -\sin(\theta) \\ \sin(\theta) & \cos(\theta) \end{pmatrix} \tag{4.3}$$

effectively mirrored the V_{PS} axis. This establishes an ε axis, corresponding to detuning from interdot transitions, and an N axis, it's orthogonal partner which is perpendicular to QD lead transitions. As a baseline, we sweep N across a lead transition, taking a frequency sweep at each N point, an example of which is in Figure 4.8. In this way we

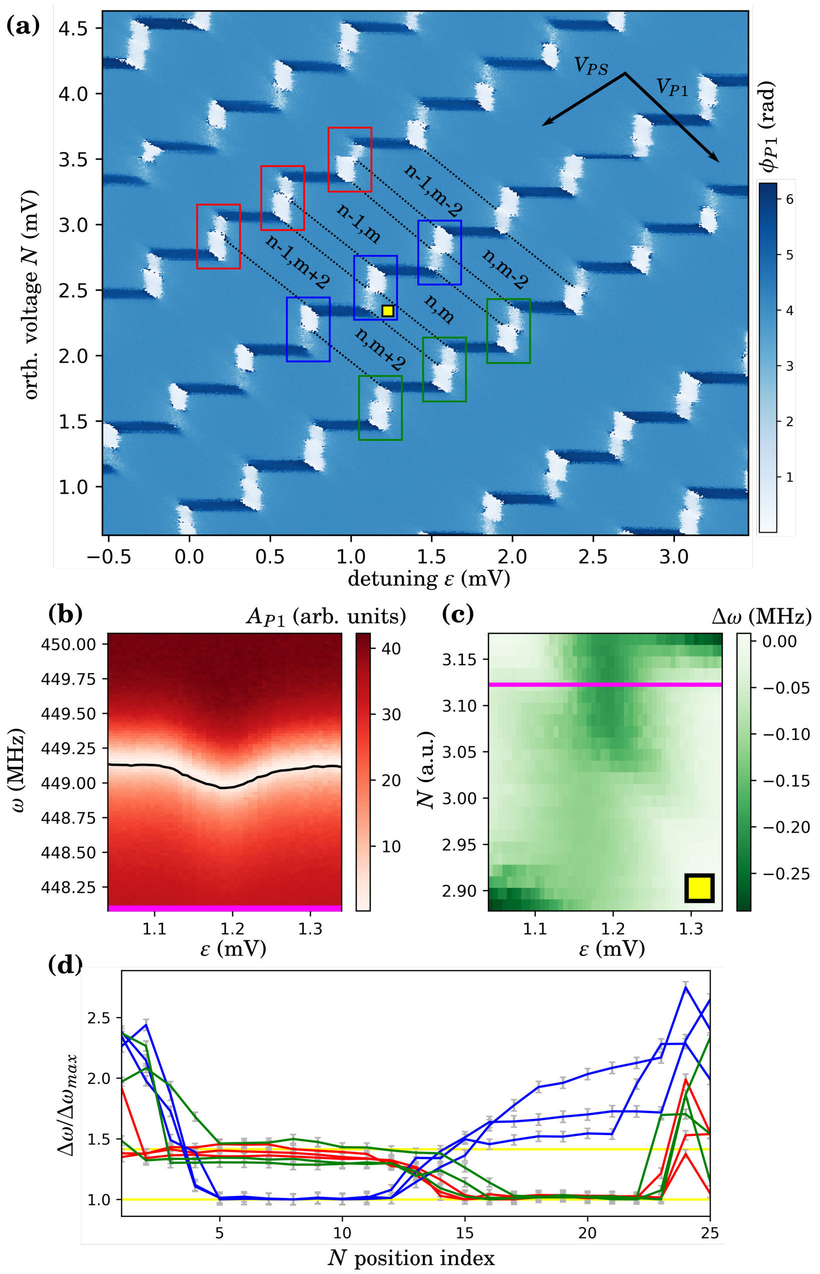

FIGURE 4.9: **(a)** Phase response in the DQD with the SCI lead pinched off, demonstrating the zero-field spin degeneracy effect on interdot tunneling. Indices (n, m) denote the charge state of the dot and SCI relative to some arbitrary center, respectively. Interdot transitions show an alternately strong or weak phase shift dependent on the total DQD parity. Voltage coordinates are rotated to create an artificial axis ε representing detuning from interdot transitions, as well as its orthogonal axis N. Boxes denote the nine pairs of interdot transitions chosen for frequency-space analysis. **(b)** is a slice of the 3-D charge stability diagram of the central transition pair, with a frequency sweep about the V_{P1} resonance on the third axis. At each (N, ε) point, the amplitude response is fitted to find the frequency shift, plotted relative to the frequency in Coulomb blockade in **(c)**. In **(d)**, we select the maximum frequency shift at each N value from each 3D transition pair scan, plotting it relative to the minimum frequency shift at each N. Colors correspond to the transition pair in **(a)**, while the yellow lines show the expected relative values of $\sqrt{2}$ and 1. Near the edges, lead transitions can clearly be seen to induce stronger frequency shifts than the interdot transitions.

establish the level of dissipation (γ) and frequency shift expected for lead transitions, namely, that both are larger compared to interdot transitions.

Cottet *et al* and our model from Section 3.1 both predict a zero-field spin effect dependent on the total parity of a DQD [48]. Particularly, these models predict the effective interdot tunnel coupling to be a factor of $\sqrt{2}$ larger for even total DQD parity, since in this case either spin up or spin down electrons can tunnel between the dots, introducing a 2-fold degeneracy. To our knowledge, this effect has not been previously observed in experiment before for two related reasons.

First, to distinguish between tunnel couplings $\sqrt{2}t_c$ and t_c, the tunnel coupling t_c must remain constant over many charge transitions in order to establish this effect as a pattern. This requires operating in the many-electron regime, where the orbital wave-functions at subsequent charge numbers show little variation. Unfortunately, in the many-electron regime it is often the case that excited states of the n-charge dot state are within $k_B T$ of the ground state, making spin effects unresolvable. Conversely, in the few-electron (< 100 electrons) regime the tunnel coupling commonly varies significantly from transition to transition, though the presence of energetically-separated spin-degenerate levels has enabled observation of a spin-blockade effect at field with DGS [61, 62]. Possibly, the presence of a subgap state in an SCI constitutes a 2-fold degenerate level at zero field, even in the many-electron regime. This is due to the coherence of the even parity SCI states simply being a Cooper pair condensate, separated by E_0 from its first excited state. The quasiparticle state at E_0, on the other hand, may be clustered next to several low energy quasiparticle excitations, though in that case observation of the spin-effect is unlikely due to thermal excitations.

Performing these measurements, results support the observation of this zero-field spin effect, albeit inconclusively. Six of the nine interdot transition pairs showed reasonable agreement with a $\sqrt{2}$ difference in their frequency shifts, though the middle row had a significantly larger difference in shift. This could not be explained by contributions from lead transitions either, since the resonance broadening characteristic of lead transitions only appeared at the very edges of each scan, see Figure F.4. On the other hand, this unexpected discrepancy is consistent with a competition between tunnel couplings being modulated by the $\sqrt{2}$ spin degeneracy and differing u and v coherence factors of the subgap state. The former alternates based on the total DQD charge parity, while the latter changes based only on the SCI parity. Hence, the 'middle row' of interdot transitions differs from the other two precisely in whether or not the larger of u or v increases the frequency shift difference between the strong and weak shifts further, or makes it smaller.

As an example, we show a numerical simulation in Figure 4.10 where both spin effects and coherence-factor dependent tunnelings are present. This can lead to confusingly complicated patterns alternating with periods larger than just strong to weak and back, from charge state to charge state. We note, however, that these differences in experiment could also simply be caused by changes in the QD orbital between charge states.

In any case, the observation of this spin-degeneracy effect crucially requires coherent tunneling between two spin-degenerate levels[2]. This is therefore strong evidence that these measurements demonstrate coherent hybridization of a dot orbital with the subgap state of a superconducting charge island.

[2]The simulations of this effect, *eg.* that in Figure 3.4b, would not exhibit it if spin was not preserved, for example. For incoherent tunneling between many states, this is certainly the case, since different electrons may be involved in each tunneling event.

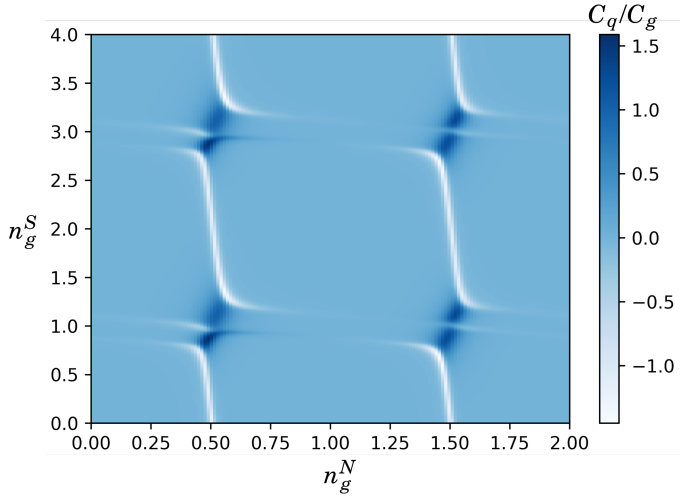

FIGURE 4.10: Simulated charge stability diagram for a normal dot coupled to a superconducting island with $E_c^S = (90/350)E_c^N$, $E_0 = (70/350)E_c^N$, $t_c = (20/350)E_c^N$, and $u = \sqrt{0.7}$, with quantum capacitance C_q probed from the normal island and with no cross-capacitance between gates. $n_g^{N(S)}$ are the dot's (SCI's) reduced gate voltages. The cancellation between t_c modulation from the spin degeneracy roughly removes the appearance of a 'spin' degeneracy effect in the interdot transitions on the right, while on the left they are distinctly resolvable by eye.

4.4 Evolution of Subgap State Transport with Field

Finally, we begin to study transport between the SCI and QD at non-zero magnetic field. Particularly, we are interested in the level of dissipation within the resonator when the SCI is metallic as opposed to when it has a discrete subgap state. Measurements are currently ongoing, but presently we have characterized the evolution of the subgap state energy in a regime where the QD lead is pinched off, see Figure 4.11. The field direction B_z is known to be within roughly 20 degrees of alignment with the nanowire's axis, based on how the sample was mounted in the dilution refrigerator. B_z and B_x therefore are 'nearly parallel' and 'mostly perpendicular' field directions, respectively.

From Figure 4.11, we see that the subgap state exhibits complex behavior as a function of field and V_{PS}. Recalling that the spacings between SCI lead transitions are proportional to $E_c \pm E_0$, the presence of two successive transitions of roughly the same width at $V_{PS} \approx 2 - 3$mV is indicative of the subgap state crossing zero energy at zero field. Extracting the level spacings as a function of field using the model described in Section 4.3.1, we observe the subgap state crossing zero energy multiple times, once, or being repelled from zero energy altogether, depending on V_{PS}. If E_0 was simply the induced gap on the SCI, it could not 'reopen' to non-zero energy after collapsing to zero energy. Thus, we have tracked a subgap state's energy as a function of field without direct transport through the DQD system.

Interestingly, the resonance point at $2 - 3$mV was consistently present across multiple measurements. Combined with previous observations that numerous disorder-based dots were present near the tunnel barriers in our system (see Figure F.3), and that we are operating at positive V_{PS} voltages, one possibility is that we are observing an effective triple dot. In other words, we may be observing a semiconductor dot state on the SCI tunnel coupled to the Al superconducting shell, which passes through a charge degeneracy point with the shell at this resonance. Additionally, a single subgap

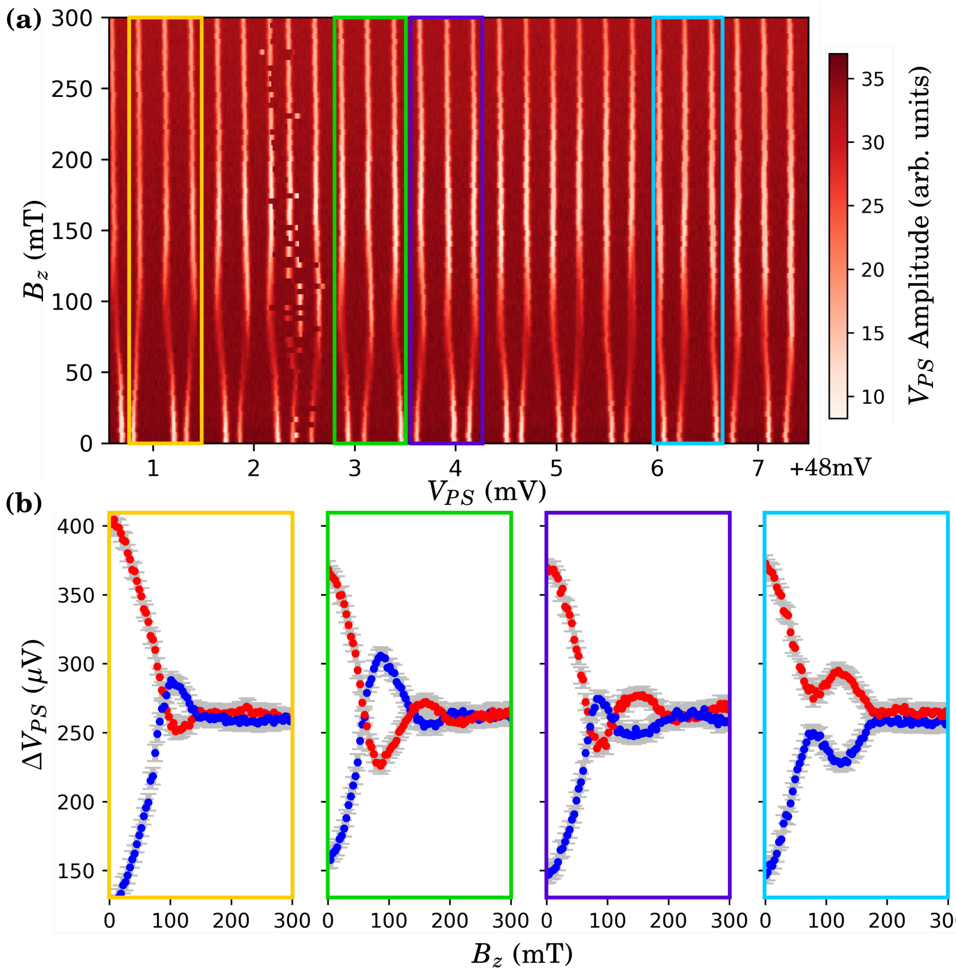

FIGURE 4.11: **(a)** SCI resonator amplitude response to lead transitions from the SCI evolving as a function of almost-parallel field B_z. **(b)** Selected fitted even (red) and odd (blue) spacings from the above scan. The colored boxes denote which transitions in **(a)** are fitted to the spacings shown in **(b)**.

state energy should evolve linearly with increasing but weak field strengths, so the curvature of the even-odd spacings as they close to zero is indicative either that the subgap state is being repelled by other higher energy states, or that mutiple states with distinct g-factors and energies are overtaking each other in approaching zero energy. Likely then, there are numerous subgap states clustered within the proximitized gap.

With the knowledge that a subgap state or small cluster of states with different g-factors is present in our superconductor, we compare the resonator frequency response for tunneling into this state with tunneling into the metallic continuum of Al at higher fields. Picking a single pair of interdot transitions for the half-closed off DQD at $(V_{P1}, V_{PS}) = (6, 51)$mV roughly, we take small charge stability diagrams where frequency is also swept about the V_{P1} resonance. Afterwards, we fit the resonance at each point in gate-space with eq. (4.2), extracting the resonance frequency ω_0 and FWHM γ. The results for various field strengths of B_x are given in Figure 4.13.

By conducting a sweep of V_{PS} versus field and extracting an even-odd spacing pair in the same region, we verify that the proximitized gap is closed at roughly $B_x = 50$ mT, see Figure 4.12. It is technically possible that B_x penetrates the Al shell more so from the side than perpendicular to its face, allowing superconductivity to persist at higher fields, but the lack of oscillations of the spacings about zero μV suggests otherwise. We do not expect to see Andreev bound states pinned at zero energy nor Majorana zero modes at such positive plunger voltages and low field strengths [63].

Curiously, the fitted FWHM reveal that the V_{P1} resonator obtains narrower amplitude response at interdot transitions compared to Coulomb blockade, giving the appearance of reduced internal dissipation at these points. Lead transitions, on the other hand, show starkly larger dissipation. This provides further evidence to the hypothesis that level hybridization at interdot transitions separates the ground state further in energy from excited states, decoupling the resonator from sources of dissipation such as higher-energy quasiparticle states.

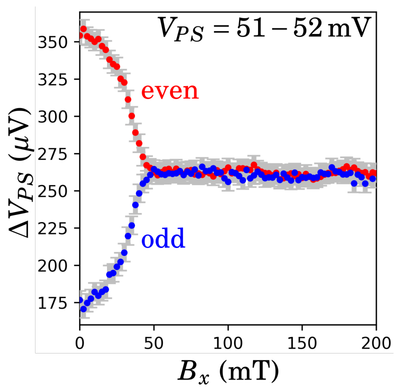

FIGURE 4.12: A typical extracted neighboring even-odd spacing of SCI-to-lead transitions as a function of nearly perpendicular field B_x in the weak tunneling $T3 = -14\,\mathrm{mV}$ regime.

As can be seen in Figure 4.13 from the γ fits, the resonator linewidth overall becomes broader as a function of field, due to B_x flux lines penetrating the resonator chip itself. Nonetheless, it is still clear that even at fields above 100 mT, placing gates at interdot transitions narrows the resonator linewidth. Unfortunately, this seems to indicate that γ is not a good measure of whether or not electron tunneling is occurring between discrete quantum states, since the SCI is almost certainly metallic at these field strengths.

To look more closely at the frequency response as a function of field, we select from each CSD in Figure 4.13 the maximum frequency shift relative to the resonance frequency ω_0 in Coulomb blockade for every value of V_{PS}, with the results pictured in Figure 4.14. At zero field, the frequency shift different between interdot transitions is roughly $\sqrt{2}$, as expected. With increasing fields, the 2-fold degenerate state develops a stronger frequency response due to the lifting of spin degeneracy, while the non-degenerate state shows comparatively less change. At fields above 50 mT, the SCI has become metallic, and so we see relatively little variation with even higher fields.

Moving on, we also fit the largest FWHM *shift* at each V_{PS} value (positive or negative), also shown in Figure 4.14. At all field strengths, upper and lower lead transitions from the CSDs are visible due to the Sisyphus dissipation into them. The central lead transition, which at low fields is energetically suppressed by mutual capacitance and tunnel coupling of the DQD in the odd-parity SCI regime, appears as a positive γ shift in between the interdot transitions. Even at high fields, however, the interdot transitions show a negative FWHM shift relative to Coulomb blockade.

Ongoing experiments with the same sample aim to conduct similar measurements with the more parallel B_z field, especially at field strengths where the subgap state is near energy.

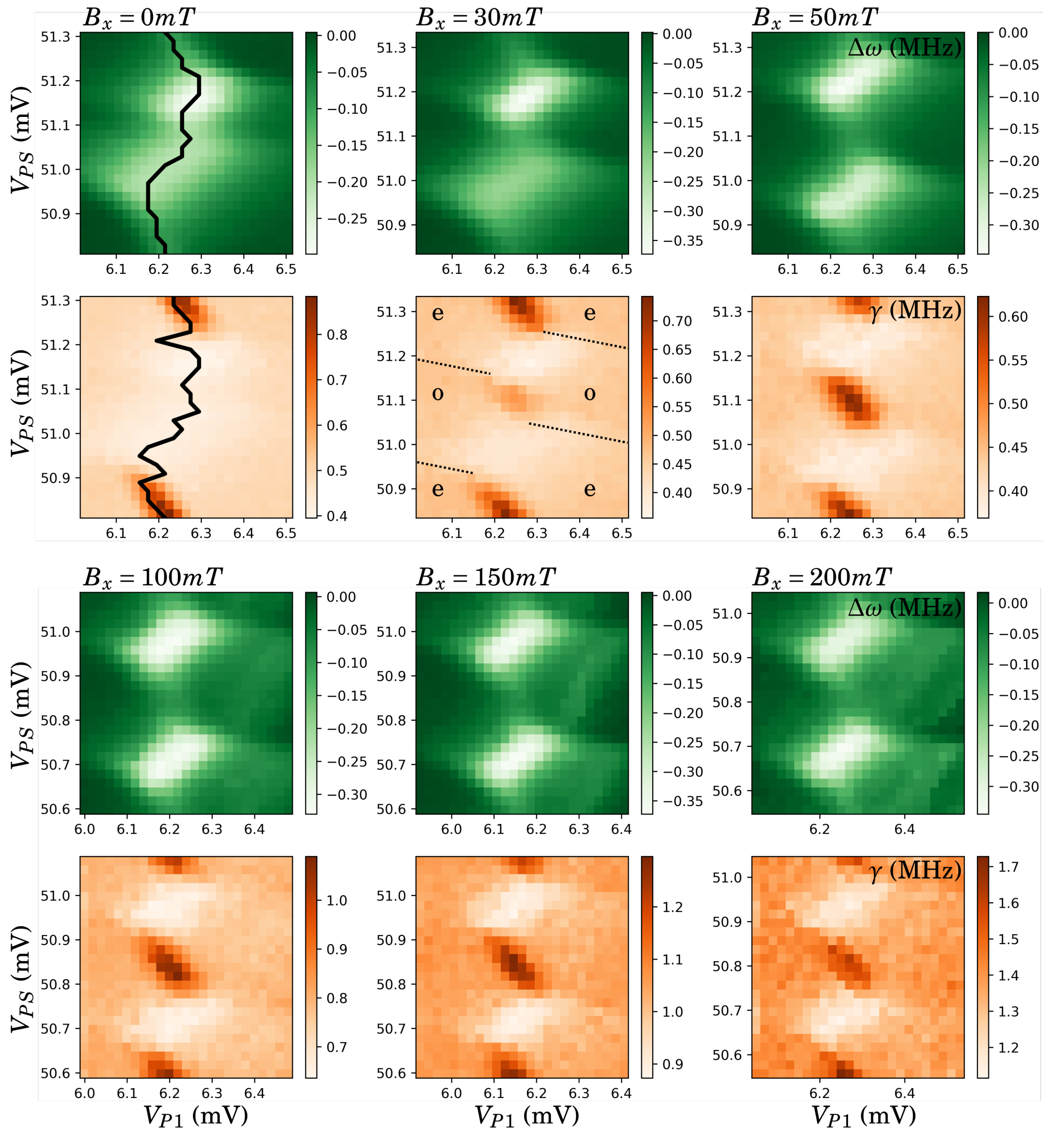

FIGURE 4.13: Frequency fits for each point in V_{P1},V_{PS} gate-space near a pair of interdot transitions at various nearly-perpendicular magnetic fields. Green color maps correspond to the fitted frequency shift $\Delta\omega$, while orange maps correspond to the fitted FWHM γ. Tunnel barriers are set to $(T1, T2, T3) = (-130, +12.1, -14)$mV to nearly pinch off the QD's lead. In the central CSD, less visible lead transitions are drawn in black as guides to the eye, with charge states indicated as having either odd (o) or even (e) SCI parity. Lines on the top left show an example of fitted positions of maximum frequency shift and γ shift used in Figure 4.14

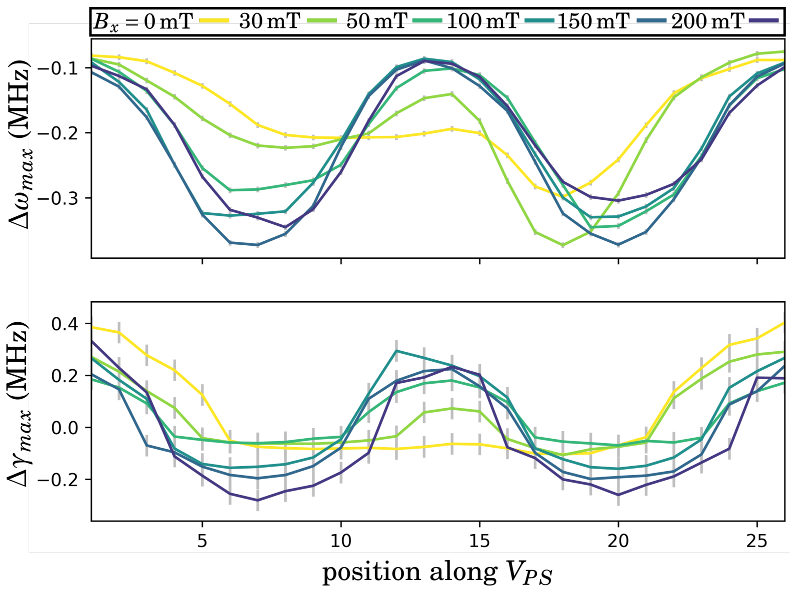

FIGURE 4.14: Maximum fitted frequency shifts and FWHM γ for each value of V_{PS} and B_x using the data from Figure 4.13.

Chapter 5

Conclusions & Outlook

In this thesis, we have scrutinized a relatively unexplored system for electron transport (with a couple exceptions [55, 64]): semiconductor-superconductor hybrid double charge islands. By making the charge islands tunable with tunnel cutter gates and plunger gates, we were granted a great deal of flexibility in studying these systems, which are essential components in some topological qubits.

With regards to theory, we found that quantization of charge in a superconducting charge island renders electron and hole-like excitations distinct, so that they modulate tunnel rates out of the island in a manner possibly detectable with Dispersive Gate Sensing (DGS). Signatures of this effect were observed in some voltage regimes of a hybrid double dot. Considering a dot orbital coupled to degenerate states, we found that the level of degeneracy directly translates to a change in quantum capacitance of the double dot. In experiment, we observed this for the case of a spin degeneracy, noting that this is only possible when discrete quantum states in both dots are hybridized. We considered the problem of a discrete dot orbital coupled to a nearly degenerate quasi-continuum of states with a master equation approach, and found that negligible dissipation is expected when interdot tunnel couplings are significant at finite temperature. This prediction is counter-intuitive, since low-lying excitations would likely be periodically occupied via Rabi driving from nearby plunger gates. Nonetheless, results thus far in an ongoing experiment supported this claim.

Contrary to our initial expectations, it is not universally the case that electron tunneling into a quasi-continuum of nearly degenerate states increases dissipation in a capacitively coupled resonator relative to when tunneling occurs between two discrete quantum states. We found in particular that dissipation was reduced at charge degeneracy points of the double island, even when the superconducting island was made metallic by applying a magnetic field. This puts into question the possibility of using DGS as a measure of tunneling coherence, since tunneling into a metal is certainly incoherent.

Towards the long term goal of constructing a topological qubit, we note that our observation of hybridization between a superconducting island's subgap state and a dot orbital is a necessary first step for using quantum dots as parity sensors for measurement based topological qubits.

5.1 Outlook

Hybrid semiconducting-superconducting dot systems open up a wealth of experimental possibilities for studying transport through subgap states such as Majorana zero modes. As examples, we mention two possible experiments.

First, by adding a second quantum dot next to a normal-superconducting double dot, the former can be used as a discrete electron reservoir for the second dot. With this tool, electrons can be loaded from a discrete quantum state onto the superconducting island without variations in the quantum state's character. This would allow isolation of various features of the island's ground state, enabling measurement of a subgap state's electron and hole-like coherence factors, for example.

Second, placing a second quantum dot at the other end of a superconducting island longer than its coherence length would make a unique cotunneling experiment possible. If further research proves that studying the frequency response of local DGS probes at either dot provides some quantitative measure to distinguish between coherent and incoherent transport, an electron teleportation experiment could be conducted [65]. Local DGS probes at either dot observing coherent cotunneling simultaneously must be coupled coherently through the central superconductor. Tuning the system into a regime expected to place the superconductor in a topological phase with a Majorana zero mode, this would provide strong evidence of electron teleportation through the fermionic mode formed by two Majorana quasiparticles.

Appendix A

Reflection Coefficient for an LC Resonator

Reflection from an Impedance Mismatch

Assuming the resonator is connected to a transmission line of standard impedance $Z_0 = 50\Omega$, the relation between the incident RF voltage $V_i = V_0 e^{-i\omega t}$ and the reflected voltage V_r at some point along the transmission line is given in terms of the reflection coefficient Γ [33]:

$$V_r = \Gamma V_i = \frac{Z - Z_0}{Z + Z_0} V_i = |\Gamma| e^{i\Delta\phi} V_i \tag{A.1}$$

Clearly to derive the amplitude change and phase shift of V_r, we need only calculate Γ. Writing the impedance in terms of its effective resistance R and reactance X:

$$\Gamma = \frac{R + iX - Z_0}{R + iX + Z_0} = \frac{R^2 - Z_0^2 + X^2}{(R + Z_0)^2 + X^2} + i\frac{2XZ_0}{(R + Z_0)^2 + X^2} \tag{A.2}$$

Γ's magnitude is then:

$$|\Gamma| = \frac{\sqrt{(R - Z_0)^2 + X^2}}{\sqrt{(R + Z_0)^2 + X^2}} \tag{A.3}$$

For the case wherein $R > Z_0$ (*i.e.* for tunnel resistance) the identity $Arg(x + iy) = \tan^{-1}(y/x)$ holds, and we find the phase shift:

$$\Delta\phi = \tan^{-1}\left(\frac{2XZ_0}{R^2 - Z_0^2 + X^2}\right) \qquad R \geq Z_0 \tag{A.4}$$

Resonator Sensing

For the case of a series resonator (see fig. 2.4a) probing a small capacitance $C = C_0 + C_p$ in parallel with a possible tunneling or Sisyphus resistance $R \gg Z_0$, its impedance is:

$$Z = i\omega L + \frac{1}{i\omega C + 1/R} \sim \frac{1}{\omega^2 C^2 R} + i\omega L - \frac{i}{\omega C} \qquad R \gg 1/\omega C \tag{A.5}$$

C_0 includes geometric capacitance to the probed system as well as parasitic capacitance to the ground. When probing at radio frequencies and with capacitances on the order of picofarads, a tunneling or Sisyphus resistance will easily satisfy the above limit. In this case, we see that the resonator behaves as a series RLC circuit with effective resistance $R_{eff} = 1/\omega^2 C^2 R \ll Z_0$, provided $1/\omega C \lesssim Z_0$. Consequently, the resonator's characteristic frequency is $\omega_0 = 1/\sqrt{L(C_0 + C_p)}$.

Next, we assume we are near resonance, that is: $|\delta| \equiv |1-\omega/\omega_0| \ll 1$. In the case where we probe at $\omega = 1/\sqrt{LC_0}$ (the resonator's bare frequency), this is equivalent to assuming $C_p \ll C_0$, so that $\delta \sim C_p/2C_0$ to first order. Then:

$$X = \omega L - 1/\omega(C_0+C_p) \sim -\frac{2\delta}{\omega(C_0+C_p)} \qquad \delta \ll 1 \tag{A.6}$$

$$\sim \frac{C_p}{C_0}\sqrt{\frac{L}{C_0}} \sim \frac{C_p}{C_0}\sqrt{\frac{L}{C_0+C_p}} \sim \frac{Q_r C_p(Z_0+R_{eff})}{C_0} \qquad C_p \ll C_0 \tag{A.7}$$

The external quality factor is that for an ideal series RLC circuit [33] $Q_e^s = \sqrt{L/C}/Z_0$ with resistance being that of the transmission line when $R_{eff} \ll Z_0$. Since $C_p \ll C_0$, the phase shift is:

$$\Delta\phi \sim \tan^{-1}\left(\frac{2Q_e^s C_p}{C_0}\right) \tag{A.8}$$

$$\sim 2Q_e^s \frac{C_p}{C_0} \qquad Q_e^s C_p \ll C_0, R_{eff} \ll Z_0 \tag{A.9}$$

when $\omega = 1/\sqrt{LC_0}$, in agreement with Duty *et al* [38].

Next, we consider the analogous problem for a parallel RLC circuit. In this case, the impedance is:

$$Z = \frac{1}{1/R + i\omega C - i/\omega L} = \frac{R}{1+R^2(\omega C - 1/\omega L)^2} + i\frac{1/\omega L - \omega C}{1/R^2 + (\omega C - 1/\omega L)^2} \tag{A.10}$$

Near resonance with the bare frequency $\omega = \omega_0(1+\delta)$ with $\delta \sim C_p/2C_0$ for $C_p \ll C_0$ as before, the the following relation holds:

$$1/\omega L - \omega C \sim \sqrt{C/L}(1-\delta) - \sqrt{C/L}(1+\delta) = -2\sqrt{C/L}\delta \qquad \delta \ll 1 \tag{A.11}$$

such that the impedance near resonance is[1]:

$$Z \sim R - 2iR^2\sqrt{\frac{L}{C}}\delta \qquad \delta \ll R/\sqrt{C/L} \tag{A.12}$$

Leading to an expected phase of the reflection coefficient equal to:

$$\Delta\phi \sim \tan^{-1}\left(\frac{-2R^2 Z_0\sqrt{C/L}\delta}{R^2 - Z_0^2 + 4R^4(C/L)\delta^2}\right) \sim -4Z_0\sqrt{\frac{C}{L}}\frac{\omega-\omega_0}{\omega_0}$$

$$\sim -2Q_e^p \frac{C_p}{C_0} \qquad Z_0 \ll R, C_p \ll C_0 \tag{A.13}$$

when $\omega = 1/\sqrt{LC_0}$, once again proportional to the parametric capacitance C_p. Above, we defined the external quality factor for a parallel RLC circuit as $Q_e^p \equiv Z_0/L\omega_0$ [33].

[1] This condition is not too strong for tunnel resistances on the order of the resistance quantum $R_0 \approx 10^4\Omega$, while for typical values of $C = 0.3pF$ and $L = 400nH$ [56], we expect $\sqrt{L/C} \approx 9\times 10^{-4}\Omega$, so that their ratio is roughly 0.1. As Sisyphus resistance is relatively unexplored in experiment, we abstain from estimating it.

Appendix B

Numerical Simulation of Hybrid Dot Systems

To confirm the broadening effect of degeneracy on quantum capacitance, and in order to study the interference between these degeneracy effects and parity dependent tunnel couplings, a numerical model for simulating arbitrary numbers of dots and total charges N at zero bias was constructed and formatted into a Python package[1]. To make the simulation of interesting systems numerically tractable however, numerous simplifications are needed.

Practical Simplifications, Features, & Limitations

For convenience, mutual capacitances are only incorporated to first order in this model. Furthermore, due to the intractability of simulating a true fermionic continuum of states in the leads, leads are modeled as quantum dots with zero charging energy and some chemical potential, able to contain all the electrons included in the system. Since tunneling to leads is an incoherent process, this is clearly unphysical, but it does simulate broadening due to tunnel couplings between dots and leads well, and correctly calculates the positions of dot-to-lead charge transitions.

Next, we make note of the flexibility of this simulation. Any number of dots and leads may be included with any charging energy and chemical potential, with tunnel couplings and mutual capacitances between any or all of them. Normal dots may be granted a sequence of orbital energy costs associated with each charge state, while superconducting (SC) islands may have any energy of the lowest excitation. In the low energy spectrum, the dots may simulate any number of degenerate fermionic modes for a given charge state, while superconducting quasiparticles may have an arbitrary degeneracy as well. Finally, parity dependent tunneling amplitudes (*eg.* coherence factors for SC quasiparticles) can be added to any SC dot.

The primary limitation of this model is that it is restricted to low energy. To make simulations numerically tractable, the system Hilbert space is drastically reduced to only the states important for the ground and first few excited states, assuming charging and quasiparticle energies are larger than temperature. Following from these assumptions, it is valid to allow only a single quasiparticle state in a superconductor to be occupied at a time. Finally, whichever quantum number is associated with degenerate fermionic modes on a dot (*eg.* spin) is assumed to be the same for each orbital, in that the level of degeneracy remains the same.

In the following section, we motivate and justify the Hilbert space used to construct a system Hamiltonian, proving that operators which add or remove electrons obey fermionic exchange statistics. Since the numerical simulation simply consists of

[1] Source code available at https://github.com/cprosko/pyqd

constructing the Hamiltonian then diagonalizing it using standard methods, it is this step which is most critical to the simulation's functionality.

The Hilbert Space

For non-superconducting quantum dots, a number basis was used, where the number of electrons with each degenerate quantum number ν (*eg.* spin, but it could be a larger degeneracy) are counted separately:

$$|\psi\rangle_D \in \left\{ \prod_{\nu} \otimes |n_\nu\rangle : |n_\nu - n_{\nu'}| \leq 1 \quad \forall \nu, \nu' \right\} \tag{B.1}$$

and the total charge on each dot may range between 0 and some fixed maximum N. This makes use of the critical assumption that the charging energy is the largest energy scale in the system, and that each dot orbital contains the same ν degeneracy, and only this degeneracy. In this case, the total charge on a dot at any given time is fixed within one of some number. In the above Hilbert space definition, we only include states wherein electrons of different quantum number are within one of the same total. Consequently, for a given gate configuration the number of electrons with each quantum number is fixed to some n or $n+1$, where n is the same for all ν. In this way, the Pauli exclusion principle is enforced in the low energy spectrum of this dot, even though electrons of each quantum number are treated as different bosonic modes, reducing the Hilbert space of the dot massively. Whenever a state does not obey the Pauli exclusion principle, it is either energetically forbidden, or in the case where it is eliminated by our choice of Hilbert space, this makes no physical difference, since that state would be energetically degenerate with the ground state of the smaller Hilbert space where the exclusion principle is enforced.

To prove that fermionic anticommutation relations are effectively implemented, we identify the following with effective fermionic creation and annihilation operators $\hat{c}_\nu$:

$$\hat{c}_\nu \equiv |n\rangle \langle n+1|, \quad \hat{c}_\nu^\dagger \equiv |n+1\rangle \langle n| \tag{B.2}$$

From these definitions, we calculate the anticommutation relations, beginning with:

$$\begin{aligned} \{\hat{c}_\nu^\dagger, \hat{c}_\nu\} &= |(n+1)_\nu\rangle \langle n_\nu | n_\nu\rangle \langle (n+1)_\nu| + |n_\nu\rangle \langle (n+1)_\nu | (n+1)_\nu\rangle \langle n_\nu| \\ &= |(n+1)_\nu\rangle \langle (n+1)_\nu| + |n_\nu\rangle \langle n_\nu| = \hat{I}_\nu \end{aligned} \tag{B.3}$$

$\hat{I}_\nu$ is the identity operator for quantum number ν in the local effective Hilbert space. Now, for $\nu \neq \nu'$:

$$\{\hat{c}_\nu^\dagger, \hat{c}_{\nu'}\} = 2\,|(n+1)_\nu\rangle \langle n_\nu| \otimes |n_{\nu'}\rangle \langle (n+1)_{\nu'}| \tag{B.4}$$

If the state of the system is $|n_\nu\rangle \otimes |n_{\nu'}\rangle$, $|(n+1)_\nu\rangle \otimes |(n+1)_{\nu'}\rangle$, or $|(n+1)_\nu\rangle \otimes |n_{\nu'}\rangle$, either $\hat{c}_\nu^\dagger$ or $\hat{c}_{\nu'}$ will bring one of the charge states to $n-1$ or $n+2$, outside of the low energy state-space, effectively annihilating the state. In the only other case, where the state is $|n_\nu\rangle \otimes |(n+1)_{\nu'}\rangle$, the anticommutator is simply a hopping term from one ν to the other. Our Hamiltonian model does not allow for any direct quantum number-flipping matrix elements, so this hopping $\hat{c}_\nu^\dagger \hat{c}_{\nu'}$ never occurs. The only way for this exchange process to occur is second order, via tunneling to a state on another dot. In this case, the resulting fermionic phase of -1 gained by the charge is squared, making it indistinguishable from the bosonic case. Assuming this intermediate mode obeys eq. (B.3) and has creation operator $\hat{d}^\dagger$, we may write out the double hopping process acting on the local vacuum state $|0\rangle = \otimes_\nu |n_\nu\rangle$:

$$\hat{c}_\nu^\dagger \hat{d}^\dagger \hat{d} \hat{c}_{\nu'} \hat{c}_{\nu'}^\dagger |0\rangle = \hat{c}_\nu^\dagger (1 - \hat{d}^\dagger \hat{d})(1 - \hat{c}_{\nu'}^\dagger \hat{c}_{\nu'}) |0\rangle = \hat{c}_\nu^\dagger \tag{B.5}$$

By this reasoning, we assume that the anticommutator need not be fermionic in this specific case, since this combination of operators never appears in the Hamiltonian or any observables. Moving on, the other fermionic anticommutation relation is easy to check for $\nu = \nu'$:

$$\{\hat{c}_\nu, \hat{c}_\nu\} = 2\,|n_\nu\rangle\,\langle (n+1)_\nu | n_\nu\rangle\,\langle (n+1)_\nu| = 0 \tag{B.6}$$

while for $\nu \neq \nu'$:

$$\{\hat{c}_\nu, \hat{c}_{\nu'}\} = 2\,|n_\nu\rangle\,\langle (n+1)_\nu| \otimes |n_{\nu'}\rangle\,\langle (n+1)_{\nu'}| \tag{B.7}$$

The relation is automatically zero for all possible states except $|(n+1)_\nu\rangle \otimes |(n+1)_{\nu'}\rangle$, where by the same reasoning as before, the relation need not apply, since this operator never appears in the Hamiltonian or any observables. A similar argument applies to the conjugate anticommutator. Thus, all fermionic anticommutation relations are either obeyed, or need not be obeyed, in our model. Since the Pauli exclusion principle is fully enforced by energy scales and our choice of Hilbert space, this restricted set of states indeed behaves as fermionic modes when low energies are considered.

Next, superconducting islands are also simulated under the assumption that the charging energy and lowest energy states are large compared to temperature. In this case, we may assume that only one quasiparticle exists at a time in the superconductor, and that this may only occur when the superconductor has odd parity. This is because the island must either pay the charging energy to add another quasiparticle, or twice the lowest energy state to break a Cooper pair. Hence, the Fock space for superconducting islands is defined as:

$$|\psi\rangle_{SC} \in \left\{ |BCS_n\rangle \right\} \cup \left\{ \hat{\gamma}_\nu^\dagger |BCS_n\rangle \right\}_\nu \tag{B.8}$$

Where $|BCS_n\rangle$ denotes the BCS ground state with n Cooper pairs. The range of n is implicitly restricted so that total particle number never exceeds N. As this choice of Hilbert space resulted from direct projection of the full SC island's Hilbert space onto the low energy spectrum, it automatically behaves as truly fermionic. This can also be seen by considering that a single particle (*eg.* a single quasiparticle) behaves identically regardless of its exchange statistics, since there are no other particles for it to exchange with.

The Fock space for leads is simplest of all:

$$|\psi\rangle_L \in \{|n\rangle\}_{n=0}^{n_d N} \tag{B.9}$$

consisting of any charge state between 0 and a charge equal to the number of dots and islands n_d times the maximum decided charge per dot N. As stated previously, this choice is not entirely physical, but it is easy to see that its particle creation operator $\hat{n}_+ = \sum_{n=0}^{n_d N} |n+1\rangle\,\langle n|$ obeys the anticommutator eq. (B.3) necessary for the previous proof of fermionic statistics for normal dots.

The Hamiltonian

The total system Hamiltonian consists of a sum of Hamiltonians for all normal dots $\mathscr{D}$, superconducting dots $\mathscr{S}$ and leads $\mathscr{L}$, as well as a tunneling Hamiltonian $\hat{H}_T$ and mutual capacitance term $\hat{H}_m$:

$$\hat{H} = \sum_{d\in\mathscr{D}} \hat{H}_d + \sum_{s\in\mathscr{S}} \hat{H}_s + \sum_{l\in\mathscr{L}} \hat{H}_l + \hat{H}_T + \hat{H}_m \tag{B.10}$$

Normal dot Hamiltonians contain a charging energy term and an orbital contribution:

$$\hat{H}_d = E_c^d(\hat{n}_d - n_g^d)^2 + \sum_{n=0}^{N}\sum_{\nu} E_n \left|n_\nu\right\rangle \left\langle n_\nu\right| \tag{B.11}$$

where $\hat{n} = \sum_{n=0}^{N} \left|n_\nu\right\rangle \left\langle n_\nu\right|$ is the dot number operator and n_g^d is its reduced gate voltage. For now, the orbital energies do not depend on the degeneracy index ν, but this feature will be added in future updates. Hamiltonians for superconducting islands are simply standard BCS Hamiltonians (in quasiparticle operator representation) with a charging energy term:

$$\hat{H}_s = E_c^s(\hat{n}_s - n_g^s)^2 + \sum_{\nu} E_0 \hat{\gamma}_\nu^\dagger \hat{\gamma}_\nu \tag{B.12}$$

whose corresponding number operator $\hat{n}_s = 2n_C + 1$ or $2n_C$ where n_C is the number of Cooper pairs, while lead Hamiltonians consist solely of a constant chemical potential term:

$$\hat{H}_l = \mu_l \sum_{n=0}^{n_d N} n \left|n_l\right\rangle \left\langle n_l\right| \tag{B.13}$$

generally set to zero with $\mu_l = 0$. This is because non-zero bias is not supported by these simulations, since it would violate the simulation's critical assumption that only low energies are involved.

Mutual capacitances $E_{\alpha\lambda}$ between islands α and λ are only considered to first order in $\hat{H}_m$:

$$\hat{H}_m = \sum_{\substack{\alpha,\lambda\in\mathscr{D}\cup\mathscr{S} \\ \alpha\neq\lambda}} E_{\alpha\lambda} \hat{n}_\alpha \hat{n}_\lambda \tag{B.14}$$

and finally, the tunneling Hamiltonian is completely general except that it does *not* allow spins to be flipped upon tunneling between two dots which both are flagged as having spin σ as their quantum number ν, and in general does not allow electrons to directly tunnel between different ν values within the same dot:

$$\hat{H}_T = \sum_{\substack{\alpha,\lambda\in\mathscr{D}\cup\mathscr{S} \\ \alpha\neq\lambda}} \sum_{\nu_\alpha,\nu_\lambda} t_{\alpha\lambda} f(\nu_\alpha,\nu_\lambda) \hat{c}_{\nu_\alpha}^{\alpha\dagger} \hat{c}_{\nu_\lambda}^{\lambda} \tag{B.15}$$

The function $f(\nu_\alpha,\nu_\lambda)$ 1 in all cases, except when both $\nu_\alpha,\nu_\lambda \in \{\uparrow,\downarrow\}$ and $\nu_\alpha \neq \nu_\lambda$, where it evaluates to 0. Annihilation operators for the normal dots simply act by decreasing n_ν by one but computationally this is more complicated for SC islands. Namely, it decreases an internally stored index of the islands charge state by one, and applies $\hat{\gamma}_\nu^\dagger$ or $\hat{\gamma}_\nu$ depending on whether the island's final parity is even or odd, respectively. This corresponds with creating a hole-like excitation when the superconductor loses an electron going from even to odd parity, or with removing an electron-like excitation when the superconductor loses an electron going from odd to even parity.

As is evident from the above descriptions, systematically generating the system's relevant charge and orbital states and organizing them into a physically correct Hamiltonian for different gate voltages is the complicated part. Once this is complete, the Hamiltonian can be diagonalized and number expectation values or parametric capacitances of low energy states can be evaluated fairly trivially.

Appendix C

Far Off-Resonant Rabi Oscillations

Here we derive the solution of the Rabi Hamiltonian given in Equations (3.8) and (3.10) to first order in the driving potential $\varepsilon(t) = \delta\varepsilon \sin(\omega t)$, and assuming probe frequencies much lower than the characteristic level splitting $\omega \ll 2\sqrt{N} t_c$.

Assuming the system is in its ground state at $t = 0$ so $|\psi(0)\rangle = |-\rangle_0 = (|D\rangle - \sum_{n=1}^{N} |n\rangle)/\sqrt{N+1}$, the general state at time t may be written:

$$|\psi(t)\rangle = c_-(t) e^{i\sqrt{N}|t_c|t/\hbar} |-\rangle_0 + c_+(t) e^{-i\sqrt{N}|t_c|t/\hbar} |+\rangle_0 \tag{C.1}$$

for some time dependent coefficients $c_\pm(t)$. In the basis of $|\pm\rangle_0$ states and after projecting out the decoupled $|n'\rangle$ states, the Hamiltonian reduces to a two-level system:

$$\hat{H} = \sqrt{N}|t_c|[|+\rangle_0 \langle+|_0 - |-\rangle_0 \langle-|_0] + \frac{1}{2}\varepsilon(t)[|-\rangle_0 \langle+|_0 + |+\rangle_0 \langle-|_0] \tag{C.2}$$

Substituting in $|\psi(t)\rangle$ to the Schrödinger equation $i\hbar\partial|\psi\rangle\partial t = \hat{H}|\psi\rangle$ and taking the inner product with either $\langle+|_0$ or $\langle-|_0$ translates this problem to a set of two differential equations for $\dot{c}_\pm \equiv dc_\pm/dt$:

$$\dot{c}_\pm = -\frac{i}{2\hbar}\varepsilon(t) e^{\mp i\omega_0 E t} c_\mp \tag{C.3}$$

defining $\omega_0 = (E_+ - E_-)/\hbar = 2\sqrt{N}|t_c|/\hbar$. Noting that taking a time derivative of $c_\pm$ increases the order of $\delta\varepsilon$ in the result by one, we see that we can calculate the n'th order perturbation expansion of $c_\pm$ in $\delta\varepsilon$ by substituting it into the left side of eq. (C.3) and the $(n-1)$'th order expansion in to the right side. By our own initial conditions, we have $c_-^{(0)} = c_-(0) = 1$ and $c_+^{(0)} = c_+(0) = 0$, so:

$$\dot{c}_- = 0 \quad \Rightarrow \quad c_-^{(1)}(t) = c_-(0) = 1 \tag{C.4}$$

Since the first order correction is equal to zero'th order, we can immediately find the expression for c_+ to second order:

$$\dot{c}_+^{(2)} = -\frac{i\delta\varepsilon}{2\hbar}\sin(\omega t) e^{i\omega_0 t} = -\frac{\delta\varepsilon}{4\hbar}[\exp(i(\omega_0+\omega)t) - \exp(i(\omega_0-\omega)t)] \tag{C.5}$$

This equation may be directly integrated to find:

$$c_+^{(2)}(t) = -\frac{\delta\varepsilon}{4\hbar}\left[\frac{\exp(i(\omega_0+\omega)t) - 1}{\omega_0+\omega} - \frac{\exp(i(\omega_0-\omega)t) - 1}{\omega_0-\omega}\right] \tag{C.6}$$

Hence, to second order in the time-oscillating detuning $\delta\varepsilon\sin(\omega t)$, the probability of an electron occupying the excited state $|+\rangle_0$ at time t when it was initially in the ground state $|-\rangle_0$ is:

$$
\begin{aligned}
P_+(t) &\approx |c_+^{(2)}(t)|^2 \\
&= \left(\frac{\delta\varepsilon}{2\hbar}\right)^2 \left[\frac{\sin^2[(\omega_0+\omega)t]}{(\omega_0+\omega)^2} + \frac{\sin^2[(\omega_0-\omega)t]}{(\omega_0-\omega)^2}\right. \\
&\qquad \left. - \left(\frac{\sin^2[(\omega_0-\omega)t] + \sin^2[(\omega_0+\omega)t] - \sin^2(\omega t)}{\omega_0^2-\omega^2}\right)\right]
\end{aligned}
\tag{C.7}
$$

found after application of the trigonometric identity $1-\cos(2x) = 2\sin^2(x)$ several times. This is obviously a messy result, so for our purposes it is best to make some approximations. We operate in a regime where ω is sub-GHz while $\omega_0 = 2\sqrt{N}t_c/\hbar$ is at least several GHz, so we approximate $\omega \ll \omega_0$. In this case, we can expand all rational terms to first order in ω/ω_0. On the other hand, every term in $P_+(t)$ either is constant, oscillates with frequency $\omega_0 \pm \omega$, or with a frequency proportional to ω. On the time scale of one resonator cycle and considering that $\omega \ll \omega_0 \pm \omega$, it is valid to make a rotating wave approximation, neglecting all terms oscillating with frequency on the order of ω_0. This is because in a time average of $P_+(t)$ over one resonator cycle $2\pi/\omega$, these terms would very nearly average to zero. The probability of occupying the highest excited state then reduces to the simple result:

$$
P_+(t) \sim \left(\frac{\delta\varepsilon}{2\hbar\omega_0}\right)^2 \sin^2(\omega t) \qquad \omega \ll \omega_0, \delta\varepsilon \ll \hbar\omega_0 \tag{C.8}
$$

So the probability of occupying the excited state oscillates roughly with the same frequency as the DGS probe provided $\omega \ll \omega_0$, and has a negligibly small probability of occupying the excited state provided $\delta\varepsilon \ll \sqrt{N}t_c$.

Appendix D

Master Equation Solution for a Degenerate DQD

Here we solve the master equations eq. (3.14) for tunnel rates $\Gamma_+ = \Gamma_0 n_p$ and $\Gamma_- = \Gamma_0(n_p + 1)$ to first order in the oscillating detuning $\varepsilon_0 + \delta\varepsilon(t) = \varepsilon_0 + \delta\varepsilon \sin(\omega t)$, where $n_p(t) = (e^{\Delta E/k_B T} - 1)^{-1}$ is the phonon occupation number at energy ΔE. To this end, we begin by rewriting the master equations, using the fact that $P_- + P_n \approx 1$ and $\Gamma_- - \Gamma_+ = \Gamma_0$:

$$\dot{\chi}(t) = \dot{P}_- - \dot{P}_n = \Gamma_-(1-P_-) - \Gamma_+ P_- - \Gamma_+(1-P_n) + \Gamma_- P_n = \Gamma_0 - (\Gamma_+ + \Gamma_-)\chi(t) \tag{D.1}$$

Above we defined the probability difference $\chi(t) \equiv P_- - P_n$. Motivated by the solution for $\Gamma_0 = 0$, we presume the ansatz $\chi(t) = f(t)\exp - \int_0^t d\tau(\Gamma_- + \Gamma_+)$ for some function $f(t)$. Substituting this into the above equation cancels the rightmost term, leaving:

$$\dot{f}(t) = \Gamma_0 \exp\left[]\int_0^t d\tau(\Gamma_- + \Gamma_+)\right] \quad \Longrightarrow \quad f(t) = \Gamma_0 \int_0^t dt_1 \exp\left[\int_0^{t_1} dt_2(\Gamma_- + \Gamma_+)\right] + f(0) \tag{D.2}$$

This gives the solution for $\chi(t)$:

$$\chi(t) = \Gamma_0 \int_0^t dt_1 \exp\left[-\int_{t_1}^t dt_2(\Gamma_- + \Gamma_+)\right] + f(0)\exp\left[-\int_0^t dt_2(\Gamma_- + \Gamma_+)\right] \tag{D.3}$$

To make this result explicit, we Taylor expand the energy difference ΔE:

$$\begin{aligned}\Delta E &= \sqrt{\frac{1}{4}(\varepsilon_0 + \delta\varepsilon \sin(\omega t))^2 + N|t_c|^2} - \frac{1}{2}(\varepsilon_0 + \delta\varepsilon \sin(\omega t)) \\ &\sim \underbrace{-\varepsilon_0 + \sqrt{\varepsilon_0^2/4 + N|t_c|^2}}_{\equiv \Delta E_0} + \underbrace{\frac{1}{2}\left(\frac{\varepsilon_0}{2\sqrt{\varepsilon_0^2/4 + N|t_c|^2}} - 1\right)}_{\equiv \lambda} \delta\varepsilon \sin(\omega t), \qquad \delta\varepsilon \ll \sqrt{N}|t_c| \end{aligned} \tag{D.4}$$

followed by the tunnel rate Γ_+:

$$\begin{aligned}\Gamma_+ &= \frac{\Gamma_0}{e^{\Delta E/k_B T} - 1} \sim \frac{\Gamma_0}{e^{\Delta E_0}(1 + \lambda\delta\varepsilon(t)/k_B T) - 1} \\ &\sim n_p(0) - \frac{\lambda\delta\varepsilon(t)/k_B T}{2\cosh(\Delta E_0/k_B T) - 2} \qquad \delta\varepsilon \ll k_B T, \sqrt{N}|t_c| \end{aligned} \tag{D.5}$$

From this, we can calculate the following useful integral to first order in $\delta\varepsilon/k_BT$:

$$\int_{t_1}^{t_2} dt(\Gamma_- + \Gamma_+) \sim \Gamma_0 \int_{t_1}^{t_2} dt \left[\left(2n_p(0)+1\right) - \frac{\lambda\delta\varepsilon/k_BT}{\cosh(\Delta E_0/k_BT)-1}\sin(\omega t) \right]$$
$$= \underbrace{\Gamma_0(2n_p(0)+1)}_{\equiv\Gamma_\Sigma}(t_2-t_1) + \underbrace{\frac{(\Gamma_0/\omega)\lambda\delta\varepsilon/k_BT}{\cosh(\Delta E_0/k_BT)-1}}_{\equiv\Lambda}[\cos(\omega t_2)-\cos(\omega t_1)] \tag{D.6}$$

If we substituted this in to the expression for χ, we would see that the $f(0)$ term contains an exponentially decaying transient term. Since we are concerned with the time averaged characteristics of the system, we discard this and all other transient terms. Then Taylor expanding the exponential of the integral and integrating, we find:

$$\begin{aligned}
\chi(t) &\sim \Gamma_0 e^{-\Gamma_\Sigma t}\int_0^t dt_1 e^{\Gamma_\Sigma t_1}\left[1-\Lambda\cos(\omega t)+\Lambda\cos(\omega t_1)\right] \\
&= \Gamma_0(1-\Lambda\cos(\omega t))\frac{e^{\Gamma_\Sigma t}-1}{\Gamma_\Sigma} + \frac{1}{2}\Gamma_0\Lambda e^{-\Gamma_\Sigma t}\int_0^t dt_1\left[e^{(\Gamma_\Sigma+i\omega)t_1}+e^{(\Gamma_\Sigma-i\omega)t}\right] \\
&\sim \frac{\Gamma_0}{\Gamma_\Sigma}(1-\Lambda\cos(\omega t))e^{\Gamma_\Sigma t} + \frac{1}{2}\Gamma_0\Lambda e^{-\Gamma_\Sigma t}\left[\frac{e^{(\Gamma_\Sigma+i\omega)t}-1}{\Gamma_\Sigma+i\omega}+\frac{e^{(\Gamma_\Sigma-i\omega)t}}{\Gamma_\Sigma-i\omega}\right] \\
&\sim \frac{\Gamma_0}{\Gamma_\Sigma}(1-\Lambda\cos(\omega t)) + \frac{\Gamma_0\Lambda}{\Gamma_\Sigma^2+\omega^2}[\Gamma_\Sigma\cos(\omega t)+\omega\sin(\omega t)]
\end{aligned} \tag{D.7}$$

From this result, it is trivial to calculate $P_- = (1+\chi)/2$ and $P_n = 1-P_-$. Finally, note that going to second order would have included terms like $\sin(2\omega t)$ in $\int_{t_1}^{t_2}(\Gamma_- + \Gamma_+)dt$, leading to terms of the form $\sin(2\omega t)$ and $\cos(2\omega t)$ in the final result – both of which average to zero over one period.

Appendix E

Normal-Superconducting Interdot Matrix Elements

In terms of quasiparticle operators, the tunneling Hamiltonian in Equation (3.24) is:

$$\hat{H}_T = t\sum_{\sigma}\left[u^*_{0\sigma}\hat{n}_+\hat{\gamma}_{0\sigma e} - \sigma v_{0\sigma}\hat{n}_+\hat{\gamma}^\dagger_{0-\sigma h} + \sum_{\nu}\left(u^*_{\nu\sigma}\hat{n}_+\hat{\gamma}_{\nu\sigma e} - \sigma v_{\nu\sigma}\hat{n}_+\hat{\gamma}^\dagger_{-\nu-\sigma h}\right)\right] + \text{h.c.} \tag{E.1}$$

For definiteness, suppose the dot is transitioning between $|n\rangle \to |n+1\rangle$ electrons (the reverse process simply has the conjugated matrix element). Then only terms in $\hat{H}_T$ proportional to $\hat{n}_+$ and not $\hat{n}_-$ contribute. Note that Bogoliubov quasiparticles behave as fermionic operators when acting on the superconducting ground state $|g\rangle$, so $\hat{\gamma}\,|g\rangle = 0$ for any $\hat{\gamma}$, and $\{\hat{\gamma}_a, \hat{\gamma}^\dagger_b\} = \delta_{ab}$ for quantum numbers a, b.

For example, let the initial superconductor state be $|g\rangle$ and suppose the E_0 state is absent. The final state must then have a quasiparticle $\hat{\gamma}^\dagger_{\eta\sigma_0 p}$ since the QD and superconductor exchange an electron in this process. Then:

$$\begin{aligned}\langle f|\hat{H}_T|i\rangle &= \langle n+1|\otimes\langle g|\hat{\gamma}_{\eta\sigma p}\hat{H}_T\,|g\rangle\otimes|n\rangle \\ &= t\sum_{\nu}\underbrace{\langle n+1|\hat{n}_+|n\rangle}_{=1}\left(u^*_{\nu\sigma}\,\langle g|\,\hat{\gamma}_{\eta\sigma_0 p}\underbrace{\hat{\gamma}_{\nu\sigma e}\,|g\rangle}_{=0} - \sigma v_{\nu\sigma}\underbrace{\langle g|\,\hat{\gamma}_{\eta\sigma_0 p}\hat{\gamma}^\dagger_{-\nu-\sigma h}\,|g\rangle}_{=\delta_{\eta,-\nu}\delta_{\sigma_0,-\sigma}\delta_{p,h}}\right) + \underbrace{\langle f|(\text{h.c.})|i\rangle}_{=0} \\ &= t\sigma_0\sigma v_{-\eta-\sigma_0}\end{aligned} \tag{E.2}$$

Importantly, charge conservation in the double-dot system implies charge number on the superconductor must be definite (when off resonance), so that an odd parity SCI with a hole-like excitation can only change its state by accepting an electron from the QD and returning to its ground state.

Appendix F

Supplementary Experimental Data

Here we include figures and data which helps provide a complete picture of the sample we measured, and the steps which led us to the various experimental results in the main text, beginning with the RF response of our resonator circuit in Figure F.1. We also show an example illustrating the separate amplitude and phase charge stability diagrams from both the V_{P1} and V_{PS} resonator in fig. F.2.

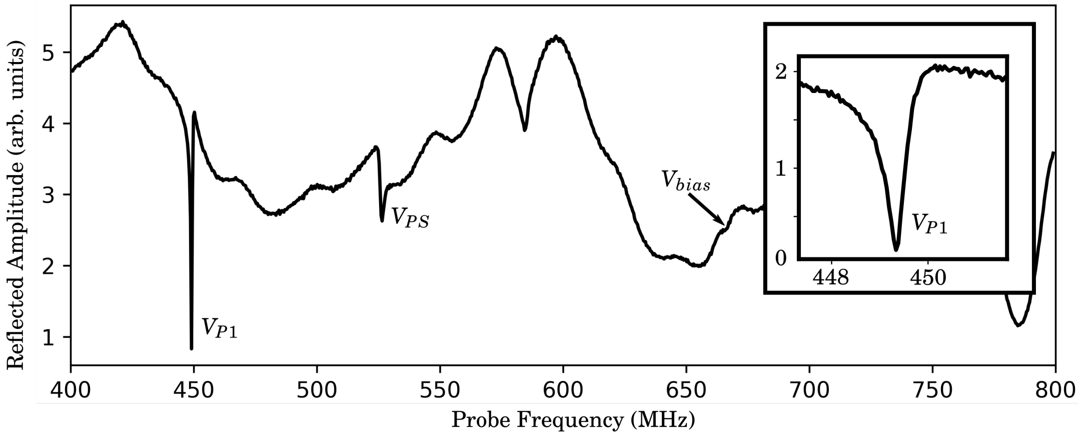

FIGURE F.1: Amplitude response of the chip circuit up to the maximum output frequency of Midas (800MHz) with sample-level power of -128dBm relative to 50Ω. Resonators are identified on the plot by the electrode they are coupled to, V_{bias} being the sample source resonator not used in these experiments. Inset is the V_{P1} resonator recorded in a later measurement where a grounding issue altered the absolute amplitude. Phase response is not plotted because its 2π periodicity causes phase wrapping, which even when 'unwrapped' showed unphysical jumps around 0 and 2π.

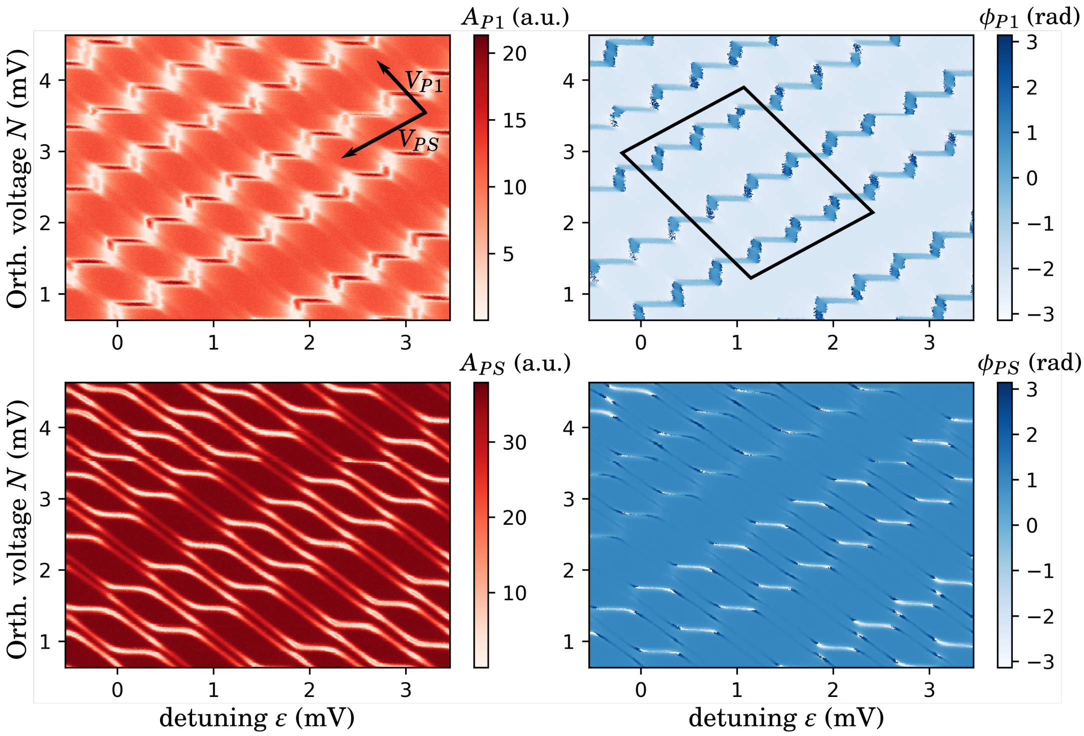

FIGURE F.2: The same stability diagram as in Figure 4.9 in rotated and skewed N,ε voltage coordinates, but where the phase and amplitude response from both the V_{P1} and V_{PS} resonators is shown. The nine interdot transition pairs used for frequency analysis are shown in the black box.

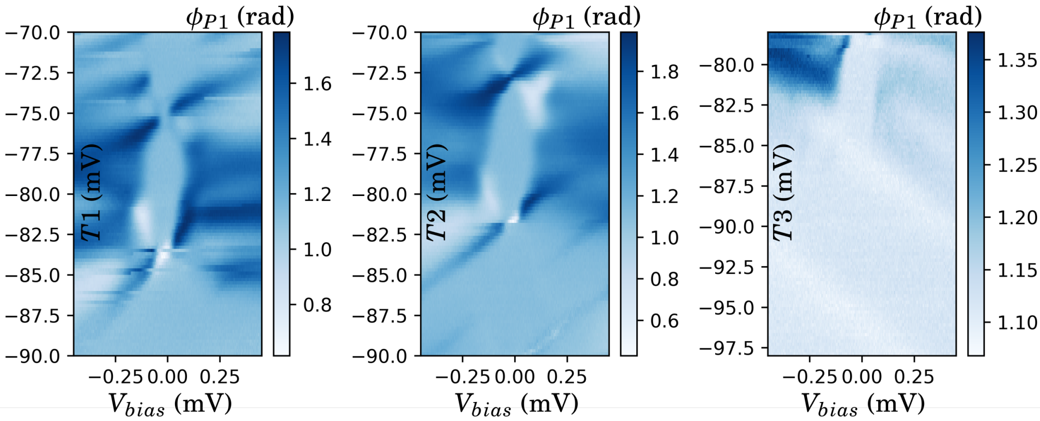

FIGURE F.3: RF tunneling spectroscopy data for the three tunnel gates defining our DQD. Plungers V_{P1} and V_{P2} were opened to $+100\,\text{mV}$ while V_{PS} was left at $0\,\text{mV}$. If the voltage drop primarily occurs over the tunnel barrier being studied, the RF response is related to the density of states at the barrier [66]. Coulomb blockade is observed in certain ranges of barrier strengths for all three voltages, indicating that quantum dots are inherently present in the sample aside from those defined by controllable voltages. Tunneling spectroscopy data is difficult to interpret in our system however, since the metallic leads are not bonded directly adjacent to the barrier.

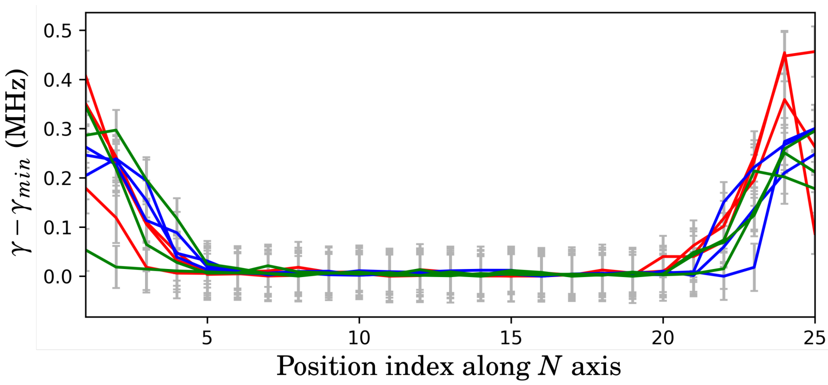

FIGURE F.4: Maximum FWHM γ relative to the minimum γ_{min} at each point along the axis orthogonal to detuning, N, for the nine interdot transition pairs studied in Figure 4.9. At the edges a significant broadening occurs due to the presence of QD to lead transitions, while the interdot transitions show negligible resonator broadening relative to its width within Coulomb blockade. Uncertainty is determined as the root variance of γ, given an uncertainty in the frequency data of ± 0.13MHz estimated from a least squares fit accounting for a linearly varying background. This uncertainty is simply the total fitted variation of the background.

Acknowledgements

Conducting MSc thesis research here at TU Delft has been a wonderful adventure. This place has so many active minds working together to study quantum transport, often with the same goal in mind. As a result, I could thank almost everyone I spoke to during my studies for helping me in some way with my research and understanding of physics, so here I must limit myself ot mentioning just a few.

Firstly, I am grateful to my supervisors Leo and Wolfgang for letting me join their group in the first place. It was a dream come true for me to be able to join the research group I had read so much about during my undergraduate studies in Canada. Thank you Wolfgang for being the ideal supervisor, always interested and involved in what we were working on, willing to debate the underlying physics and provide help whenever. Thank you as well, Leo, for providing some critical advice to re-orient me when my perspective got off track.

Of course, working with such a complicated device and experimental set-up wasn't something I could have just jumped into on my own, particularly coming from a theory background. This research was conducted in close collaboration with Lin Han, where we worked together on trying to understand and measure interesting physics with our sample since first cooling it down. I am forever in the debt of Damaz de Jong and Jasper van Veen as well, for going out of their way to explain things to me and ease me into the world of experimental physics with a wealth of advice and practical help. Finally, a thank you to Daan Waardenburg for many useful debates, forcing me to scrutinize whether or not I ever *really* could justify what I was thinking.

I also wouldn't have made it through the business of writing a MSc thesis without the support of my family and friends. Calls with Amanda and Glenn, my mom and dad, and my sister Ellen kept me sane even though I miss them very much, motivating me to make them proud and reminding me of what is really most important in life. Finally, thank you to my girlfriend Hélène: we both went through MSc studies together, and without sharing this experience with you, I wouldn't have had the confidence to make it through. Thank you and I love you!

Bibliography

1. Colless, J. I., Mahoney, A. C., Hornibrook, J. M., *et al.* "Dispersive Readout of a Few-Electron Double Quantum Dot with Fast rf Gate Sensors". *Phys. Rev. Lett.* **110,** 046805 (4 2013).
2. Zheng, G., Samkharadze, N., Noordam, M. L., *et al.* "Rapid high-fidelity gate-based spin read-out in silicon". *arXiv e-prints.* arXiv: cond-mat.mes-hall/1901.00687 (2019).
3. Mizuta, R., Otxoa, R. M., Betz, A. C., *et al.* "Quantum and tunneling capacitance in charge and spin qubits". *Phys. Rev. B* **95,** 045414 (4 2017).
4. Plugge, S., Rasmussen, A., Egger, R., *et al.* "Majorana box qubits". *New Journal of Physics* **19,** 012001 (2017).
5. Bernstein, D. J. & Lange, T. "Post-quantum cryptography". *Nature* **549,** 188 (2017).
6. Wehner, S., Elkouss, D. & Hanson, R. "Quantum internet: A vision for the road ahead". *Science* **362.** ISSN: 0036-8075 (2018).
7. Grover, L. K. *A Fast Quantum Mechanical Algorithm for Database Search.* in *Proceedings of the Twenty-eighth Annual ACM Symposium on Theory of Computing* (ACM, Philadelphia, Pennsylvania, USA, 1996), 212–219. ISBN: 0-89791-785-5.
8. Lloyd, S. "Universal Quantum Simulators". *Science* **273,** 1073–1078. ISSN: 0036-8075 (1996).
9. Hempel, C., Maier, C., Romero, J., *et al.* "Quantum Chemistry Calculations on a Trapped-Ion Quantum Simulator". *Phys. Rev. X* **8,** 031022 (3 2018).
10. Montanaro, A. "Quantum algorithms: an overview". *Npj Quantum Information* **2,** 15023 (2016).
11. Childs, A. M., Schulman, L. J. & Vazirani, U. V. *Quantum Algorithms for Hidden Nonlinear Structures.* in *48th Annual IEEE Symposium on Foundations of Computer Science (FOCS'07)* (2007), 395–404.
12. Ladd, T. D., Jelezko, F, Laflamme, R, *et al.* "Quantum computers". *Nature* **464,** 45 (2010).
13. Campbell, E. T., Terhal, B. M. & Vuillot, C. "Roads towards fault-tolerant universal quantum computation". *Nature* **549,** 172 (2017).
14. Divincenzo, D. P. "The Physical Implementation of Quantum Computation". *Fortschritte der Physik* **48,** 771–783. arXiv: quant-ph/quant-ph/0002077 (2000).
15. Nayak, C., Simon, S. H., Stern, A., *et al.* "Non-Abelian anyons and topological quantum computation". *Rev. Mod. Phys.* **80,** 1083–1159 (3 2008).
16. Karzig, T. *et al.* "Scalable designs for quasiparticle-poisoning-protected topological quantum computation with Majorana zero modes". *Phys. Rev. B* **95,** 235305 (23 2017).

17. Rančić, M. J., Hoffman, S., Schrade, C., *et al.* "Entangling Spins in Double Quantum Dots and Majorana Bound States". *arXiv e-prints,* arXiv:1902.10251. arXiv: cond-mat.mes-hall/1902.10251 (2019).

18. Aguado, R. "Majorana quasiparticles in condensed matter". *ArXiv e-prints.* arXiv: cond-mat.supr-con/1711.00011 (Oct. 2017).

19. Bonderson, P. & Nayak, C. "Quasi-topological phases of matter and topological protection". *Phys. Rev. B* **87,** 195451 (19 2013).

20. Lutchyn, R. M. & Glazman, L. I. "Kinetics of quasiparticle trapping in a Cooper-pair box". *Phys. Rev. B* **75,** 184520 (18 2007).

21. Oreg, Y., Refael, G. & von Oppen, F. "Helical Liquids and Majorana Bound States in Quantum Wires". *Phys. Rev. Lett.* **105,** 177002 (17 2010).

22. Zhang, H., Liu, C.-X., Gazibegovic, S., *et al.* "Quantized Majorana conductance". *Nature* **556,** 74 (2018).

23. Gonzalez-Zalba, M. F., Barraud, S., Ferguson, A. J., *et al.* "Probing the limits of gate-based charge sensing". *Nature Communications* **6,** 6084 (2015).

24. Kouwenhoven, L. P. *et al.* in *Mesoscopic Electron Transport* 105–214 (Springer Netherlands, Dordrecht, 1997). ISBN: 978-94-015-8839-3.

25. Averin, D. V. & Likharev, K. K. "Coulomb blockade of single-electron tunneling, and coherent oscillations in small tunnel junctions". *Journal of Low Temperature Physics* **62,** 345–373. ISSN: 1573-7357 (1986).

26. Averin, D. V. & Nazarov, Y. V. "Single-electron charging of a superconducting island". *Phys. Rev. Lett.* **69,** 1993–1996 (13 1992).

27. Hanson, R., Kouwenhoven, L. P., Petta, J. R., *et al.* "Spins in few-electron quantum dots". *Rev. Mod. Phys.* **79,** 1217–1265 (4 2007).

28. Van der Wiel, W. G., De Franceschi, S., Elzerman, J. M., *et al.* "Electron transport through double quantum dots". *Rev. Mod. Phys.* **75,** 1–22 (1 2002).

29. Schoelkopf, R. J., Wahlgren, P., Kozhevnikov, A. A., *et al.* "The Radio-Frequency Single-Electron Transistor (RF-SET): A Fast and Ultrasensitive Electrometer". *Science* **280,** 1238–1242. ISSN: 0036-8075 (1998).

30. Reilly, D. J., Marcus, C. M., Hanson, M. P., *et al.* "Fast single-charge sensing with a rf quantum point contact". *Applied Physics Letters* **91,** 162101 (2007).

31. Clerk, A. A., Girvin, S. M. & Stone, A. D. "Quantum-limited measurement and information in mesoscopic detectors". *Phys. Rev. B* **67,** 165324 (16 2003).

32. Field, M., Smith, C. G., Pepper, M., *et al.* "Measurements of Coulomb blockade with a noninvasive voltage probe". *Phys. Rev. Lett.* **70,** 1311–1314 (9 1993).

33. Pozar, D. *Microwave Engineering.* ISBN: 9780471448785 (Wiley, 2004).

34. Croot, Xanthe G. *The Environment and Interactions of Electrons in GaAs Quantum Dots.* PhD thesis (The University of Sydney, 2017).

35. Luryi, S. "Quantum capacitance devices". *Applied Physics Letters* **52,** 501–503 (1988).

36. Büttiker, M., Thomas, H. & Prêtre, A. "Mesoscopic capacitors". *Physics Letters A* **180,** 364 –369. ISSN: 0375-9601 (1993).

37. Sillanpää, M. A. *et al.* "Direct Observation of Josephson Capacitance". *Phys. Rev. Lett.* **95,** 206806 (20 2005).

38. Duty, T. *et al.* "Observation of Quantum Capacitance in the Cooper-Pair Transistor". *Phys. Rev. Lett.* **95,** 206807 (20 2005).

39. Persson, F., Wilson, C. M., Sandberg, M., *et al.* "Fast readout of a single Cooper-pair box using its quantum capacitance". *Phys. Rev. B* **82,** 134533 (13 2010).

40. Crippa, A., Maurand, R., Kotekar-Patil, D., *et al.* "Level Spectrum and Charge Relaxation in a Silicon Double Quantum Dot Probed by Dual-Gate Reflectometry". *Nano Letters* **17,** 1001–1006. ISSN: 1530-6984 (2017).

41. Ciccarelli, C. & Ferguson, A. J. "Impedance of the single-electron transistor at radio-frequencies". **13,** 8. ISSN: 1367-2630 (2011).

42. Pfund, A., Shorubalko, I., Ensslin, K., *et al.* "Suppression of Spin Relaxation in an InAs Nanowire Double Quantum Dot". *Phys. Rev. Lett.* **99,** 036801 (3 2007).

43. De Jong, D., van Veen, J., Binci, L., *et al.* "Rapid Detection of Coherent Tunneling in an InAs Nanowire Quantum Dot through Dispersive Gate Sensing". *Phys. Rev. Applied* **11,** 044061 (4 2019).

44. Zener, C. "Non-adiabatic crossing of energy levels". *Proceedings of the Royal Society of London A: Mathematical, Physical and Engineering Sciences* **137,** 696–702. ISSN: 0950-1207 (1932).

45. Persson, F., Wilson, C. M., Sandberg, M., *et al.* "Excess Dissipation in a Single-Electron Box: The Sisyphus Resistance". *Nano Letters* **10,** 953–957. ISSN: 1530-6984 (2010).

46. Albrecht, S. M., Hansen, E. B., Higginbotham, A. P., *et al.* "Transport Signatures of Quasiparticle Poisoning in a Majorana Island". *Phys. Rev. Lett.* **118,** 137701 (13 2017).

47. Nazarov, Y. & Danon, J. *Advanced Quantum Mechanics: A Practical Guide*. ISBN: 9780521761505 (Cambridge University Press, 2013).

48. Cottet, A., Mora, C. & Kontos, T. "Mesoscopic admittance of a double quantum dot". *Phys. Rev. B* **83,** 121311 (12 2011).

49. Koppens, F. H. L., Folk, J. A., Elzerman, J. M., *et al.* "Control and Detection of Singlet-Triplet Mixing in a Random Nuclear Field". *Science* **309,** 1346–1350. ISSN: 0036-8075 (2005).

50. Deng, M. T., Vaitiekenas, S., Hansen, E. B., *et al.* "Majorana bound state in a coupled quantum-dot hybrid-nanowire system". *Science* **354,** 1557–1562. ISSN: 0036-8075 (2016).

51. Prada, E., Aguado, R. & San-Jose, P. "Measuring Majorana nonlocality and spin structure with a quantum dot". *Phys. Rev. B* **96,** 085418 (8 2017).

52. Nechaev, I. A., Sklyadneva, I. Y., Silkin, V. M., *et al.* "Theoretical study of quasiparticle inelastic lifetimes as applied to aluminum". *Phys. Rev. B* **78,** 085113 (8 2008).

53. Hansen, E. B., Danon, J. & Flensberg, K. "Probing electron-hole components of subgap states in Coulomb blockaded Majorana islands". *Phys. Rev. B* **97,** 041411 (4 2018).

54. Shen, J., Heedt, S., Borsoi, F., *et al.* "Parity transitions in the superconducting ground state of hybrid InSb-Al Coulomb islands". *Nature Communications* **9,** 4801. ISSN: 2041-1723 (2018).

55. van Veen, J., de Jong, D., Han, L., *et al.* "Revealing charge-tunneling processes between a quantum dot and a superconducting island through gate sensing". *arXiv e-prints*. arXiv: cond-mat.mes-hall/1903.09066 (2019).

56. Hornibrook, J. M., Colless, J. I., Mahoney, A. C., *et al.* "Frequency multiplexing for readout of spin qubits". *Applied Physics Letters* **104,** 103108 (2014).

57. Higginbotham, A. P. *et al.* "Parity lifetime of bound states in a proximitized semiconductor nanowire". *Nature Physics* **11,** 1017 (2015).

58. De Moor, M. W. A., Bommer, J. D. S., Xu, D., *et al.* "Electric field tunable superconductor-semiconductor coupling in Majorana nanowires". *New Journal of Physics* **20,** 103049 (2018).

59. Wang, J.-Y., Huang, S., Huang, G.-Y., *et al.* "Coherent Transport in a Linear Triple Quantum Dot Made from a Pure-Phase InAs Nanowire". *Nano Letters* **17,** 4158–4164. ISSN: 1530-6984 (2017).

60. Rainis, D. & Loss, D. "Majorana qubit decoherence by quasiparticle poisoning". *Phys. Rev. B* **85,** 174533 (17 2012).

61. Betz, A. C. *et al.* "Dispersively Detected Pauli Spin-Blockade in a Silicon Nanowire Field-Effect Transistor". *Nano Letters* **15,** 4622–4627 (2015).

62. Urdampilleta, M., Chatterjee, A., Lo, C. C., *et al.* "Charge Dynamics and Spin Blockade in a Hybrid Double Quantum Dot in Silicon". *Phys. Rev. X* **5,** 031024 (3 2015).

63. Albrecht, S. M., Higginbotham, A. P., Madsen, M., *et al.* "Exponential protection of zero modes in Majorana islands". *Nature* **531,** 206 (2016).

64. Deng, M.-T., Prada, E., *et al.* "Nonlocality of Majorana modes in hybrid nanowires". *Phys. Rev. B* **98,** 085125 (8 2018).

65. Fu, L. "Electron Teleportation via Majorana Bound States in a Mesoscopic Superconductor". *Phys. Rev. Lett.* **104,** 056402 (5 2010).

66. Klein, J., Léger, A., Belin, M., *et al.* "Inelastic-Electron-Tunneling Spectroscopy of Metal-Insulator-Metal Junctions". *Phys. Rev. B* **7,** 2336–2348 (6 1973).